# UNIVERSITY OF SOUTHAMPTON

FACULTY OF ENGINEERING AND ENVIRONMENT
School of Engineering Sciences

**Design, construction and characterisation of an iron air battery for automotive propulsion**

by

**Horacio Antonio Figueredo Rodríguez**

A Thesis presented for the degree of
Doctor of Philosophy

November 2018

**UNIVERSITY OF SOUTHAMPTON**

# Abstract

FACULTY OF ENGINEERING AND ENVIRONMENT

Electrochemical Engineering Group

## DESIGN, CONSTRUCTION AND CHARACTERISATION OF AN IRON AIR BATTERY FOR AUTOMOTIVE PROPULSION

Horacio Antonio Figueredo-Rodríguez

Novel energy storage technologies are required to further the development of crucial applications to reduce the dependence on fossil fuels. In particular for electric propulsion and for the efficient utilization of intermittent sources of renewable energy. Metal-air-batteries are appealing candidates to develop these type of energy-storage-technologies due to their theoretical energy-density. In particular the iron-air-battery (**IAB**) with a theoretical energy-density of 764 W h $kg^{-1}$, represents a low cost, environmentally friendly alternative.

During the 70s, research into the IAB system was performed and a few laboratory prototypes were developed. Unfortunately, the specific energy density and cell potential of these prototypes were far below their theoretical value due to challenges in their engineering design and electrochemistry performance. Recently, the study of IABs has been of special interest to the automotive industry, due to the possibility of rechargeable metal-air batteries for electric vehicles. Furthermore, the new technological advances in nanomaterials since the 70s, and the use of new catalyst materials in combination with innovative laboratory tools for the manufacturing of the electrodes have enabled IAB s to achieve a further level of development.

The main research goal of this Ph.D. research has been to determine the electrochemical performance of a novel IAB using novel nanostructured materials reported in the literature and to gain insight of what are the advantages and main challenges of this electrochemical system.

The applied methodology included to develop and optimise each one of its components, mainly the negative iron-electrode, and the positive bifunctional-gas diffusion-electrode. The detailed study of the iron-electrode lead to the comparison of various reported active-iron-materials including: carbonyl iron, hematite, goethite, magnetite and iron sulphide as active-materials in hot-pressed-iron-electrodes, this research lead to the development of iron-electrodes with capacities as high as 910 m A $g^{-1}_{Fe}$ using $Fe_2O_3$/C, and mean discharge capacities of 650 m A $g^{-1}_{Fe}$ over 240 hrs of continuous reduction-oxidation cycling at the C/5 rate (254.6 mA $g^{-1}_{Fe}$).

Research on the air electrode lead to the development of a gas diffusion electrode with a remarkably stability able to cycle up to 3000 cycles continuously and to perform at current densities up to 1000 mA $cm^{-2}$ before deteriorating. Furthermore the comparison of Ni-Fe hex-cyanoferrate, palladium and LSFCO perovskite on carbon as bifunctional catalysts and its combination lead to the development of optimised gas diffusion electrodes.

In parallel the development as a proof of concept of an IAB stack and a larger scale IAB (200$cm^2$ GDE electrodes) required the engineering design of various IAB prototypes which were manufactured using 3D printing techniques that allowed rapid modifications and improvements before an optimised prototype was sent to be manufactured using traditional computer numerical control machining. The electrochemical testing of these batteries prototypes are as well part of the main results of this research.

Finally the electrochemical performance of a novel iron air battery prototype with an energy density as high as 453 W h $kg^{-1}_{Fe}$ and a maximum capacity of 814 mA h $g^{-1}_{Fe}$ when cycled at a current density of 10 mA $cm^{-2}$ equivalent to 100 mA $g^{-1}_{Fe}$, achieving a power density of *ca.* 75 W $kg^{-1}_{Fe}$ was achieved.

# Table of contents

**Abstract…..** ..... **iii**

**Table of contents** ..... **v**

**List of tables** ..... **viii**

**List of figures** ..... **ix**

**Declaration of authorship** ..... **xv**

**Acknowledgements** ..... **xvii**

**Abbreviations** ..... **xix**

**Symbols**……**xx**

**Chapter 1: Objectives, publications, and research paths** ..... **21**

1.1 Foreword ..... 21

1.2 Objectives ..... 23

1.3 Publications resulting from this research ..... 24

**Chapter 2: The iron air battery electro-chemical system** ..... **27**

2.1 Energy density of electrochemical couples ..... 29

2.1.1 Types of batteries ..... 32

2.1.2 Major secondary electrochemical systems ..... 33

2.2 Metal air batteries ..... 37

2.3 Electric vehicles ..... 42

2.4 History of the iron air batteries. ..... 46

2.5 Iron-air battery conceptual design ..... 49

2.6 Iron-air battery main challenges ..... 52

**Chapter 3: The negative iron electrode** ..... **55**

3.1 Iron electrodes in other related batteries ..... 55

3.2 Iron electrode behaviour in alkaline media ..... 56

3.3 The iron electrode performance challenges ..... 58

3.3.1 Hydrogen evolution reaction ..... 58

3.3.2 Hydrogen evolution over the iron electrode and the role of sulphides in the electrolyte ..... 60

3.3.3 Passivation of the iron electrode ..... 63

3.3.4 Iron electrode self-discharge and corrosion ..... 64

3.4 Iron electrode porosity considerations ..... 65

3.5 Different types of iron active materials ..... 67

3.6 Strategies to improve the iron electrode performance ..... 68

3.7 Iron electrode conceptual design ..... 69

**Chapter 4: The positive air electrode ..... 71**

4.1 The oxygen reduction reaction (ORR) electro-catalysts ..... 71

4.2 The oxygen evolution reaction (OER) electro-catalysts ..... 74

4.3 The bifunctional catalyst ..... 75

4.4 Factors affecting gas diffusion electrode performance ..... 79

4.5 Bifunctional gas diffusion electrode conceptual design ..... 80

**Chapter 5: Iron electrode experiments and results ..... 83**

5.1 Experiments performed on the iron electrode ..... 83

5.2 Preparation of hot pressed iron electrodes (HPIE) ..... 84

5.3 Iron electrode half-cell prototype ..... 86

5.4 Effect of Fe/C ratio on the capacity of $Fe_2O_3$/C HPIE ..... 86

5.5 Effect of synthesis method of $Fe_2O_3$/C on the discharge performance of HPIE ..... 89

5.6 Effect of ball milling on different iron active material formulations ..... 91

5.7 Discharge capacity of various iron active materials electrodes E2-E5 ... 97

5.8 Discharge capacity of various ball milled iron formulations electrodes E7-E10 ..... 99

5.9 Discharge capacity comparison of all hot-pressed iron electrode formulations, electrodes E1-E10 ..... 100

5.10 Morphology change on ball milled iron active materials ..... 101

5.11 Discharge capacity comparison with other reported iron electrodes .... 103

5.12 Conclusions and further work on the iron electrode ..... 107

**Chapter 6: Bifunctional air electrode experiments and results ..... 110**

6.1 Bifunctional electro-catalyst preparation ..... 110

6.1 Bifunctional catalyst preparation ..... 112

6.2 Electro-chemical characterisation of GDE ..... 113

6.3 Bifunctional air electrode catalyst loading optimization ..... 118

6.4 Computer assisted tomography to study the mesoporous structure of the GDE ..... 123
6.5 Conclusions and further work on the air electrode ..... 125
**Chapter 7: Engineering design of an IAB ..... 127**
7.1 The importance of cell design ..... 127
7.2 Engineering design of the IAB battery cell ..... 128
7.3 IAB preliminary designs ..... 129
7.4 3D printing the laboratory prototypes ..... 132
7.5 Final design for the IAB laboratory cell ..... 133
7.6 Design of an iron air battery stack ..... 135
7.7 Scaling up the cell (200 $cm^2$ electrodes) ..... 137
**Chapter 8: Iron air battery performance and characterisation results. ..... 139**
8.1 Prototype 1. IAB flow cell ..... 139
8.2 Prototype 2. IAB static-bipolar-1cm inter-electrode gap cell ..... 140
8.3 Prototype 3. Improved IAB screw less static design ..... 141
8.4 Prototype 4. IAB static-design open cell ..... 142
8.5 Charge-discharge of prototype-5 supplying $O_2$ ..... 144
8.6 Continuous charge-discharge cycling and air supply prototype 5 ..... 146
8.7 Charge discharge profiles only 1 air electrode prototype 5 ..... 148
8.8 Effect of current density on the discharge capacity ..... 149
8.9 Charge-discharge profiles considering only the 1st plateau ..... 153
8.10 Life cycle and deterioration of the IAB components ..... 154
8.11 Performance of the IAB stack ..... 155
8.12 Electrochemical testing of 200 $cm^2$ electrodes ..... 160
8.13 Conclusions on the performance of the IAB ..... 161
**Chapter 9: Conclusions, future work and final remarks ..... 165**
**Appendix A NECOBAUT flow cell design ..... 171**
**Appendix B Activities chronogram ..... 174**
**References ..... 181**

# List of tables

Table 1. Major secondary batteries electrochemical systems overall cell reactions (⟶ discharge, ⟵ charge) ....36
Table 2. Metal air/$O_2$ batteries anode and overall cell reactions....39
Table 3. Metal air/oxygen cells characteristics. ....40
Table 4. Major iron air battery developments operational parameters [2,31,42]....48
Table 5. State of the art IAB performance and suggested targets [31] ....53
Table 6. Volume change during discharge. ($V_o$ volume of 1 mol of Fe)....66
Table 7. Synthesis details for iron electrodes formulations. ....85
Table 8. Formulations ICR1-ICR3 to test different iron to carbon ratios. ....87
Table 9. Formulations ICR1-ICR3 to test the electrochemical performance of hematite synthetized by the oxalate and the Adams methods. ....90
Table 10. Formulations E1-E10, with the mass of each component (their percentage by weight, in the mixture, in brackets). ....92
Table 11. Comparison between similar iron electrodes reported in the literature ....104
Table 12. Cell performance data for the first seven cycles of cell 3. ....145
Table 13. Energy and power density for the IAB in prototype 5 at various current densities…. ....151
Table 14. Performance of the IAB 5 cells stack at different current densities....157
Table 15. NECOBAUT complete list of components specification. ....171
Table 16. Used cell components specification. ....173

# List of figures

Figure 1. Theoretical standard energy densities for electrochemical systems according to the Nernst Equation [15]. .....31

Figure 2. MAB schematic during discharge. The active materials in a MAB are a metallic anode and the oxygen taken directly from atmospheric air. .....37

Figure 3. Metal air batteries characteristics. Theoretical gravimetric energy density considering only mass of the metal anode (in purple) and considering the mass of the hydroxides (magenta). .....41

Figure 4. Status of advanced Li-ion battery development relative to the USA BC goals for EVs [34] .....44

Figure 5. Relative frequency of use over daily driving-range, and battery electric vehicle (BEV) range projection for different batteries. (Data for 2003) [32]. .....45

Figure 6. Three-electrode configuration of an IAB. This configuration includes an iron electrode, a gas diffusion electrode for the ORR during discharge and an auxiliary charging electrode (*i.e.* a nickel counter electrode). .....50

Figure 7. Two-electrode configuration of an IAB. This configuration use one iron electrode in combination with a bifunctional gas diffusion electrode that must contain a catalyst able to promote both the oxygen reduction reaction during discharge and the oxygen evolution during charge. .....51

Figure 8. Typical iron electrode charge-discharge profile at the C/5 rate (254 mA $g^{-1}_{Fe}$), own data. .....57

Figure 9. Pourbaix diagrams for iron-water systems at 298K, based on data from [58]. ..65

Figure 10. Iron electrode conceptual design. a) High surface area support material (*e.g.* Ketjenblack), b) Binder (*e.g.* PTFE), c) Iron active material (*e.g.* $Fe_2O_3$, $Fe_3O_4$, FeOOH, Carbonyl iron, FeS), d) Additives to diminish HER (*e.g.* $Bi_2O_3$, $Bi_2S_3$, FeS) e) Pore former (*e.g.* $K_2CO_3$) f) Current collector (*e.g.* stainless steel mesh and metal foams). .....70

Figure 11. Example models for the ORR. On the left model suggested by Damjanovic *et al.* [70], on the right model proposed by Bagotskii *et al.* [26]. Subscript "a" means adsorbed on electrode surface, "b" means in bulk solution, "*" means in the vicinity of electrode surface. .....73

Figure 12. Schematics to compare the performance of various bifunctional catalyst in GDE…. .....76

Figure 13. Typical cyclic voltammograms of a gas diffusion electrodes with different loadings of the Pd/C bifunctional catalysts. The left arm corresponds to the ORR while the extreme right to the OER. Adapted from [6]. .....77

Figure 14. Cyclic voltammetry comparison between seven reported bifunctional catalyst and the in-house Pd (0.5 mg $cm^{-2}$) + Ni-Fe HCF (5 mg $cm^{-2}$) GDE, adapted from [5]…… .....78
Figure 15. Air-electrode conceptual design. a) oxygen permeable membrane, b) gas diffusion layer, c) current collector, d) catalyst support material, e) bifunctional catalyst, f) hydrophobic binder material.....81
Figure 16. Experimental cell arrangement. a) Hot-pressed iron working electrode, b) Nickel plate counter electrode, c) Luggin capillary connected to Hg/HgO reference electrode, d) ABS 3D printed electrodes support. Interelectrode gap: 2 mm, e) Electrolyte: 6M KOH solution. .....86
Figure 17. Charge-discharge profiles at the C/5 rate for electrode ICR1. .....87
Figure 18. Discharge capacity of electrodes ICR1, ICR2 and ICR3. These formulations only differ in the proportion of iron to carbon being 0.7, 2.0 and 5.7 respectively….....88
Figure 19. Discharge capacity of hot pressed $Fe_2O_3$/C electrodes at the C/5 rate (mA $g^{-1}$ Fe). Left: Fe/C = 0.7 Center: Fe/C 2.0 Rigth: Fe/C = 5.7 .....89
Figure 20. Discharge capacity of $Fe_2O_3$/C electrodes at the C/5 rate (255 mA $g^{-1}_{Fe}$) synthetized by: a) SM1-Adams method b) SM2-Oxalate method .....90
Figure 21. Descriptive statistics of the discharge capacity at the C/5 rate of electrodes E1, and E4: Left: Adams at 500°C Rigth: Oxalate method (*n.b.* Fe/C = 0.7).....91
Figure 22. Galvanostatic charge-discharge for the E1 - iron sulphide formulation at C/5 rate ($m_{Fe}$ = 85 mg and $I_{C/5}$ = 22 mA, $V_{co}$ = -0.55 V vs. Hg/HgO). The 1st and 2nd plateaux of some cycles are indicated with arrows. .....93
Figure 23. E1- iron sulphide electrode 49 charge-discharge overlaid cycles at C/5 rate ($i_{C/5}$ = 22 mA). .....94
Figure 24. E1- iron sulphide electrode discharge capacity of each cycle. .....95
Figure 25. E6 - ball milled iron-sulphide electrode detailed discharged capacity of each cycle…. .....95
Figure 26. E1 and E6 – Iron sulphide electrodes discharge capacity performance .....96
Figure 27. E2-E5 Iron electrodes detailed discharged capacity during each cycle.....97
Figure 28. E7-E10 Iron electrodes manufactured with ball milled materials. Detailed discharged capacity of each cycle. .....99
Figure 29. Iron electrodes discharge capacity at the C/5 rate performance summary. ....100
Figure 30. SEM images of different iron active materials before ball milling corresponding to E1-E5 formulations .....102
Figure 31. SEM images of different iron active materials after ball milling corresponding to E6-E10 formulations .....102

Figure 32. Iron electrode comparison. Note that the references taken from the literature electrodes LR1-LR6, [54,55,60,61,86,87] respectively, have been highlighted to distinguish them from the in-house hot pressed electrodes E1-E10. .....105
Figure 33. Bi-functional air electrodes schematics. Carbon cloth as support material 80% carbon and 20% PTFE as hydrophobic layer, a Pd catalyst loading of 0.5 mg $cm^{-2}$ and Ni mesh as current collector hot pressed at 140 °C and 250 kPa. .....111
Figure 34. Left: Bi-functional in-house manufactured (5cm x 5cm x 0.5 mm) air electrode. Right: SEM image of its cross-section [4]. .....112
Figure 35. Experimental set up to test the GDE. Pt mesh counter electrode in 6 M KOH electrolyte, oxygen/air supplied to the back part of the air electrode at 100 ml $min^{-1}$ and Hg/HgO as reference electrode. .....113
Figure 36. Cyclic voltammograms for 3 different electro-catalysts formulations for GDE. Scan rate 1 mV $s^{-1}$ in 6 M KOH, with 100 mL $min^{-1}$ $O_2$ flow into the back of the electrodes. .....114
Figure 37. Reduction (30 mins) – oxidation (30 mins) profiles of GDE using 3 different electro-catalysts in GDE at 20 mA $cm^{-2}$ in 6 M KOH, with 100 ml $min^{-1}$ $O_2$ flow into the back of the electrodes. .....115
Figure 39. Reduction-oxidation profiles of the Ni/Fe + Pd/C catalysed gas diffusion air electrodes at [40 - 2000 mA $cm^{-2}$ current density in 6 M KOH, with 100 ml $min^{-1}$ $O_2$ flow into the back of the electrodes. .....116
Figure 40. Simplified Pourbaix diagram for C, adapted from [93,94] .....117
Figure 41. Charge-discharge potential E at various current densities for the GDE with Ni/Fe + Pd…… .....118
Figure 42. Cycle voltammograms for both the OER and ORR of Pd/C at various loadings ranging from 0.5 mg $cm^{-2}$ -10 mg $cm^{-2}$. Pt mesh counter electrode in 6 M KOH Oxygen (99.999%, BOC) supplied at 100 $cm^3$ $min^{-1}$ at a scan rate of 10 mV $s^{-1}$…….....119
Figure 43. Cycle voltammograms for both the OER and ORR of Ni-Fe HCF/C at various loadings ranging from 0.5 mg $cm^{-2}$ -10 mg $cm^{-2}$. Pt mesh counter electrode in 6 M KOH Oxygen (99.999%, BOC) supplied at 100 $cm^3$ $min^{-1}$ at a scan rate of 10 mV $s^{-1}$…. .....119
Figure 44. Polarization curves of various gas diffusion electrodes that only differs in the respective loading of both Ni/Fe hexacyanoferrate and Pd/C electrocatalysts loadings Scan rate at 10 mV $s^{-1}$. .....120
Figure 45. Cycle voltammograms for both the OER and ORR of LSFCO/C at various loadings ranging from 0.5 mg $cm^{-2}$ -10 mg $cm^{-2}$. Pt mesh counter electrode in 6

M KOH Oxygen (99.999%, BOC) supplied at 100 $cm^3$ $min^{-1}$ at a scan rate of 10 mV $s^{-1}$. .....121
Figure 46. Cycle voltammograms for both the OER and ORR of 3 electro-catalysts combinations. Pt mesh counter electrode in 6 M KOH Oxygen (99.999%, BOC) supplied at 100 $cm^3$ $min^{-1}$ at a scan rate of 10 mV $s^{-1}$. .....121
Figure 47. Reduction (30 mins) – oxidation (30 mins) GDE profiles comparison using 5 electro-catalysts at 20 mA $cm^{-2}$ in 6 M KOH, with 100 ml $min^{-1}$ $O_2$ flow into the back of the electrodes. .....122
Figure 48. Reduction-oxidation potential as a function of the current density for various GDE formulations. .....123
Figure 49. 3D reconstruction from tomography data of a gas diffusion electrode. .....124
Figure 50. Electron microscope SEM and TEM of a) Pd/C, b) Ni-Fe HCF and c) LSFCO/C electro-catalysts, SEM performed on a 0.5-30 kV JSM 6500F thermal emission SEM and TEM performed using a 300 kV JEOL 3010 TEM on S147-3 copper grids coated with perforated carbon film (Agar Scientific).....124
Figure 51. Conceptual design No 1. 3D CAD model. .....130
Figure 52. Conceptual designs No. 2 and No. 3. .....130
Figure 53. Conceptual design No.4. For this design consideration to allow the air to flow in a serpentine structure were maintained. The thickness of the end plates was increased to avoid the bending of these parts when it is under compression. ..131
Figure 54. This cell is a flow cell to ensure that the electrolyte level is always enough to avoid leaving the electrodes dry during operation. This model has not yet been 3D printed or tested. .....132
Figure 55. 3D printer “Dimensions 1200es”.....133
Figure 56. Prototype 5. Left. 3D CAD model assembly, Right. 3D printed cell assembled with all its components, weight 350 g, overall height = 9 cm, overall width 11.0 cm overall thickness = 3.9 cm. Electrode area 25 $cm^2$. .....133
Figure 57. Prototype-5 exploded view. List of parts: 2 end plates, 4 silicon gaskets, 2 air electrodes, 1 iron electrodes, 1 main body, 1 inner lid, 1 top lid, 5 nylon screws…. .....134
Figure 58. Prototype 5 disassembled. List of parts: 2 end plates, 4 silicon gaskets, 2 air electrodes, 1 iron electrodes, 1 electrolyte compartment body, 1 inner lid, 1 top lid, 5 nylon screws. .....134
Figure 59. Iron air battery 5 cell stack CAD design done in Autodesk Inventor 2015. Units are in mm. .....135
Figure 60. 3D printed IAB 5 cell stack. .....136

Figure 61. IAB 5-cells-stack 3D printed at UoS (right) and the outer protective case manufactured by Tecnicas Reunidas (left). .....136
Figure 62. Large IAB cell design. Cell dimensions: overall height = 215 mm, Overall width = 147 mm, Overall thickness = 47 mm, Electrode area = 200 $cm^2$. .....137
Figure 63. Large house-made IAB cell components.....137
Figure 64. Left: first IAB flow cell prototype. Right: Discharge curve of IAB prototype iron electrode and improved air electrode (30% Pd-Vulcan with Ni mesh) at 1 mA $cm^{-2}$, with oxygen and electrolyte flow rates at 50 $cm^3$ $min^{-1}$. The individual electrode potentials were measured against an Hg/HgO (1M KOH) reference electrode. The average cell voltage for the first discharge plateau was 0.82 V, and the total energy density was 451 W h $kg^{-1}_{Fe}$ at only 1 mA $cm^{-2}$, flow rate 5 $dm^3$ $min^{-1}$.....139
Figure 65. Left: Photograph of prototype-2 inter-electrode gap 1 cm. Right: Discharge profile for the best cycle at 10 mA $cm^{-2}$. The electrolyte was 6 M KOH and oxygen was flowed into the cell at a rate of 100 $cm^3$ $min^{-1}$.....141
Figure 66. Left. 3D-model of prototype-3, Middle. 3D-printed prototype-3, Right. Top view of the cell interior. Inter-electrode gap 64 mm. .....142
Figure 67. Discharge profile for the best cycle at 5 mA $cm^{-2}$ in prototype 3. The electrolyte was 6 M KOH and oxygen was flowed into the cell at a rate of 100 $cm^3$ $min^{-1}$…….....142
Figure 68. Static open cell design. In this cell the inter electrode gap was 6 mm. .....143
Figure 69. Discharge profile obtained with prototype 4 at 10 mA $cm^{-2}$. The iron electrode was the improved iron electrode sent by TECNALIA, and the air electrodes were the improved air electrodes catalysed with the 30% Pd/C developed by CNR-ITAE….....144
Figure 70. Cycling of prototype 5 filled with 6 M KOH, and 100 ml $min^{-1}$ oxygen flow into the back of the air electrodes. The air electrodes were catalysed with 30 wt % Pd/C developed by CNR-ITAE. Potential is *vs* the Hg/HgO ref electrode. .....145
Figure 71. Charge-discharge cycling of prototype 5 with air suply into the back of the air electrodes at 1 $dm^3$ $min^{-1}$ and a gradual increase in cycling current density (both charge and discharge) in the range from 5-25 mA $cm^{-2}$. .....146
Figure 72. Charge-discharge curves of prototype 5 with only one air electrode at different current densities, the iron and air individual half-cell potentials are refered to the Hg/HgO reference electrode. The dotted line refers to the cut-off potential of 0.45 V…… .....148
Figure 73. Discharge curves of prototype 5 with only one air electrode at different current densities in prototype 5.....150

Figure 74. Effect of current density on the energy density and capacity of the whole discharge cycle using prototype 5. .....150
Figure 75. Effect of current density on the energy density and capacity of the whole discharge cycle using prototype 5. .....152
Figure 76. Charge-discharge profile. Cut off voltage set up at 0.5 V. Only the 1st plateau is discharged inside prototype 5 using only 1 air electrode, KOH 6M electrolyte, Hg/HgO reference electrode.....153
Figure 77. Capacity and energy density for each cycle presented in Figure 74.....154
Figure 78. Scanning electron micrographs of the surface of carbon cloth after 4 h treatment with (left) distilled wather, and (rigth) 6M KOH, the one on the right lost had lost its hydrofobicity. .....155
Figure 79. Charge-discharge cycling of the 5 IAB cells-stack. .....156
Figure 80. Discharge profiles of the 5 IAB cells-stack a t various current densities.....156
Figure 81. Charge discharge curves for the stack and the five cells that comprise the stack. The current density was 10 mA $cm^{-2}$, and the air flow rate was 1 L $min^{-1}$.....158
Figure 82. Polarisation curve of the stack, measured at a scan rate of 0.25 mA $s^{-1}$.....159
Figure 83. Discharge capacity profiles for the 200 $cm^2$ IAB cell at 1.25 mA $cm^{-2}$, 2.5 mA $cm^{-2}$ and 5 mA $cm^{-2}$ discharge rates. .....160
Figure 84. Typical charge-discharge IAB profile at 10 mA $cm^{-2}$. .....165
Figure 85. NECOBAUT Iron-air battery laboratory prototype. .....171
Figure 86. Actual NECOBAUT configuration for cell-characterisation-laboratory testing…. .....172

# Declaration of authorship

I, Horacio Antonio Figueredo-Rodríguez, declare that this thesis and the work presented in it are my own and has been generated by me as the result of my own original research:

Design, construction and characterisation of an iron-air battery for automotive propulsion

I confirm that:

1. This work was done wholly or mainly while in candidature for a research degree at this University;
2. Where any part of this thesis has previously been submitted for a degree or any other qualification at this University or any other institution, this has been clearly stated;
3. Where I have consulted the published work of others, this is always clearly attributed;
4. Where I have quoted from the work of others, the source is always given. With the exception of such quotations, this thesis is entirely my own work;
5. I have acknowledged all main sources of help;
6. Where the thesis is based on work done by myself jointly with others, I have made clear exactly what was done by others and what I have contributed myself;

Signed:.....

Date: .....

# Acknowledgements

I would like to express my depth gratitude to my main supervisor, Dr. Carlos Ponce de León Albarrán and Dr. Rachel D. Mckerracher, for their invaluable guidance and their willingness to share their time and knowledge with me throughout my postgraduate study. I also want to offer my special thanks to Dr. Richard Wills and Professor Frank Walsh for their objective and constructive recommendations.

I would like to express as well my gratitude to all the partners involved in the EU FP7 NECOBAUT project, this have been an insightful and valuable experience that allow me to be part of this laudable research collaboration. I want to express my gratitude in particular to Dr. Cinthia Alegre who has shared much of her time and knowledge during this research collaboration.

I would like to acknowledge as well the postgraduate students I had the opportunity to work with at the electrochemistry laboratory, MSc. Karol Kwasnicki, MSc. Olaf Ávila-Alejo, and MSc. Konstantinos whose enthusiasm and diligent research allowed the further development of bifunctional gas diffusion electrodes and optimization of hot pressed iron electrodes.

I would like to show gratitude to my examiners who took their time to read thoroughly my thesis and who provided valuable and critical observations.

My very great appreciation to CONACYT-FiiDEM institutions for their financial support that allowed me to pursue my Ph.D. in Engineering and Environment at the University of Southampton.

I would also like to extend my thanks to the mechanical and glass workshops and electronic circuits specialized technicians for their support with the required aid and services during my research.

Finally but not least, I would like to praise my family for their support and encouragement during my postgraduate studies and to all the amazing people that I had the opportunity to meet along in Southampton during the last few years, so many memorable experiences to treasure together with the cultivated friendships that shall continue for the times to come.

# Abbreviations

| | |
|---|---|
| ABS | acrylonitrile butadiene styrene |
| BEV | battery electric vehicles |
| CCD | current density distribution |
| DoD | depth of discharge |
| ECR | electrochemical reactor |
| ESA | electrochemical surface area |
| FP | fast prototyping |
| GDE | gas diffusion electrode |
| GUI | graphical user interface |
| HCF | hex-cyanoferrate |
| HEV | hybrid electric vehicles |
| HSE | horizontal segmented electrode |
| IAB | Iron air batter |
| ICV | internal combustion vehicle |
| ICR | iron to carbon ratio |
| KB | Ketjenblack |
| LSFCO | $La_{0.6}Sr_{0.4}Fe_{0.8}Co_{0.2}O_3$ |
| MAB | metal air battery |
| MDC | mean discharge capacity (mA h) |
| NECOBAUT | new concept of metal-air battery for automotive application |
| OER | oxygen evolution reaction |
| ORR | oxygen reduction reaction |
| PEM | proton exchange membrane |
| SEM | scanning electrode microscope |
| SHE | standard hydrogen electrode |

# Symbols

| | |
|---|---|
| A $h_{Fe}$ | Ampere h per gram of iron |
| $E^0$ | standard potential / V |
| $E_a$ | anode potential vs SHE / V |
| $E_c$ | cathode potential vs SHE / V |
| $E_{cell}$ | cell voltage / V |
| $E_{cut\ off}$ | cut off potential / V |
| $E^e_{cell}$ | equilibrium cell potential / V |
| $F$ | Faradays constant 96,485 C $mol^{-1}$ |
| $I$ | electric current / A |
| $J$ | electric current density |
| M | Molar concentration, mol/L |
| $P$ | power / W |
| $Q$ | electric charge / A h |
| $R_e$ | total resistance / Ω |
| $V$ | voltage between the electrodes / V |
| $\alpha, \beta, \gamma, \delta$ | stoichiometric coefficients |
| $\Delta_r G^0$ | Gibbs free energy under standard conditions / J $mol^{-1}$ |
| $\eta_G$ | gravimetric energy density / W h $kg^{-1}$ |
| $\eta_V$ | volumetric energy density / W h $m^{-3}$ |
| $\eta$ | over potential / V |

# Chapter 1: Objectives, publications, and research paths

In this initial chapter, the description of the main objectives and milestones of this Ph.D. research project are presented. This information should help the reader to have in mind the various stages that were part of this research and will be useful to understand in a logical way the structure of the subsequent chapters.

In this first chapter, the description of the relevant publications that arouse as part of this research are outlined. In these publications, a more concise presentation of the main results can be found, and the reader is encouraged to revise these publications in parallel to the work presented in this thesis to achieve a wider outlook of the research project.

## 1.1 Foreword

I started the present Ph.D. research on the iron air battery (**IAB**) electrochemical system on November 2014 following a M.Sc. in sustainable energy technologies. At that time, this research aligned to an outgoing European collaboration denominated **NECOBAUT** that stands for "Novel conceptual metal air battery for automotive propulsion" [1,2].

During the first stage of my Ph.D. I focused in the engineering design of a laboratory cell prototype that could be used to test in-house gas diffusion electrode (**GDE**) and hot pressed iron electrodes (**HPIE**) supplied by one of our research collaborators. Part of the engineering design activities during this phase included: (1) the design of a 5 cell stack, (2) scaling up of a laboratory cell to test larger electrodes (3) to characterise the current density distribution of a flow cell [3]. Most of these results form part of the main body of chapter 7.

Having finished the engineering design part of my Ph.D. I focused on the electrochemistry characterisation studies, which led me to join an existing line of research to further the development of novel GDE using Pd over carbon black (**Pd/C**) as a bifunctional catalyst for both the oxygen reduction reaction (**ORR**) and the oxygen evolution reaction (**OER**) [4]. Following this research path, I learned

how to manufacture in-house GDE and to characterise the performance of bifunctional catalysts, including a combination of Pd/C, with Ni-Fe hex-cyanoferrate (**HCF**) and $La_{0.6}Sr_{0.4}Fe_{0.8}Co_{0.2}O_3$ (**LSFCO**)-perovskite, which later on enabled the development of two collaborative publications [5,6] where the electrochemical performance of these formulations was detailed. To further these studies, computer assisted tomography was performed to learn about the mesoporous structure of GDE. In chapter 4 these results are described more in detail.

Afterwards my research focused in the performance of the iron electrode. An in-depth literature review of the iron electrode, showed that there were many experiments that could be performed to improve the discharge capacity of HPIE, these experiments included (1) testing different iron active materials in HPIE, (2) mixing the iron active material with carbon in different proportions and (3) to determine if the ball-milling mixing process improves the performance of HPIE. These experiments form part of the main body of chapter 3 which has led to draft two publications that will be in preparation at the time the thesis is submitted (Nov 2018).

The main results of this Ph.D. will be the characterisation of the whole IAB system, these results have been published in [7] where the performance of both electrodes in their respective half-cell configurations and the performance of the IAB as a whole is presented. These results are the main substance of chapter 8

The reader will find the following thesis structure. Chapter 2, chapter 3 and chapter 4 are introductory chapters to the IAB system. Chapter 2 is a brief introduction to electrochemical energy technologies, and a revision of metal air batteries focusing on the operation principles of the iron air battery electrochemical system. Chapter 3 and chapter 4 correspond to the detailed literature review associated to both the iron electrode and gas diffusion electrodes respectively.

The main laboratory results and the associated laboratory methodology and discussion are presented in chapters 5, 6, 7 and 8. Chapter 5 presents the results and experiments associated with the iron electrode performance, in a similar way in chapter 6 the respective results to the GDE are discussed. In chapter 7 the focus is put over the engineering design aspect of the laboratory prototypes, cell stacks and

scaling up the system using additive manufacturing (3D printing). Finally in chapter 8, the main results associated to the performance of both, iron and air electrodes working together in an IAB configuration is presented. In chapter 9, the concluding remarks, future lines of research together with the limitations and future opportunities for the IAB are highlighted.

The strategies and time management that were followed can be analysed from the Gantt diagram that is presented at the Appendix B.

## 1.2 Objectives

As my Ph.D. research progressed various objectives and milestones were outlined. The most relevant ones can be listed as:

1. ***To carry out an extensive literature review aiming to gain an in depth understanding of the iron air battery electrochemical system***. This objective implied: learning the fundamental electrochemistry principles, familiarize with the relevant laboratory techniques in electrochemistry, becoming knowledgeable about the various battery materials used as active materials, binders, separators, cell cases, current collectors, electrolyte, support materials and additives.
2. ***To design and develop an IAB laboratory scale prototype***: The design must be optimized to place all the elements of the battery together. The design must be impermeable to avoid leaks and should allow the evolved gas to escape to avoid evolved bubbles from interfering with the performance of the battery. At the same time, it should be as light as possible and should allow different reproducible experimental configurations.
3. ***To manufacture and test in-house bi-functional air electrodes***: The air electrodes use carbon as a support material given its high surface area to distribute the catalyst layer. This task would require determining the right proportion of binder to achieve the right balance between hydrophobicity and hydrophilic properties to allow oxygen to reach the catalytic material whilst holding the electrolyte from leaking; for the oxygen reduction reaction $O_2$ should be supplied to the back of the air electrode, and for the oxygen evolution $O_2$ should be able to escape rapidly; a nickel mesh can be

used as current collector to improve its conductivity, the work described in [4] were used as a starting point to develop GDE in the laboratory.

4. ***To characterise the performance of the battery cell using the iron electrodes supplied by the partners of the NECOBAUT collaboration and the in-house air electrode***: To measure the charge-discharge profiles of the IAB cell to determine the energy density, capacity, and efficiency of the battery under different current density rates aiming to improve its performance.
5. ***To design a 5 IAB cells stack***. Once the laboratory cell was developed it was suggested to design a stack that was able to connect at least 5 cells in series to power a small DC electric motor as proof of concept.
6. ***To scale up the IAB laboratory cell from 25 cm$^2$ electrodes to 100 cm$^2$.*** Scaling up the electrodes to gain insight on the potential engineering problems that may be found when scaling up the cell components.
7. ***To test and compare the electrochemical performance of various electro-catalyst such as Pd/C, Ni-Fe HCF, LSFCO perovskite and optimise their loadings in our in-house GDE.*** Since promising results were obtained with the in-house prepared GDE it was decided to continue that line of research using different catalysts and further experiments to determine the optimum loading.

## 1.3 Publications resulting from this research

The main results of this Ph.D. project have led to the development of the following collaborative publications:

1. R.D. McKerracher, H.A. Figueredo-Rodríguez, C. Ponce De León, C. Alegre, V. Baglio, A.S. Aricò, F.C. Walsh, A high-performance, bifunctional oxygen electrode catalysed with palladium and nickel-iron hexacyanoferrate, Electrochim. Acta. 206 (2016) 127–133. doi:10.1016/j.electacta.2016.04.090. [5]

   In this publication, it is reported the performance of GDE using a combination of a previously reported Pd/C catalyst [4], but this time in combination with a Ni-Fe HCF catalyst that showed an increased electro catalytic activity towards the oxygen evolution reaction. The combination of both catalyst in GDE for the

IAB system was the main aspect reported in this publication. My participation in this paper was performing the required electrochemical experiments including the cyclic voltammetry, charge-discharge profiles and the rotating disk electrode measurements reported in this experiment.

2. H.A. Figueredo-Rodríguez, R.D. McKerracher, C. Ponce de León, F.C. Walsh, Current distribution in a rectangular flow channel manufactured by 3-D printing, AIChE J. 63 (2017) 1144–1151. doi:10.1002/aic.15454. [3]

Part of this research required to design various laboratory prototypes to test the electrodes, and to comply the objectives associated to our collaboration with the NECOBAUT project, this included to carry out the characterisation of a flow cell that could be used for the IAB system. In this paper different flow channel geometries were tested and, in each case, the current density distribution over the electrodes was reported to improve the design of the cell components. My collaboration in this paper included doing all the laboratory experiments and as the first author to outline the structure of this publication including the preliminary drafts and the associated proofreading and improvements in the subsequent versions.

3. H.A. Figueredo-Rodríguez, R.D. McKerracher, M. Insausti, A.G. Luis, C.P. de León, C. Alegre, V. Baglio, A.S. Aricò, F.C. Walsh, A rechargeable, aqueous iron air battery with nanostructured electrodes capable of high energy density operation, J. Electrochem. Soc. 164 (2017) A1148–A1157. doi:10.1149/2.0711706jes. [7]

This paper summarizes the main results associated to the performance of the IAB. This paper includes the performance of both half-cell configurations independently, and the performance of both the iron and GDE working together in a battery configuration. The design considerations of the cells that were used in the project were also included. My collaboration in this publication includes the outline of the original draft and to update the improvements and amendments done by our other collaborators. I did in collaboration with the research fellow in the project to set up the required electrochemical experiments presented in this publication. I did as well all the engineering design aspects associated to the results presented in this publication.

4. R.D. McKerracher, H.A. Figueredo-Rodríguez, J.O. Avila-Alejo, K. Kwasnicki, C.P. de León, C. Alegre, V. Baglio, A.S. Aricò, F.C. Walsh, A

Comparison of Pd/C, Perovskite, and Ni-Fe Hexacyanoferrate Bifunctional Oxygen Catalysts, at Different Loadings and Catalyst Layer Thicknesses on an Oxygen Gas Diffusion Electrode, J. Electrochem. Soc. 165 (2018) A1254–A1262. doi:10.1149/2.0321807jes. [6]

This paper follows the GDE line of research testing a novel bifunctional catalyst, LSFCO-perovskite, and to compare its performance with the ones that were previously reported, Pd/C and Ni-Fe HCF. The optimum loading of catalyst was also investigated. My collaboration was co-supervising the electrochemical characterisation and manufacture of the GDE and performing as well some of the characterisation studies including the scanning electron micrographs of the GDE samples.

The following two publications will present our findings when testing various iron electrode formulations, there are at the moment in preparation.

5. H.A.F. Rodríguez, R.D. McKerracher, C.P. de León, F.C. Walsh, Improvement of Negative Electrodes for Iron-Air Batteries: Comparison of Different Iron Compounds as Active Materials, J. Electrochem. Soc. 166 (2019) A107–A117. doi:10.1149/2.1071816jes. [8]

In this paper the discharge capacity of different iron active material for hot pressed iron electrode was investigated and reported. This paper compares as well our in-house HPIE and similar ones reported in the literature. My contribution in this paper was to plan in advance the materials to test based on an extensive literature review, to carry out the charge-discharge cycles, and to contribute with SEM characterisation of the materials before and after being cycled for various cycles.

6. H.A. Figueredo-Rodríguez, R.D. McKerracher, C. Alegre, A.S. Aricò, V. Baglio, C.P. de León, F.C. Walsh, Improvement of $Fe_2O_3$/C formulations for hot pressed iron electrodes. In prep

In collaboration with our Italian partners it was possible to improve the discharge capacity performance of HPIE using hematite dispersed over high surface carbon black, the difference is that this dispersion resulted from the synthesis process of the material, which lead to an improved discharge capacity performance.

# Chapter 2: The iron air battery electro-chemical system

The energy demand of modern society is one of the most challenging engineering problems faced by the actual energy infrastructure. Finding a solution to satisfy an increasing energy demand, without compromising the environment for future generations will require transforming our energy supply in such a way that allows a greater contribution from renewable energy sources whilst reducing the greenhouse gas emissions. At the same time the current energy conversion systems needs to adopt new technologies to become more versatile and efficient.

Novel electrical energy storage technologies are needed in order to allow renewable energy sources to contribute a greater percentage of the energy generation mix. Renewable sources such as solar, wind, tidal and wave are mostly stochastic and are characterised by their intermittency and variability over time. Because of this, it is not possible to ensure that the power generation will coincide with the load demand unless it is coupled with a suitable energy storage technology [9,10].

Efforts in different areas of research have been addressed to study and develop novel energy storage technologies. Using mechanical principles there are various categories of energy storage technologies including pumped hydro, compressed air and flywheels. In the particular case of electrochemistry energy storage, batteries, fuel cells and electrochemical capacitors are the main existing technologies for this use.

A battery delivers electrical energy [Joules] relying on an ongoing electrochemical reaction, whilst a capacitor relies on the geometry and the dielectric properties of the media that determines its capacitance [Farads] to store electric charge (Coulombs). How fast a battery can deliver its stored energy depends on the kinetics of the involved electrochemical reaction, on the other hand a capacitor can be discharged almost instantly delivering high power [Watts]. Somewhere in between, an electrochemical-capacitor makes use of its inherent capacitance in combination with a rapid electrochemical reaction occurring on its surface to increase its storage capacity. *Grosso modo*, a battery can deliver ten to fifty times the energy density of

a capacitor but capacitors can deliver ten to hundred times the power density of a normal battery [11]. That is why it has been suggested that depending on the application a hybrid system batteries-capacitor might be the way to deliver the power and energy densities required circumventing the limitations that some electrochemical systems may have on their own [12].

Ubiquitous available batteries including lithium-ion, nickel/cadmium, nickel/metal-hydride and lead-acid batteries have their own merits depending on the application. Nevertheless, any of these energy storage technologies can be said to be the best option for all applications, including the most demanding ones such as electric vehicles and large grid energy storage. Therefore, novel electrochemical systems that make use of more abundant, safe and environmentally friendly materials to develop new batteries types are needed to take further the development of these applications.

Among the various electrochemical systems, fuel cells, flow cells and metal air batteries have been highlighted for many years for its high theoretical energy density in comparison with other batteries chemistries. The present work focuses on the aqueous iron-air electrochemical system due to the low cost, abundance and the fact that iron can be electrodeposited in aqueous solution which enables this system to work as a rechargeable battery [13].

In this chapter a brief literature review to set the panorama for the IAB research is outlined, this literature review includes a primer on the types of batteries that exist commercially at the present time and a theoretical comparison of various rechargeable battery chemistries to compare what is in principle the potential and limitations of iron-air and other metal air batteries systems. Thereafter the focus will be put upon the IAB system as a whole, including the history of its development and the reported experiences and results reported by previous research groups that have focused in developing this battery.

## 2.1 Energy density of electrochemical couples

The principle of operation of any battery implies two simultaneous electrochemical reactions, one occurring at the anode surface and another at the cathode surface. Equation (1) represents a general electrochemical reaction involving the transfer of $n$ electrons at the cathode while equation (2) is the corresponding electrochemical reaction occurring at the anode: [14]

$$\alpha A + ne^- \rightarrow \beta B \quad E^0 = E_c \; vs \; SHE \qquad Eq.\ (1)$$

$$\gamma C \rightarrow \delta D + ne^- \quad E^0 = E_a \; vs \; SHE \qquad Eq.\ (2)$$

As a result of these two electrochemical reactions taking place at each electrode, the overall cell reaction can be written as:

$$\alpha A + \gamma C \rightarrow \beta B + \delta D \quad E^0_{cell} = E_c - E_a \qquad Eq.\ (3)$$

To determine the useful available energy from equation (3), the Gibbs free energy under standard conditions $\Delta_r G^0$ can be calculated as the difference of standard formation energies between reactants and products $\Delta_f G^0$. Thus, the maximum theoretical available energy during reaction (3) is given by:

$$\Delta_r G^0 = \left(\beta \Delta_f {G_B}^0 + \delta \Delta_f {G_D}^0\right) - \left(\alpha \Delta_f {G_A}^0 + \gamma \Delta_f {G_C}^0\right) \qquad Eq.(4)$$

Furthermore, using the Nernst equation (5) at standard conditions (T=298 C and both [Red] and [Ox] being 1.0 M)

$$E = E^0 - \frac{RT}{nF} ln\left(\frac{[Red]}{[Ox]}\right) \qquad Eq.(5)$$

The maximum electrical work would be given by the product of the potential and the total charge ($nF$), which is equal to free Gibbs energy (4). By equating (4) and ($nFE$), it is possible to relate the standard equilibrium potential, ($E^0$) to the Gibbs free energy under standard conditions ($\Delta_r G^0$) [15],

$$\Delta_r G^0 = -nFE^0 \qquad Eq.(6)$$

By dividing $\Delta_r G^0$either by the mass or volume of the reactants (A and C), it is possible to obtain the theoretical gravimetric or volumetric energy density respectively,

$$\eta_G = \frac{\Delta_r G^0}{\sum M} \qquad Eq.(7) \qquad\qquad \eta_V = \frac{\Delta_r G^0}{\sum V} \qquad Eq.(8)$$

Expressions (7) and (8), allow the comparison of various electrochemical systems from standard Gibbs free energy or equilibrium potential tables such as those reported in references [16–20].

The change of standard free energy of a cell reaction is the driving force for the system to deliver energy to an external circuit. The measurement of the cell potential is at the same time an indirect way to measure the change in Gibbs free energy using (6).

Various studies use similar expressions to set a baseline and to highlight potential electrochemical systems to develop novel batteries. For example in [15], the authors have made a thermodynamic comparison of 1,172 electrochemical couples. Among them, the $Li/F_2$ battery has in principle the highest specific energy density while the $Li/O_2$ ranks as the second with 6,294 W h $kg^{-1}$ and 5,217 W h $kg^{-1}$ respectively as is shown in Figure 1. It must be mentioned that these numbers do not take into account other important factors to address the feasibility of a system such as: stability and availability of the active materials, kinetic considerations, relative abundancy of a material, cost, toxicity or safety. Nevertheless, this approach is insightful to understand the theoretical performance of any electrochemical system.

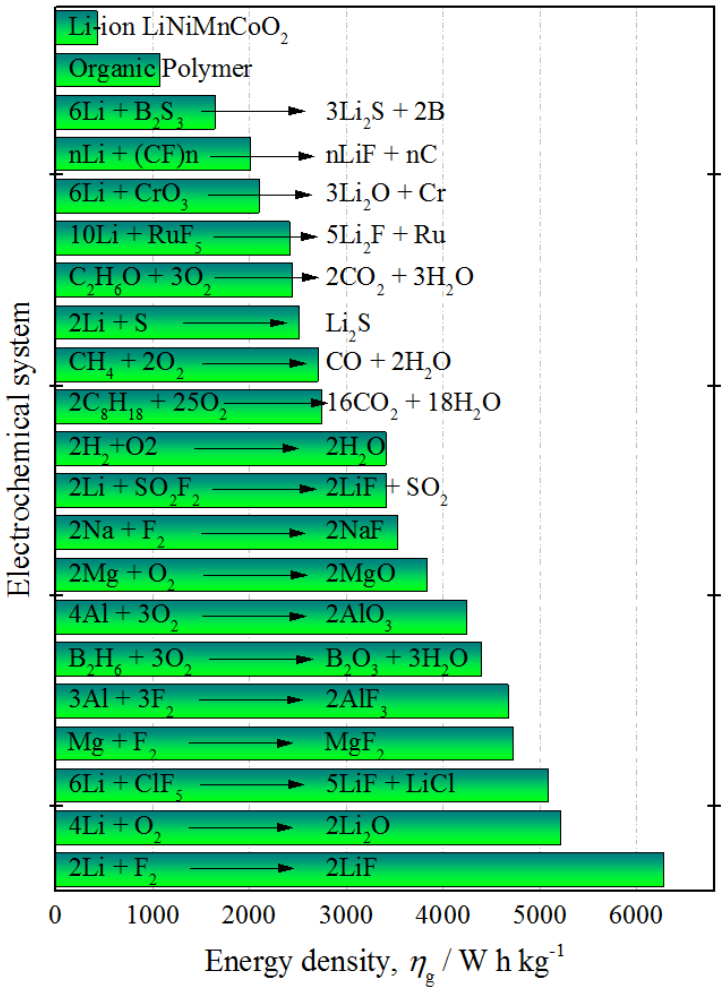


Figure 1. Theoretical standard energy densities for electrochemical systems according to the Nernst Equation [15].

The capacity of a real battery will depend on the amount of active materials that contains within. In practice, only a fraction of the theoretical specific energy values can be achieved due to the need of passive components such as, cell containers, connectors, separators, pumps that add weight to the overall system.

Thermodynamics and first principles are useful to have an initial estimation of the order of magnitude of the upper limit performance of an electrochemical system. In practice, the battery cell voltage never coincides with the standard equilibrium potential, nor is it discharged to zero volts (due to anode and cathode the activation overpotentials and the associated ohmic losses). Additionally, in a normal battery, the active materials rarely are stoichiometrically balanced; this implies that there will always be an excess amount of one of the active materials. Besides, like in any other electrical circuit there will Ohmic losses related to the inherent impedance of

the various components of the battery. Finally, specific challenges related to each one of the electrochemical systems have to be addressed individually in order to determine the real performance of the system such as power density, operation requirements and life cycle [21].

In general terms, the measured potential of a cell, can be expressed as:

$$E_{cell} = E_{cell}^{e} - \sum|\eta| - \sum|IR_e| \qquad Eq.\ (9)$$

Where $E_{cell}$ refers to the observed cell potential while $E_{cell}^{e}$ refers to the equilibrium cell potential. $\sum|\eta|$ is the sum of the activation over potentials at each electrode, and $\sum IR_e$ refers to the various ohmic losses at each of the elements in the cell ($R_e$ refers to the equivalent resistance of the whole system). At this point, it is worth mentioning that the last two terms are dependent on the applied current density.

Broadly speaking, depending on the operation conditions, the performance of the cell may be limited by either the electron transfer kinetics or by mass transport phenomena in addition to the expected ohmic losses. As a rule of thumb at low current-densities the electron-transfer-kinetics at the electron-transfer-site is the rate limiting phenomenon, whilst at high current-densities the mass transport of the ionic species from the bulk of the electrolyte to the surface becomes the limiting phenomenon. The detailed description of these phenomena can be found in classic electrochemistry books [22–25] .

### 2.1.1 Types of batteries

There are various classifications for batteries depending on the type of chemistry, cell design or depending if they can be mechanically or electrically recharged. However, it is usual to make a first classification in primary and secondary depending on their ability to be electrically recharged or not, Linden in [21] suggest the following classification:

- ***Primary batteries***: These batteries are not effectively recharged electrically. This type of batteries are disposed once they have been used. Many primary

cell have the electrolyte adsorbed on a separator material and are termed "dry cells".

- ***Secondary or rechargeable batteries***: These batteries can be electrically recharged, after they have been discharged by passing a current through them in an opposite direction to that of the discharge current, sometimes they are referred as well as "storage batteries" or "accumulators". Some batteries known as "mechanically rechargeable batteries" can be recharged by replacing one depleted electrode, usually the metal anode with a fresh one like in some metal air batteries. Mechanically rechargeable batteries operate essentially as a primary battery but the design includes features to conveniently replace one of the electrodes in a fast and easy way.
- ***Reserve batteries***: In this type of batteries, a key component is isolated from the rest of the battery prior to activation in order to eliminate self-discharge or chemical deterioration of the system prior to use. These batteries are intended for long-term energy storage. Reserve battery design aims to meet some extremely long or environmentally severe storage requirements that cannot be meet with an "active" battery. These batteries are usually used to deliver high power for short periods, for example in missiles, torpedoes and rockets.
- ***Fuel cells***: Fuel cells are similar to batteries except that the active materials are not an integral part of the device (as in a battery), but are fed into the fuel cell from an external source when required, and only operate in discharge mode. In principle, a fuel cell could work as long as it is feed with the required fuel. In practice at some point, deterioration of its components will determine the lifetime of the fuel cell.

### 2.1.2 Major secondary electrochemical systems

It is possible to compare various electrochemical systems in a theoretical basis using equations (5-8). By further research, it is possible to determine how reversible an electrochemical is using cycling voltammetry (**CV**) and comparing how far the reduction and oxidation peaks are.

If the electrochemical reactions involved have good electrochemical reversibility (*i*.e. if in a CV the separation between the oxidation and the reduction peaks is

small) and if they occur reasonable fast and in a controlled way they could lead to the development of a secondary battery.

The combination of materials to store energy and the operational reaction-rate-range will determine if a system can deliver the energy and power energy requirements for a particular application. Further analysis considering the degradation of materials, the expected lifetime of the electrodes, the life cycle together with safety considerations will determine if an electrochemical system can be used in a particular application, or alternatively the characterisation of a novel electrochemical system will allow determining what type of application it is suitable for.

Some of the most commonly found secondary batteries at the present time are:

***Lead-acid batteries***: It is the oldest rechargeable battery, specific energy (40-50 W h $kg^{-1}$), limited cycle count (200-300 cycles at 80% DoD). Some common applications include: cars ignition systems, wheelchairs, emergency lighting, golf cars and uninterruptible power supply (UPS). It is not easily disposed since lead is toxic, but some of its components can be recycled. This type of batteries can withstand overcharge and have a relatively low self-discharge (5%).

This type of battery should be called lead (Pb)/lead oxide batteries ($PbO_2$), the electrochemical reactions taking place in this systems are [25]:

At the negative electrode:

$$Pb \rightleftarrows Pb^{2+} + 2e^- \qquad Eq.(10)$$

$$Pb^{2+} + SO_4^{2-} \rightleftarrows PbSO_4 \qquad Eq.(11)$$

At the positive electrode:

$$PbO_2 + 4H^+ + 2e^- \rightleftarrows Pb^{2+} + 2H_2O \qquad Eq.(12)$$

$$Pb^{2+} + SO_4^{2-} \rightleftarrows PbSO_4 \qquad Eq.(13)$$

The overall cell reaction can be seen in table 1, it is interesting to observe that in this battery during discharge both electrodes turn to lead sulphate.

***Nickel-cadmium***: Long life, high discharge rates (1-20 C rate), most enduring batteries, ultra-fast charging with not much deterioration of its components. Usually

used for power tools, medical devices, aviation, and UPS. When possible it is avoided due the inherent cadmium toxicity, but is a mature and well-understood reliable battery, specific energy (45-80 W h $kg^{-1}$). Similar as before the overall cell reaction for this system can be seen in table 1, row 3, at the Cd negative electrode Cd is oxidised to $Cd(OH)_2$ and Nickel oxyhydroxide (NiOOH) is reduced to $Ni(OH)_2$.

***Nickel-metal hydride***: This rechargeable battery is a good alternative to the reliable nickel cadmium batteries in terms of safety since this way it is possible to avoid the toxicity problems related to the use of cadmium. These batteries have a similar specific energy (60-120 W h $kg^{-1}$). Recycling these batteries is profitable given the high content of nickel. Unfortunately, its coulombic efficiency is not very high (65%), they suffer from high self-discharge and requires a special charging protocol since they are sensitive to overcharge. The electrochemical reaction of this system can be found in table 1 row 6, in this type of battery during discharge.

The active material in the positive electrode is nickel hydroxide (discharged state) while the negative electrode is an alloy capable to store hydrogen usually of the form $AB_5$ or $AB_2$ type where $AB_x$ refers to the ratio of the A type (LaCePrNd or TiZr) elements o the B type elements (VNiCrCoMnAlSn) [25].

***Lithium-ion***: Under the label of lithium ion batteries there are a number of different types of formulations most of them use a graphite anode but they differs in the formulation of their cathodes. The better-known ones are lithium cobalt oxide (LCO), lithium manganese oxide ($LiMn_2O_4$), and lithium iron phosphate ($LiFePO_4$). Their high coulombic efficiency (99%) and higher energy densities (90-250 W h $kg^{-1}$) gives these batteries a superior performance, nevertheless they do required a protection circuit to avoid thermal runaway and are more expensive than many other secondary batteries but in principle they can achieve a lower cost per cycle.

In Table 1 various major secondary battery systems are presented for comparison.

Table 1. Major secondary batteries ele4ctrochemical systems overall cell reactions (⟶ discharge, ⟵ charge)

| | | | | Theoretical[1] | | | Practical Battery[2] | | |
|---|---|---|---|---|---|---|---|---|---|
| **Electrochemical System** | **Anode** | **Cathode** | **Overall reaction** | **V** | **A h kg$^{-1}$** | **W h kg$^{-1}$** | **V** | **W h kg$^{-1}$** | **W h dm$^{-3}$** |
| Lead-acid | Pb | $PbO_2$ | $Pb + PbO_2 + 2H_2SO_4 \rightleftarrows 2PbSO_4 + 2H_2O$ | 2.1 | 120 | 252 | 2 | 35 | 70[3] |
| Edison | Fe | Ni oxide | $Fe + 2NiOOH + 2H_2O \rightleftarrows 2Ni(OH)_2 + Fe(OH)_2$ | 1.4 | 224 | 314 | 1.2 | 30 | 55[3] |
| Nickel-cadmium | Cd | Ni oxide | $Cd + 2NiOOH + 2H_2O \rightleftarrows 2Ni(OH)_2 + Cd(OH)_2$ | 1.35 | 181 | 244 | 12 | 40 | 135[4] |
| Nickel-zinc | Zn | Ni oxide | $Zn + 2NiOOH + 2H_2O \rightleftarrows 2Ni(OH)_2 + Zn(OH)_2$ | 1.73 | 215 | 372 | 1.6 | 90 | 185 |
| Nickel-hydrogen | $H_2$ | Ni oxide | $H_2 + 2NiOOH \rightleftarrows 2Ni(OH)_2$ | 1.5 | 289 | 434 | 1.2 | 55 | 60 |
| Nickel-metal hydride | MH | Ni oxide | $MH + NiOOH \rightleftarrows M + Ni(OH)_2$ | 1.35 | 178 | 240 | 1.2 | 100 | 235[4] |
| Silver-zinc | Zn | AgO | $Zn + AgO + H_2O \rightleftarrows Zn(OH)_2 + Ag$ | 1.85 | 283 | 524 | 1.5 | 105 | 180[3] |
| Silver-cadmium | Cd | AgO | $Cd + AgO + H_2O \rightleftarrows Cd(OH)_2 + Ag$ | 1.4 | 227 | 318 | 1.1 | 70 | 120[3] |
| Zinc/chlorine | Zn | $Cl_2$ | $Zn + Cl_2 \rightleftarrows ZnCl_2$ | 2.12 | 394 | 835 | | | |
| Zinc/bromine | Zn | $Br_2$ | $Zn + Br_2 \rightleftarrows ZnBr_2$ | 1.85 | 309 | 572 | 1.6 | 70 | 60 |
| Lithium-ion/cobalt dioxide | $LiC_6$ | $Li_{(i-x)}CoO_2$ | $Li_xC_6 + Li_{(1-x)}CoO_2 \rightleftarrows LiCoO_2 + C_6$ | 4.1 | 109 | 448 | 3.8 | 200 | 570[4] |
| Lithium-ion/manganese dioxide | $LiC_6$ | $MnO_2$ | $Li + Mn^{IV}O_2 \rightleftarrows Mn^{IV}O_2(Li^+)$ | 3.5 | 286 | 1001 | 3 | 120[5] | 265[5] |
| Lithium-ion/iron disulphide | Li(Al) | $FeS_2$ | $2Li(Al) + FeS_2 \rightleftarrows Li_2FeS_2 + 2Al$ | 1.73 | 285 | 493 | 1.7 | 180[5] | 350[5] |
| Sodium/sulphur | Na | S | $2Na + 3S \rightleftarrows Na_2S_3$ | 2.1 | 377 | 792 | 2 | 170[5] | 345[5] |
| Sodium/nickel chloride | Na | $NiCl_2$ | $2Na + NiCl_2 \rightleftarrows 2NaCl + Ni$ | 2.58 | 305 | 787 | 2.6 | 115 | 190 |

[1] The theoretical values considered the mass of the anode and cathode only it does not consider the mass of the potential electrolyte or additional electrode materials.
[2] These values are for single-cell batteries, with discharge rates optimized for energy density, using midpoint voltage.
[3] Prismatic battery.
[4] Cylindrical spiral wound battery
[5] Based on cell performance

## 2.2 Metal air batteries

Metal air batteries (**MAB**) exploit the possibility to use oxygen taken directly from air as one of the active materials, this implies that only one of the active components have to be contained within the battery and this could lead to higher specific energy density batteries. Besides this type of batteries would only be limited by the amount of active material at the anode that could always react completely given the virtually infinity supply of oxygen from air.

As a fist approximation a MAB will consist of a metal anode, a gas diffusion electrode where the oxygen reactions are catalysed, both in ionic contact via a suitable electrolyte. In this type of batteries, the metallic anode is oxidized to metal hydroxides in alkaline media whilst oxygen is reduced to oxygen-containing species within the electrolyte. This idea is schematically presented in Figure 2.

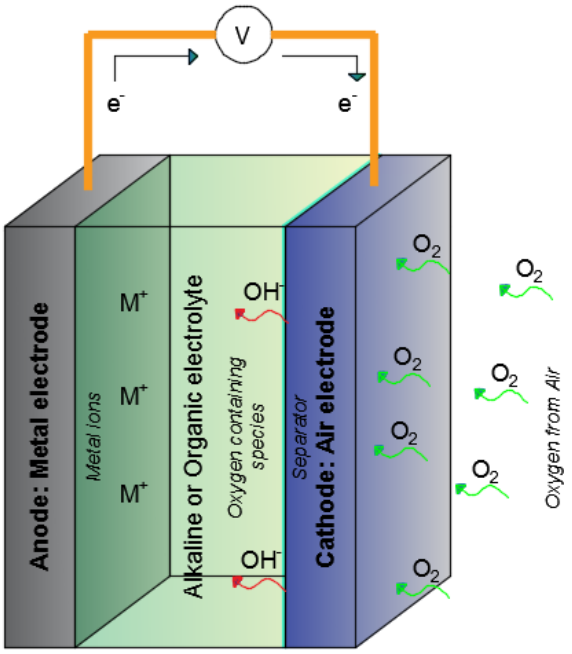


Figure 2. MAB schematic during discharge. The active materials in a MAB are a metallic anode and the oxygen taken directly from atmospheric air.

Depending on the metal anode choice there are potentially as many MABs as metals there are. In general terms the electrochemical reactions occurring at the anode in any MAB during the discharge can be written as [26]:

$$\frac{n}{z}M + nOH^- \longrightarrow \frac{n}{z}M(OH)_z + ne^- \qquad Eq.(14)$$

Here, $M$ represents the metal, $n$ the number of electrons exchanged, and $z$ is the valence of the metal in the resulting hydroxide.

The other half-cell reaction during the discharge cycle corresponds to the oxygen reduction reaction at the cathode equation (15),

$$O_2 + 4e^- + 2H_2O \longrightarrow 4OH^- \qquad E_0 = 0.401\,V \;\; vs\; SHE \qquad Eq.(15)$$

The cell potential is given by equation (16):

$$E_{cell} = E_{cathode} - E_{anode} \qquad Eq.(16)$$

Therefore, the overall cell reaction can be written as:

$$\frac{4}{z}M + O_2 + 2H_2O \longrightarrow \frac{4}{z}M(OH)_z \qquad Eq.\ (17)$$

In principle, any metal that undergoes a similar oxidation to hydroxide could be used as a metal air battery in equation (17). The electrochemical reactions of some metal-air systems can be seen in Table 2 with their correspondent anode reactions and their respective equilibrium potentials.

Table 2. Metal air/$O_2$ batteries anode and overall cell reactions.

| Metal | Anode Reaction | Overall Cell Reaction |
|---|---|---|
| *Li* | $Li + OH^- \longrightarrow LiOH + e^-$ <br> $E_0 = -3.05\ V\ vs\ SHE$ | $Li + \frac{1}{2}O_2 + H_2O \longrightarrow 2LiOH$ <br> $E_{\text{cell}} = -3.451\ V$ |
| *Ca* | $Ca + 2OH^- \longrightarrow Ca(OH)_2 + 2e^-$ <br> $E_0 = -3.01\ V\ vs\ SHE$ | $2Ca + O_2 + 2H_2O \longrightarrow 2Ca(OH)_2$ <br> $E_{\text{cell}} = -3.411\ V$ |
| *Mg* | $Mg + 2OH^- \longrightarrow Mg(OH)_2 + 2e^-$ <br> $E_0 = -2.69\ V\ vs\ SHE$ | $2Mg + O_2 + 2H_2O \longrightarrow 2Mg(OH)_2$ <br> $E_{\text{cell}} = -3.901\ V$ |
| *Al* | $Al + 3OH^- \longrightarrow Al(OH)_3 + 3e^-$ <br> $E_0 = -2.30\ V\ vs\ SHE$ | $2Al + \frac{3}{2}O_2 + H_2O \longrightarrow 2Al(OH)_3$ <br> $E_{\text{cell}} = -2.701\ V$ |
| *Zn* | $Zn + 2OH^- \longrightarrow Zn(OH)_2 + 2e^-$ <br> $E_0 = -1.25\ V\ vs\ SHE$ | $2Zn + O_2 + 2H_2O \longrightarrow 2Zn(OH)_2$ <br> $E_{\text{cell}} = -1.651\ V$ |
| *Fe* | $Fe + 2OH^- \longrightarrow Fe(OH)_2 + 2e^-$ <br> $E_0 = -0.88\ V\ vs\ SHE$ | $2Fe + O_2 + 2H_2O \longrightarrow 2Fe(OH)_2$ <br> $E_{\text{cell}} = -1.281\ V$ |
| *Cd* | $Cd + 2OH^- \longrightarrow Cd(OH)_2 + 2e^-$ <br> $E_0 = -0.87\ V\ vs\ SHE$ | $2Cd + O_2 + 2H_2O \longrightarrow 2Cd(OH)_2$ <br> $E_{\text{cell}} = -1.271\ V$ |
| $O_2$ | ***Cathode:*** $O_2 + 4e^- + 2H_2O \longrightarrow 4OH^-$ $E_0 = 0.401\ V\ \ vs\ SHE$ | |

The oxygen reduction reaction presented previously in equation (15) is the same in all MABs. The resulting MAB cell potential is given by equation (17). For example, for the iron-air battery couple the cell potential would be $E_{iron/air} = E_{O_2} - E_{iron} = 0.401\ V - (-0.88\ V) = 1.28\ V$.

In Table 3 some parameters including the standard cell potential, gravimetric and volumetric specific energies and specific capacity of various metal air batteries are presented. From this data it is appreciable that the *Li-air*, *Al-air*, *Mg-air*, and *Ca-air* systems have the potential to deliver high cell voltages. Unfortunately developing these systems in aqueous solutions is unviable since these metallic elements electrodeposit at very negative potentials, which implies the need of an ionic liquid or a non-aqueous electrolyte with a wider potential window than aqueous solutions [27].

Table 3. Metal air/oxygen cells characteristics.

| **Metal-air couple** | **Cell voltage theoretical / V** [13] | **Gravimetric energy density $\sum M$ =metal / W h kg$^{-1}$** | **Gravimetric energy density $\sum M$ =reactants excepting $O_2$ / W h kg$^{-1}$** | **Volumetric energy density $\sum V$ =reactants excepting $O_2$ / W h dm$^{-3}$** | **Specific energy density / m A h g$^{-1}$** |
|---|---|---|---|---|---|
| **Li-air** | 3.45 | 12741 | 3692 | 5390 | 3861 |
| **Al-air** | 2.70 | 8046 | 2786 | 6854 | 2980 |
| **Mg-air** | 3.09 | 6837 | 2850 | 6669 | 2205 |
| **Ca-air** | 3.42 | 4547 | 2458 | 5432 | 1337 |
| **Fe-air** | 1.28 | 1248 | 764 | 2598 | 960 |
| **Zn-air** | 1.65 | 1312 | 863 | 2635 | 820 |
| **Cd-air** | 1.27 | 572 | 439 | 2103 | 478 |

When reporting the theoretical energy densities of MAB some authors consider only the ***mass of the metal*** involved in the reaction when taking the ratio in equations (7) and (8) as presented in the third column of Table 3. However, these values do not consider that even if it is true that the mass of oxygen is not within the battery at the beginning, it will be at the end of the discharge within the hydroxide structure. Hence, a more representative value should consider the mass or volume of the products when dividing in equations (7) and (8) these values are presented in columns 4 and 5 of Table 3. Both values had been plotted for quick comparison in Figure 3, as it can be seen the difference when the mass of the hydroxide is considered.

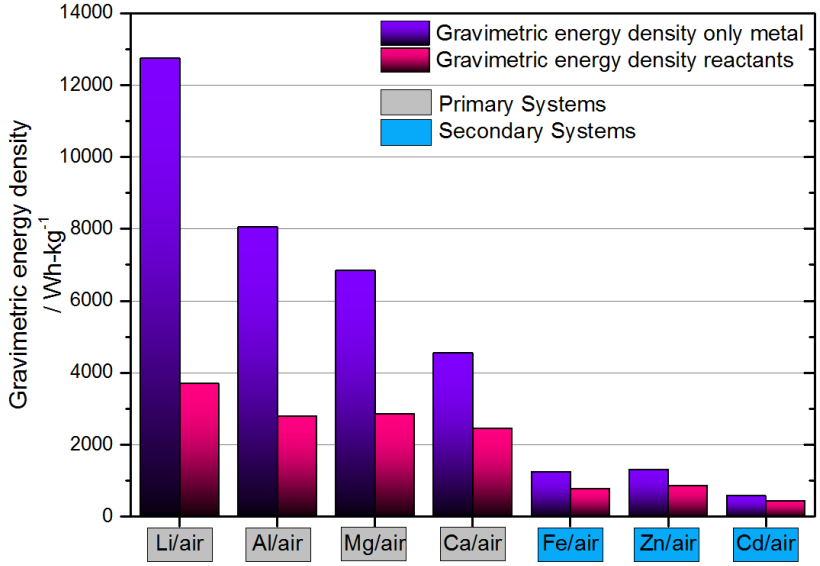


Figure 3. Metal air batteries characteristics. Theoretical gravimetric energy density considering only mass of the metal anode (in purple) and considering the mass of the hydroxides (magenta).

Mechanically rechargeable and primary MABs would require a "unifunctional air electrode" cathode optimized just for the oxygen reduction reaction. On the other hand, electrically rechargeable ones would require either a third electrode optimized for the charge or a "bifunctional air electrode" able to evolve and reduce $O_2$ during the charge and discharge respectively.

*Fe*, *Zn* and *Cd* have the advantage that can be electrically deposited in aqueous electrolyte and have low corrosion rates in alkaline media. Therefore, they could be developed as secondary systems.

The *Cd-air* system is interesting since the *Cd* anode stability had been proven in nickel-cadmium and silver-cadmium systems. A *Cd-air* battery performance had been reported with an energy density of 93 W h $kg^{-1}$ achieving 500 cycles 100% DoD and maintaining its capacity after 1 year of storage [28]. Nevertheless, it is not a very attractive battery for many applications due to the inherent toxicity of *Cd*.

*Zn* is an attractive option for the anode being one the most electropositive metals, relatively stable in aqueous alkaline solution without suffering significant corrosion

[29]. The primary *Zn-air button type battery* have proved very successful. It is known for its remarkable high energy density (300-400 Wh $kg^{-1}$ and 1.3-1.4V) for low power applications. These type of batteries had been widely used in low power portable applications mostly for telecommunications and medical applications such as hearing aid devices, cardiac telemetry monitors, railway signs, navigation aid systems, maritime buoys, telecom headsets among others [30]. The secondary *Zn-air* system still have numerous challenges related to dendrite formation inherent to the solubility and deposition of the zincate anion when cycled [26].

The *Fe-air* system despite not having the highest theoretical specific energy density among the metal-air batteries has appealing characteristics such as simple cell design, use of abundant, low costs, safe and highly recyclable materials. On the other hand, low Faradaic efficiency, passivation of the iron electrode and high over potentials at the air electrodes due to the fact that the reduction of oxygen are the main challenges in iron air batteries. These challenges have to be surpassed or diminished in order to increase the current level of performance of the this system, [2,31].

## 2.3 Electric vehicles

At the beginning of the 20$^{th}$ century, both the internal combustion engine (**ICE**) vehicles and battery electric vehicles (**BEV**) were two emerging technologies competing for the market offering better power or comfort. Since the beginning of this race electric vehicles had always been attractive for the comfort aspect especially before the starting, lighting and ignition systems for ICE vehicles was developed. BEV did not require a shifting gears system and this meant they were easier to drive. The Ford's Model T marked an important moment to impulse the use of internal combustion engine vehicles by lowering the manufacturing costs and making it widely available at the same time that gave the advantage to the ICE vehicles over BEV.

Later during this 60s together with the development of fuels cell, the idea of using them to impulse electric cars lead to the R&D of fuel cell electric car. Later on, the possibility to use the combination of both systems became an interesting research area to develop different types of hybrid electric vehicles (**HEV**) [32,33].

One of the strong points of using electric vehicles is that they do not need a gear system. Usually, the motor is below the passenger compartment and the battery system is located under the hood and the trunk. Disadvantages of BEV include insufficient driving-range, long recharge duration for which the heavy and costly-to-replace battery was blamed.

The market for electric vehicles still have some niches, like in milk deliveries services or postal services where frequent stop-start actions and quiet performance enhance the best of these systems. Another niche is for indoor vehicles such as forklift in stores where zero emissions are mandatory.

In order to advance to broader niches a breakthrough must be achieved in battery research. The United States Advanced Battery consortium USABC had analysed what would be the requirements to develop a competitive BEVs.

During the 90s, electric vehicles battery research focused largely on nickel-metal hydride batteries, developed by General Motors GM, Ovonics, SAFT, Panasonic among others. NiMH typically were able to deliver 65 W h $kg^{-1}$ with 200 W $kg^{-1}$ for 1000 cycles, this performance could lead to the development of a 160 km range in a small electric vehicle. Unfortunately, these types of batteries had a cost of 1000 USD kW $h^{-1}$, which for a 100-mile vehicle, translated into a cost over 25,000 USD per vehicle just for the battery.

The commercial development of li-ion batteries had promoted once again more research related to electric vehicles. Li-ion batteries include a variety of chemistries with specific energy densities between 140-250 W h $kg^{-1}$ and a power density of 250 - 300 W $kg^{-1}$. Nevertheless, the cost of the batteries make up for one of the most expensive components, usually the cost of the lithium-ion batteries is around 1000 USD (k W h)$^{-1}$ Li-ion is one of the best compromises between energy and power density so far, but still it should be improved in order to satisfy these goals as can be seen in Figure 4, some targets such as specific energy and most important cost are still far away from these targets.

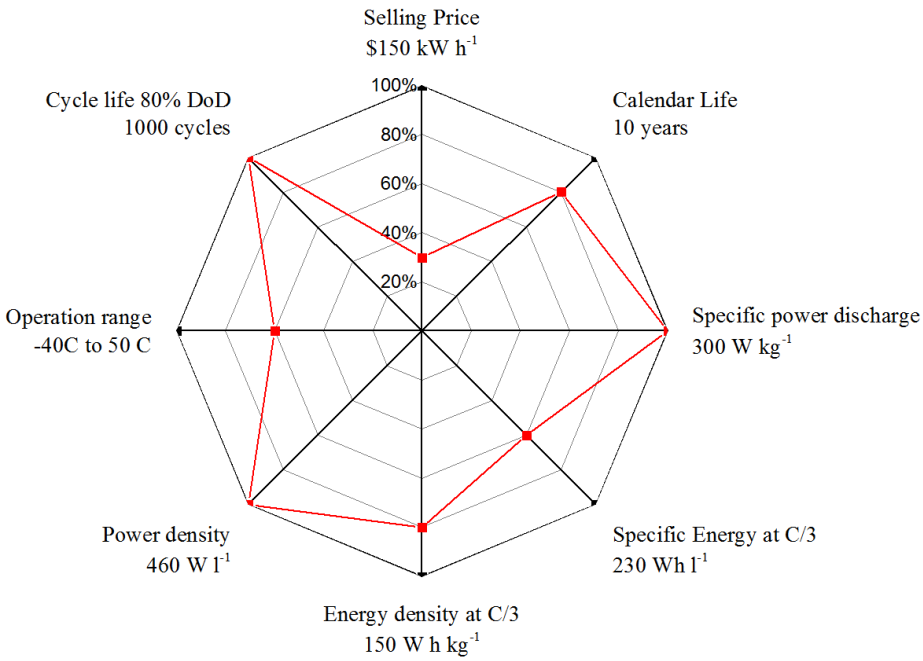


Figure 4. Status of advanced Li-ion battery development relative to the USA BC goals for EVs [34]

It has to be mentioned that these targets have done mostly in comparison to current ICE vehicles that have a considerable long driving-range before refuelling. Users living in the cities or close to main cities have pointed it out that depending on the circumstances such long ranges are actually not required most of the time. For example, the driving requirements for the case of Germany are presented in Figure 5.

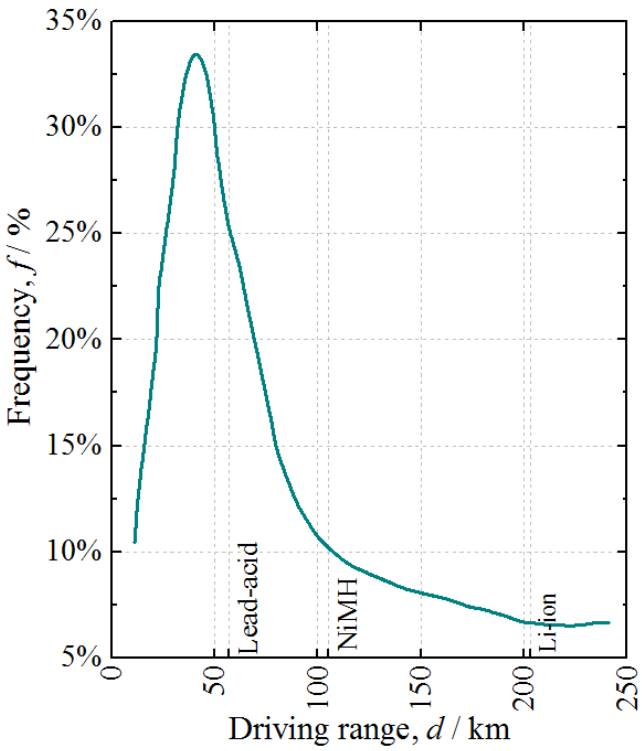


Figure 5. Relative frequency of use over daily driving-range, and battery electric vehicle (BEV) range projection for different batteries. (Data for 2003) [32].

According to Figure 5, it is observable that most of the time the driving range that is required is less than 100 km, and for seldom occasions it is required to travel longer distances, as well it is observable that with available technologies these practical driving ranges should be able to be covered by electric vehicles.

## 2.4 History of the iron air batteries.

Work specifically related to the iron-air electrochemical system did not start until middle 1960 in USA, Japan and Europe [35]. It followed in many cases previous experiences in fuel cells technology in combination with by the 70s oil crisis that impulse research on novel energy power sources.

In 1968 NASA pioneered the research of the iron-air electrochemical system and determine the feasibility to develop a 5-20 A h capacity battery with an energy density of 132 - 154 W h $kg^{-1}$, at that time NASA highlighted that the main challenges were related to water loss, self-discharge and degradation of iron oxides.

A few years later during the early 70s, Matsushita group in Japan reported the development of a 1.56 kW h iron-air module with an energy density of 88 W h $kg^{-1}$ at the C/7[6] rate and had an outgoing project to develop a 70 W h $kg^{-1}$ module able to cycle for 200 - 300 cycles by 1977. They reported the use of a sintered iron electrode and a thin carbon based air electrode in combination with a charging pole. Matsushita's cells are known to have worked for more than 800 cycles and powered a lightweight car over 200 km.

Siemens in Germany researched as well the iron-air system. They develop a 10-cell iron-air battery with a reported power and energy density of 20 W $kg^{-1}$ and 60 W h $kg^{-1}$ respectively and an overall energy efficiency of 35 % using multi-layered air-electrodes with silver as catalyst [36].

Westinghouse Electric Corporation in U.S.A was as well an active researcher of the iron-air system focusing mainly in the development of state-of-the-art sintered iron electrodes at that time. At that time it was estimated that a specific energy density of *ca* 75 W h $kg^{-1}$, and potentially 1,000 cycles of duration could be achieved [37]. Nevertheless this predicted battery module did not meet the expected lifecycle according to the final report published in 1979 due to the fast degradation of their air electrode [38].

[6] C/1 rate is the rate at which the capacity of a battery is discharged in 1 h, similarly C/7 rate is the rate at which the capacity of a battery is discharged in 7 hrs.

The iron-air battery project of the Swedish National Development Company (SNDC) was the only one that led to the development of full-scale battery tested in vehicles. With the development of a 30 kW h battery for traction applications with an energy density of 80 W h $kg^{-1}$ at the C/5 rate [35].

Early work on iron-air batteries focused on electric vehicle applications. Unfortunately, this market did not evolve as expected and further research of the iron-air system was discontinued at that time and focused instead in other metal air batteries systems such as the primary zinc-air or primary aluminium-air system.

Renewed interest has been shown in the *Fe*–air battery over last few years owing to the recent advances in nanotechnology that allows to manufacture novel high-electrochemical-surface-area, corrosion-resistant support materials that may be used to develop more robust, high efficient iron and air electrodes [2].

In recent years (Nov 2010), the University of Southern California together with the Jet propulsion lab have continued the research of iron-air batteries in 2012 with the aim of developing an iron air batter for grid-scale energy storage though an ARPA-E project [11]. The goals of the project are to start from the state of the art IAB technologies and to improve the round-trip efficiency of the system. So far a high efficiency iron electrodes had been reported by the use of different additives in the iron electrode formulation, by adding bismuth and iron sulphides into the formulations

As well in recent years Kyushu University have been an active researcher of the IAB system [39–41]. The study of novel nanomaterials to improve the performance of the iron electrode for iron air batteries is a very active area of research in this university. Some results so far are the use of novel additives and nanomaterials to further the development of iron electrodes. [39–41]

As part of this renewed interest, the NECOBAUT EU FP7 Project 2013-2015 [1] and European collaboration undertook the task to study the feasibility of an IAB for automotive propulsion by testing novel nanomaterials for electrode manufacture.

Some of the key issues related to each one of these research collaborations are briefly listed in Table 4.

Table 4. Major iron air battery developments operational parameters [2,31,42].

| **Organiza-tion/year** | **Operational parameters** | | | **Additional info** |
|---|---|---|---|---|
| | *Capacity* | *Energy density* | *Lifetime* | |
| NASA 1968 | 5-20 Ah | 132-154 W h $kg^{-1}$ | 200 cycles. | They pointed out the problems related to the self-discharge, and water lost over time. |
| Matsushita, Early 1970s [35] | 1.56 kW h | 88 W h $kg^{-1}$ | 800 cycles were achieved | Proof of concept was developed powering a lightweight vehicle for 200 km. No need for electrolyte flow systems. |
| Siemens, 1975 [36] | 50 Ah | ---- | 200-300 cycles limited by the degradation of the air electrode | They used a multi-layered air electrode using silver as catalyst. |
| Swedish National Develop. Corp., 1974-1976 [43] | 30 kW h | 80 W h $kg^{-1}$ | 1000 cycles were achieved | It was expected to reach 110 W h $kg^{-1}$ by optimizing the technology and a 44% efficiency were achieved. |
| Westing-house Electric Corp. 1970-1992 [37,38] | 40 kW h | 75 W h $kg^{-1}$ | ---- | The battery was able to deliver a 10 KW continuously with an overall weight of 530 kg. |

Because of these efforts, some preliminary prototypes were developed with practical energy densities as high as 88 W h $kg^{-1}$ during the 70s. Then during the 80s, MAB research was a minor part of most research groups since the developments focused on batteries for portable devices applications. Nevertheless, the electrode materials of these batteries have been previously studied as part of other electrochemical systems, for example the iron-electrodes have been studied as part of the nickel-iron battery (Edison battery), and as well as part of the silver-iron battery. The bi-functional air electrodes have been studied as part of fuel cells under alkaline environment as well as in other metal air battery systems such as the primary zinc-air system.

## 2.5 Iron-air battery conceptual design

At a conceptual level, the iron-air electrochemical system will rely on two main processes to deliver energy as a battery during the discharge process. The first one, the oxidation of metallic iron $Fe^0$ to $Fe^{2+}$ forming $Fe(OH)_2$ during the first plateau and later a further oxidation to $Fe^{3+}$ to form $Fe_2O_3$ respectively. Secondly, the reduction of $O_2$ taken from the air, to oxygen reduced species such as $OH^-$ within the alkaline electrolyte. The reactions involving these forms of iron oxides and hydroxides are reversible in aqueous solution, usually a strong alkaline electrolyte where the corrosion problems of metals are more manageable than in acid electrolytes [44].

The iron-air system can be engineered in two configurations:

1) The *three-electrode* configuration IAB shown in Figure 6

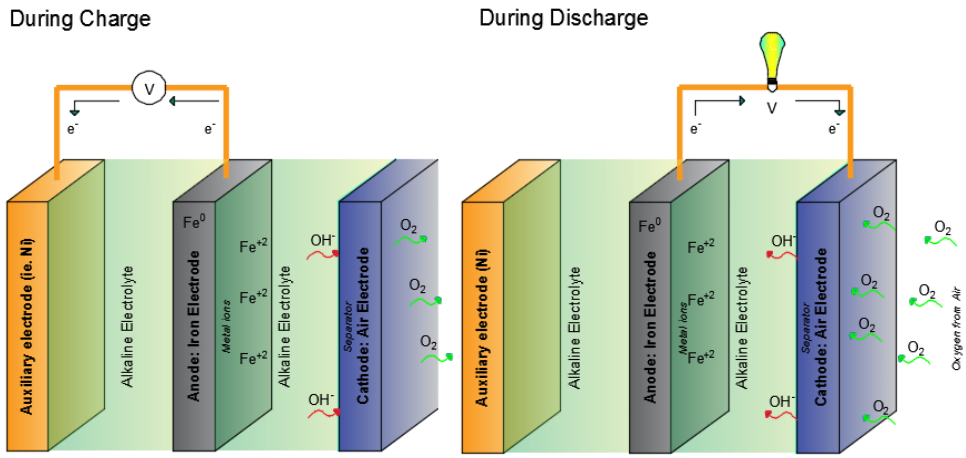


Figure 6. Three-electrode configuration of an IAB. This configuration includes an iron electrode, a gas diffusion electrode for the ORR during discharge and an auxiliary charging electrode (*i.e.* a nickel counter electrode).

The first approach implies the use of one iron electrode and two additional electrodes. One for the charging process and one gas diffusion electrode for the discharge one. This approach has the disadvantage that the third electrode will imply a greater volume and weight of the whole battery but it is attractive for systems that include a charging station where the auxiliary charging electrode can be contained outside the battery cell and only inserted when charging. This configuration has the advantage that the GDE used during discharge would only have to be optimized to catalyse the ORR overcoming the difficulties of finding a suitable bifunctional catalyst that are rare. Furthermore this configuration could allow a faster charging rate that could be limited by the performance of the GDE during charge in comparison with a Nickel electrode.

2) The *two-electrode* configuration IAB shown in Figure 7

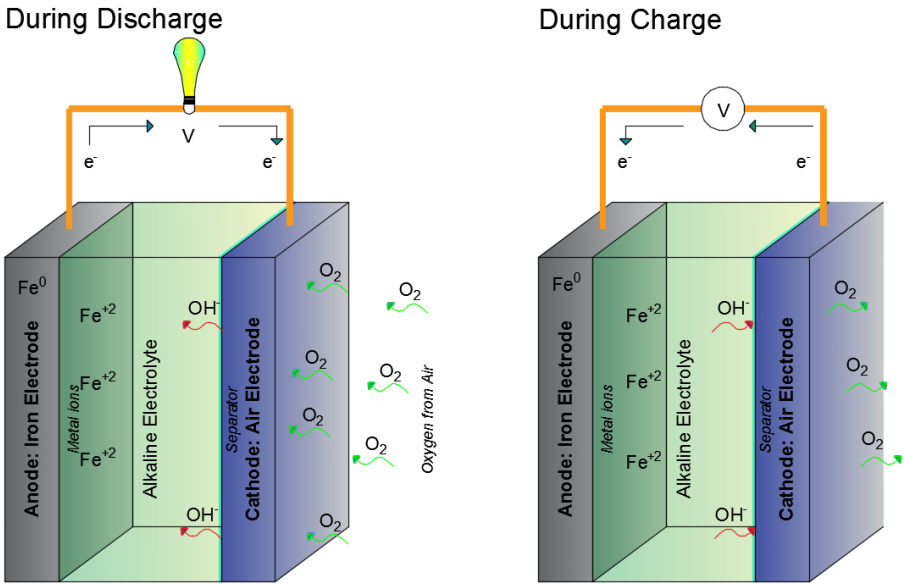


Figure 7. Two-electrode configuration of an IAB. This configuration use one iron electrode in combination with a bifunctional gas diffusion electrode that must contain a catalyst able to promote both the oxygen reduction reaction during discharge and the oxygen evolution during charge.

This configuration use a negative iron electrode in combination with one bifunctional air electrode that can work reversibly both during charge and discharge. This configuration as expected would be the ideal since a fewer number of component would lead to a greater energy density of the battery; this configuration relies on the development of novel nanomaterials suitable to work as bifunctional catalyst for both the ORR and OER for a reasonable amount of time.

## 2.6 Iron-air battery main challenges

The IAB system could be introduced as a modification of the nickel-iron battery where the nickel cathode is being replaced by a bifunctional gas diffusion electrode. The nickel iron system can be used for tractive or standalone applications with a very long life cycle up to 20 years' life with a theoretical and practical energy densities of 268 W h $kg^{-1}$ and 60 W h $kg^{-1}$, respectively. The main limitations of the nickel-iron system are low power density, poor charge retention and gas evolution on stand. The cost of this system lies between the lead acid batteries and the standard nickel/cadmium batteries [42].

The air-breathing electrode consist of a conductive support material where a bifunctional catalyst is deposited to increase the rate of both the oxygen evolution and reduction reactions. By doing this modification the resulting electrochemical system would have an increased theoretical specific energy from 268 W h $kg^{-1}$ when the nickel electrode is used to 764 W h $kg^{-1}$ with the oxygen reduction reaction and a standard equilibrium potential of 1.28 V [2].

The main challenges encountered in the past were the slow kinetics at the air breathing electrode, the relatively complex kinetics of iron reaction together with the evolution of hydrogen and self-discharge of the iron electrode that lead to low Faradaic efficiencies.

In recent years new groups have been researching the IAB system to addresses these main issues and to improve its performance, one of these groups [31] made a comparison of the state of the art of the IAB at the end of 2012 and foresaw some performance targets, these are presented in Table 5 below.

Table 5. State of the art IAB performance and suggested targets [31]

| **Parameters** | **State of the art 2013** | **Target** |
|---|---|---|
| **Voltage losses during charge at the air electrode** | **300 mV** | **150 mV** |
| **Voltage losses during discharge at the air electrode** | **200 mV** | **100 mV** |
| **Faradic charge efficiency excluding $H_2$ evolution** | **90%** | **96 %** |
| **Self-discharge per day**<br>**Efficiency lost** | **1-3%** | **0.1%** |
| **Theoretical cell voltage** | | **1.28** |
| **Overall round trip efficiency**<br>**Excluding $H_2$ evolution** | $\frac{1.28-0.3}{1.28+0.2}-3\%$<br>***ca.* 60%** | $\frac{1.28-0.15}{1.28+0.1}-0.1\%$<br>***ca.* 80%** |
| **Cycle Life** | **1000** | **2000-5000** |

The target values in Table 5 are an educated guess of how much the system can improve but these target may be achieved by addressing one by one the main challenges that hinders the performance of existing IAB systems. These are mainly the following:

- ✓ Slow kinetics of the oxygen reaction at the air electrode that require the study of suitable catalyst to improve the rate reaction over the air electrodes.
- ✓ Iron electrode self-discharge, and $H_2$ evolution during the charging process that may be address by the study of different additives in both the iron electrode and electrolyte compositions.
- ✓ Iron electrode passivation during discharge, that may be improved by combining the iron with other materials such as C or iron sulphides to improve the overall electrode conductivity.

- ✓ Life cycle of the air electrode that tends to fail due to flooding, pore blocking by carbonation or electro-oxidation of the carbon substrate that damages the support material over continuous cycling.

Some strategies to improve the performance of the iron air system includes:

- Development of high surface carbon as support material for bifunctional catalyst in air electrodes with high electrochemical surface area.
- Development of novel and low cost bifunctional catalyst for both the oxygen reduction reaction and the oxygen evolution reaction such as Pt/C, Pd/C with ultra-low loadings, or non-noble metal alternatives such as transition metal like perovskites and spinels [4].
- Studies related to the use of different additives to lower the $H_2$ evolution in iron electrodes [45].
- Studies to improve the performance of the iron electrode by using different $H_2$ inhibitors, pore formers and conductive additives [46–48].

# Chapter 3: The negative iron electrode

This chapter will present a deeper review on iron electrodes for aqueous alkaline batteries. This review will start introducing two similar electrochemical systems that makes use of iron electrodes in alkaline media, the secondary nickel-iron and the secondary silver-iron aqueous electrochemical systems. To further the description of the iron anode the reported electrochemical behaviour in alkaline media will be presented, together with the relevant electrochemical reactions. Finally the main performance challenges and suggested approaches to improve the iron electrode performance are discussed when considering the conceptual design of the iron electrode.

## 3.1 Iron electrodes in other related batteries

Negative iron electrodes have been widely studied in the past in other electrochemical systems such as the nickel-iron and the silver-iron battery. The nickel-iron secondary battery was extensively studied by Junger in Europe and Edison in the United States at the beginning of the last century [49].

The nickel-iron system is well known to be one of the most robust secondary batteries able to withstand electrical abuse such as overcharging, over discharging or short circuiting, on the other hand it suffers from a high self-discharge mostly coming from the nickel electrode, low power and energy density and similar performance as a lead acid battery but at a slightly higher cost, reason why this system is not widely used.

The secondary silver-iron system has a relatively high theoretical energy density [W h $kg^{-1}$], and can be developed with a practical energy density of 110 W h $kg^{-1}$ including other elements, it is not the most widely available battery due to the high cost of silver and in the past its applications have been reserved to those where energy density is paramount such as submarines. This system has the disadvantage that it requires a separator to avoid the silver ions reaching the iron electrode during its operation. The capacity, maximum power and shell-life is usually limited by the lifetime of the aforementioned separators that are application dependant.

The iron-air system has a high theoretical energy density of (764 Wh $kg^{-1}$)[7] due to the use a bifunctional GDE that will be discussed in the next chapter. Nevertheless all of these three electrochemical systems share similar challenges associated to the negative iron electrode in alkaline media.

## 3.2 Iron electrode behaviour in alkaline media

Iron is an attractive material for different batteries given the large number of oxidations states that it has. When iron is cycled in alkaline media (most commonly as an anode) it is possible to observe two plateaus corresponding to different oxidation states. For the first discharge plateau metallic iron $Fe^0$ oxidises to $Fe^{2+}$,

$$Fe + 2OH^- \leftrightarrow Fe(OH)_2 + 2e^- \qquad E = -0.88V\ vs\ Hg/HgO \qquad Eq.(18)$$

For the second discharge plateau $Fe^{2+}$ is further oxidized to $Fe^{3+}$,

$$3Fe(OH)_2 + 2OH^- \leftrightarrow Fe_3O_4 + 4H_2O + 2e^- \quad E = -0.76\ vs\ Hg/HgO\ Eq.(19)$$

A typical charge-discharge curve of an iron electrode in alkaline media is shown in Figure 8, the two observed plateaus corresponds to the formation of stable ions $Fe^{2+}$ and $Fe^{3+}$ in the oxidation states (II) and (III) respectively.

[7] If only the mass of the metal is considered the energy density would be 1273 W h $kg^{-1}_{Fe}$. During discharge oxygen from the air will become part of the iron hydroxides and oxides, if this mass is considered as well. Then, the theoretical energy density of the iron-air system is 764 W h $kg^{-1}$.

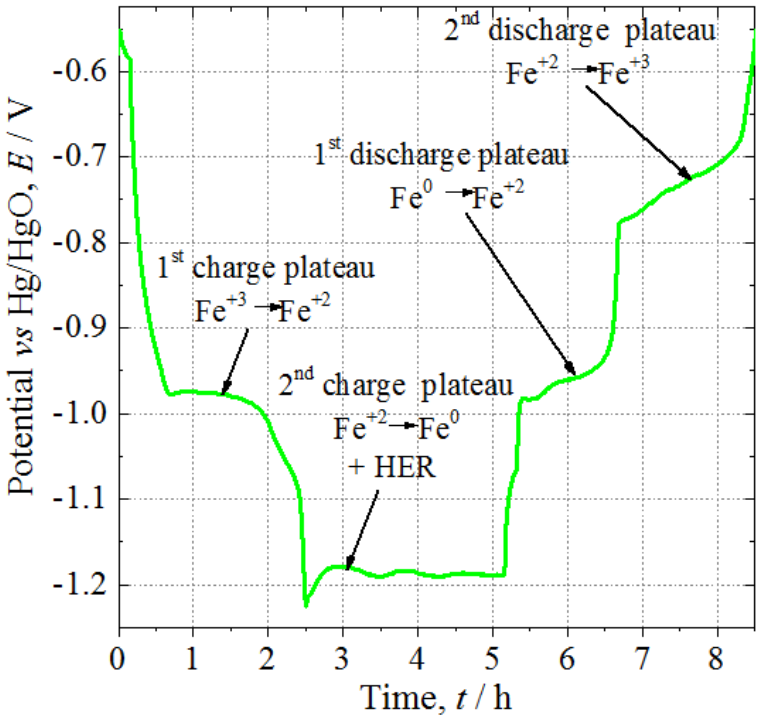


Figure 8. Typical iron electrode charge-discharge profile at the C/5 rate (254 mA $g^{-1}_{Fe}$), own data.

These plateaus are essentially the ones that correspond to the equations (18) and (19), but some authors have investigated in more detail the reaction mechanism and the structure of iron at various stages of the charge-discharge cycle [49,50]. For example according to [42] the first plateau corresponds to a more detailed mechanism given by

$$Fe + nOH^- \leftrightarrow Fe\ (OH)_n^{2-n} + 2e^- \qquad Eq.(20)$$

$$Fe\ (OH)_n^{2-n} \leftrightarrow\ Fe(OH)_2 + n(OH)^- \qquad Eq,(21)$$

In this first stage iron is dissolved as $Fe^{2+}$ species in alkaline media followed by complexation of the divalent iron with the electrolyte to form the $Fe\ (OH)_n^{2-n}$ complexes which have low solubility.

Continuing the discharge cycle is believed to form the second plateau that will lead to the formation of a mixed state between $Fe^{3+}/Fe^{2+}$ species which may interact with the $Fe^{2+}$ to form $Fe_3O_4$. (See equations (22-23))

$$Fe(OH)_2 + (OH)^- \leftrightarrow\ Fe(OH)_3 + e^- \quad Eq.(22)$$

$$3Fe(OH)_3 + Fe(OH)_2 \leftrightarrow Fe_3O_4 + 4H_2O \qquad Eq.(23)$$

The low solubility of iron intermediates and oxidized species is one of the reasons for the superior life cycling of the iron electrode; this low solubility is the reason why dendrites formation does not occur as it happens with the Zn electrode when cycling. The supersaturation of iron species on discharge results in the formation of small iron-crystallites near the reaction sites that during the charge, allows the formation of metallic iron from the hydroxides or oxides near the surface of the electrode. On the other hand this low solubility is as well the reason why these electrodes do not perform well at high current densities since the formation of these oxides at the surface of the electrode means that some of the active material will be encapsulated before reacting if it is not in intimate contact with a conductive support material.

## 3.3 The iron electrode performance challenges

As mentioned before, iron electrodes have been studied in other electrochemical systems such as, the nickel-iron battery or the iron-silver-oxide battery [42]. From these related research experiences the main identified and reported performance challenges of the iron electrode in alkaline electrolyte are: 1) the low coulombic efficiency during charge-discharge cycling, 2) the passivation of the iron electrode at high cycling rates and 3) the iron electrode self-discharge over longer periods of time.

### 3.3.1 Hydrogen evolution reaction

The low coulombic efficiency in iron electrodes is a consequence of the close proximity in the equilibrium potentials between the reduction of the ferrous ion $Fe^{2+}$ to metallic iron $Fe^0$ at -0.88 V *vs* SHE (eq. 24) and the well-known hydrogen evolution reaction (**HER**) at -0.83 vs SHE (eq. 25), the fact that the HER has a slightly less negative potential implies that reaction (eq. 25) would be occurring simultaneously during charge as a parasitic reaction.

$$2Fe + O_2 + 2H_2O \leftrightarrow 2Fe(OH)_2 \qquad E^0 = -0.88\ V\ vs\ \text{SHE} \qquad Eq.(24)$$

$$2H_2O + 2e^- \leftrightarrow H_2 + 2OH^- \qquad E^0 = -0.83\ V\ vs\ \text{SHE} \qquad Eq.(25)$$

The strategy to improve the iron electrode efficiency has been to research potential additives in both the iron electrode formulation and into the electrolyte that selectively inhibits the HER or additives that helps to separate the potentials between the HER and the iron reduction reaction, without tampering with the other reactions involved during the operation of the battery [41,51].

Some of the most successful experiments involve the addition of small amounts (*ca.* 5-10% w/w) of different sulphide additives such as $Bi_2S_3$, $K_2S$, FeS, NaS [45]. Nevertheless further studies to understand how these sulphides additives improve the performance are required since the exact mechanism is still not very well understood [45]. It was not until very recently that some insightful mechanism have been described in the iron electrodes literature [41,52,53]. According to [53] it has been identified that it is the $O^{2-}$ diffusion the rate-limiting step of the reduction-reaction of $Fe_2O_3$ under normal conditions. In the presence of sulphides, the in-situ modified $Fe_2O_3$, forms a conductive shell with excellent electrical and ionic conductivity. It has been suggested that, the amorphous FeS (shell) ages to $FeS_{0.9}$ (mackinawite) among other oxides, which introduce vacancies that can greatly enhance the $O^{2-}$ diffusion, under these conditions the surface-reaction becomes the rate-limiting step.

In a related study [41] the effects of, both bismuth oxide ($B_2O_3$) and iron (II) sulphide (FeS) were studied when used as additives in carbonyl iron electrodes. It was concluded that the presence of sulphides are required to have a steady capacity at the iron electrode and when the sulphides are depleted from the electrolyte the capacity of the iron electrodes starts to diminish (after 180 cycles) but if a sulphide source is added into the iron electrode composition the performance of the electrode does not decay even after (1200 cycles). From these result the use of small quantities of sulphide sources such as $FeS/Bi_2S_3$ would be advisable, or even taking this step further as was done in [54] where the performance of an iron-sulphide electrode was evaluated. The result was a high coulombic efficiency of 95% and a capacity of *ca.* 220 mA h $g^{-1}_{Fe.}$

Besides the use of sulphides it has been suggested that the addition of compounds containing metals known for their high over potentials towards the HER such as

metallic Hg, Pb and Bi [47] could improve the coulombic efficiency of iron electrodes, though the use of Hg is discouraged due to its inherent toxicity.

Additionally the use of a pore-former into the iron electrode formulation can lead to an improvement of its performance by allowing the electrolyte to permeate intimately the active material during its operation. For this purpose 5-10 % w/w of a sacrificial material is added into the composition of the electrode such as potassium carbonate in hot-pressed iron electrodes or ammonium bicarbonate in sintered carbonyl iron electrodes, in both cases the sacrificial material is displaced from the electrode structure leaving behind cavities that increase the overall porosity of the electrode.

The impact of the porosity has been reported in detail in [55]. As it has been mentioned the density variation between the charged and discharged phases implies a considerable change in volume that may lead to the entrapment of active material that cannot be reached to react during the cycling of the electrode. For this reason the use of a sacrificial material is suggested to deliberately create pores within the electrode structure and in general the results indicated an increment in the discharge capacity of sintered iron electrodes in the measure that the porosity increased. According to a model the optimum would be when the porosity that makes up exactly for the volume change between the charge and discharged phases but experimentally an additional 24% porosity was required to achieve values close to 962 mA h $g^{-1}{}_{Fe}$.

### 3.3.2 Hydrogen evolution over the iron electrode and the role of sulphides in the electrolyte

As mentioned before, the equilibrium potential of the hydrogen-evolution-reaction and the charging reaction from iron hydroxide to iron in alkaline media are very close as is shown in equation (24) and equation (25). Furthermore, the $H_2$ evolution under standard conditions is slightly less negative this means that during charge this reaction should be observed before the iron-hydroxide reduction reaction, this implies that during charge some of the electrons will be used to evolved hydrogen instead of charging the iron electrode, lowering the coulombic efficiency. Usually between 30-45% of the applied charge is wasted via $H_2$ evolution [40].

There are mainly three approaches to reduce $H_2$ evolution over iron electrodes. The first one is the use of additives in the iron electrode formulation that will raise up the over potential for the electron-transfer step involved in the $H_2$ evolution reaction. The second one is the use of additives within the electrolyte that form adsorbed layers at the iron electrode/electrolyte interface that block the active sites for the electron transfer. The third one is the use of ultrapure iron such as carbonyl iron that has very little impurities that may favour $H_2$ evolution reaction.

It is known that the hydrogen evolution potential will vary depending on the metal used as a catalyst. This means that when using different metal-electrodes the potential at which the hydrogen evolution reaction starts will be different, with lead, mercury and bismuth having the highest over potentials.

Bismuth is usually the preferred choice for safety reasons. It has been suggested that the addition of bismuth, bismuth oxide, or bismuth sulphide in the iron electrode formulation could reduce the $H_2$ evolution, since $Bi^{3+}$ ions can deposit as metallic bismuth over which the hydrogen evolution occurs at a more negative potential making $H_2$ evolution harder to occur. Using this approach in combination with carbonyl iron, very high coulombic efficiencies over 90% had been reported [41]. This is an example of how adding small amount of additives into the iron electrode formulation (5-10 wt. %) can increase its coulombic efficiency.

The second approach is the use of sulphide additives in the electrolyte rather than in the electrode formulation. The role of sulphides have been studied in detail by Narayanan in [41]. In this work, a hot-pressed carbonyl iron electrode with small amounts (5%) of bismuth sulphide was studied, this electrode had a rated capacity of 300 mA h $g^{-1}$ and a charging efficiency of 96%. Then after continuous cycling the capacity faded away after 150 cycles to 50% of its rated capacity, but it was recovered by the addition of sodium sulphide into the electrolyte (2mM). It is believed that the sulphide ion in the electrolyte plays an important role in the performance of the iron electrode.

It has been suggested by [41] that when bismuth sulphide ($Bi_2S_3$) is added into the iron electrode formulation, $Bi_2S_3$ will reduce and deposit metallic bismuth on the iron electrode whilst releasing sulphide ions ($S^{2-}$) into the electrolyte according to eq. (26)

$$Bi_2S_3 + 6e^- \leftrightarrow 2Bi + 3S^{2-} \qquad Eq.(26)$$

Then it is believed that the sulphide ions within the electrolyte will combine with the iron (II) hydroxide (27), and will form FeS which according to [53] will give the iron electrode an enhanced electric and ionic conductivity.

$$Fe(OH)_2 + S^{2-} \leftrightarrow FeS + 2OH^- \qquad Eq.(27)$$

Nevertheless, these ions have the tendency to be oxidized at the positive electrode to sulphates and will deplete overtime implying that a continuous supply of sulphides would be required to maintain the performance.

In a second experiment using a carbonyl iron containing (10%) bismuth oxide and (5%) iron sulphide it was possible to achieve capacity of 250 mA h $g^{-1}$, but in this case, unlike the previous one, the discharge capacity remained unaltered even after 1200 cycles with a 92% charging efficiency. The main difference is that the iron sulphide is insoluble unlike the sodium sulphide used in the first experiment. (This result was achieved when charged at the C/2 rate and discharged at the C/20 rate).

In a recent publication [48], different additives such as bismuth, bismuth sulphide, iron sulphide, were added into the carbonyl iron electrode formulation the conclusion was that bismuth sulphide and iron sulphide were the most promising additives to diminish the $H_2$ evolution and enhance the iron electrode performance, in this experiment when no additive was used a very low utilization of electroactive material at the C/5 rate < 5% was achieved and when used in combination with these additives it increased up to 20% and 35% for the iron sulphide and bismuth sulphide respectively, bismuth by itself did not help to improve the performance of the iron electrode, this may indicate that the amount of added bismuth is not enough to increase the overall over-potential of the HPIE for the HER, and that the effect due to the presence of sulphides is the dominant one when improving the performance of HPIE.

The use of sulphides to improve the iron electrode performance is a recurring topic, but lately the use of organosulfur molecules have been mentioned as well as potential additives to reduce $H_2$ evolution. In a recent study [40], the reduction in the $H_2$-evolution-current caused by various organomolecules with different structural motifs (linear and cyclic thiols, dithiols, thioethers and aromatic thiols)

were reported. The results reported $H_2$-evolution-current reductions between 50% and 95% when small concentrations of these additives were included in the electrolyte composition (2mM concentrations). The best case reported was for the 1-dodecanetiol. An unexpected advantage of using these additives to reduce $H_2$ evolution was that unlike soluble sulphides such as sodium and potassium sulphides [41,45] the organomolecules do not get electro-oxidized at the positive electrode. In these experiments the carbonyl iron electrodes were charged at C/2 rate and discharged at the C/20 rate, when no additives were used the charging efficiency was 65% and when additives were used the efficiency improved up to 90%, the electrodes were charged to its rated capacity of 275 mA h $g^{-1}$ (28% of the theoretical 960 mA h $g^{-1}$).

### 3.3.3 Passivation of the iron electrode

Metallic iron has a good electrical conductivity (*ca.* 10 M S $m^{-1}$), unlike its discharged products $Fe(OH)_2$, FeOOH which increase the ohmic losses and create an insulating layer that prevents the electrolyte from reaching the iron active material contained within the electrode core when discharged at high C rates (>1C).

Both the iron hydroxides and oxides formed during discharge occurs at a solid state, this is both an advantage and a disadvantage. On one hand this is the reason why in this system there is no need to worry about dendrite formation due to the re-platting of dissolved species; but on the other hand, is the reason behind the passivation of the iron electrode.

To address the passivation of the iron electrodes it is necessary to modify the electrode-electrolyte interface as well as improving the electronic and ionic conductivity at the surface where the iron electrode reactions occurs. At a higher scale (µm) it is important to ensure that the iron electrode is porous enough to ensure an intimate contact with the electrolyte, furthermore due to the differences in molar volume between the charged and discharged state a 73% porosity is required to allow enough space for the iron to become iron hydroxide [56].

The suggested strategy to surpass this problem has been to mix the iron active material with a high electrochemical-surface-area (ESA) and good conductivity support material such as carbon black in various proportions. This mix can be

accompanied by other processes such as ball milling to ensure a more intimate mixing or can be done as part of the nano-structuring synthesis process of the active material.

Besides the use of additives, and the combination of the iron active material with nanostructured carbon, it is worth mentioning that iron under different conditions can create different types of iron oxides. The different types of iron oxides are an interesting area of research since their electrical, optical, magnetic and electrochemical properties are very dependant of the type and size of nanostructure they develop during its operation.

One property that can vary drastically and that is very important to determine the performance of the iron electrode is the electrical conductivity of the discharge products. It has been mentioned in the past that if iron electrodes are discharged at very high discharge rates they may produce FeOOH with certain structure that have a reduced electrical conductivity (*ca.* $10^9$ Ω cm) responsible of the passivation of the iron electrode [57].

### 3.3.4 Iron electrode self-discharge and corrosion

The final challenge related to the iron electrode is the self-discharge over longer periods, this self-discharge is a consequence of iron corrosion reaction. To explain this in Figure 9, the Pourbaix diagram for iron has been included, in this diagram it is possible to observe which species of Fe are in equilibrium at a particular p.H. and potential, for the case of the IAB the electrolyte is usually a very strong alkaline solution, (6M KOH), which correspond to a p.H. close to 14. In this region, it is observable that Fe will transform directly into $Fe(OH)_2$ over time depending on the potential, according to the reaction presented in eq. (28). Without any measures this may cause a loss of 1-2% per day [31].

$$Fe + 2H_2O \rightarrow Fe(OH)_2 + H_2 \qquad Eq.(28)$$

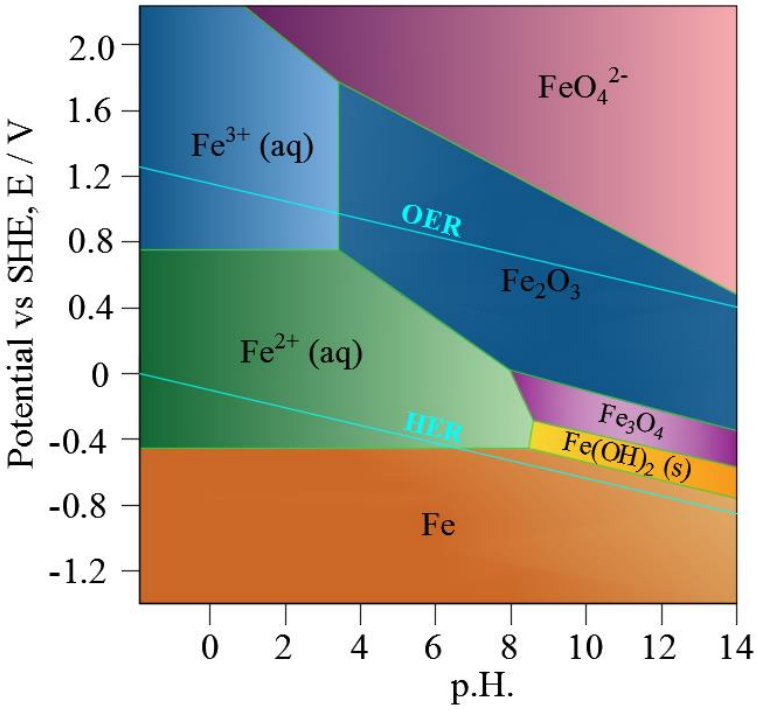


Figure 9. Pourbaix diagrams for iron-water systems at 298K, based on data from [58].

It has been reported that the presence of small amounts of bismuth oxide may help to reduce the HER but that it provides as well the additional benefit of diminishing the losses due to the self-discharge of the iron electrode [47]. It has been suggested that the following reaction takes places in the presence of bismuth oxide.

$$Bi_2O_3 + 3H_2O + 3Fe \rightarrow 2Bi + 3Fe(OH)_2 \qquad Eq.(29)$$

The potential of equation (29) is more positive than the potential of the reduction from iron hydroxide to iron, therefore during the charge the electro-reduction of bismuth and iron will occurs simultaneously which may increase the $H_2$ over-potential.

## 3.4 Iron electrode porosity considerations

An important macroscopic design consideration of iron electrodes is the fact that there is a considerable volume change during the iron electrodes operation, especially during the first discharge plateau corresponding to the oxidation of Fe to $Fe^{2+}$.

When comparing the density of Fe, $Fe(OH)_2$ and $Fe_3O_4$, from reactions (18) and (19) it is appreciable that 1 mol of Fe will react to 1 mol of $Fe(OH)_2$ which later will produce 0.33 of $Fe_3O_4$, taking this into account the expected volume and volume changes are outlined in table 6.

Table 6. Volume change during discharge. ($V_o$ volume of 1 mol of Fe)

| | ***Involved Moles*** | ***Molar Mass / g mol$^{-1}$*** | ***Mass / g*** | ***Density / g cm$^{-3}$*** | ***Volume / cm$^3$*** | ***$V_f/V_o$ %*** | ***Vol change %*** |
|---|---|---|---|---|---|---|---|
| ***Fe*** | 1 | 56 | 56 | 7.87 | 7.12 | 100% | 0% |
| ***$Fe(OH)_2$*** | 1 | 90 | 90 | 3.4 | 26.47 | 373% | 272% |
| ***$Fe_3O_4$*** | 0.33 | 160 | 53.33 | 5.24 | 10.18 | 143% | 43% |

It is appreciable that there will be a 373% volume increase when going for metallic iron to the formation of iron hydroxide according to equation (18), so it is important to make the iron electrode porous enough in order to avoid the cavities getting blocked which may prevent the electrolyte from reaching the iron electrode active material contained within.

In order to avoid losing material that may detach from the iron electrode main structure during continuous charge-discharge cycling the active material could be contained within a metallic plate or metallic mesh that works as well as the electrode connection.

Alternatively, sintering the iron electrode is a way to ensure the mechanical integrity of the iron electrode but it would be expected that any nano-structuring processing of the iron material may be lost during the sintering process. The sintering process consist in compacting the active material (usually a powder with a binder) followed with a thermal process that is lower than the melting point of the mixture. During this phase some of the nanostructures of the material could be lost mostly due to the thermal treatment.

## 3.5 Different types of iron active materials

Following these techniques there are various papers reporting the performance of different materials containing iron to be used in aqueous alkaline iron based batteries such as: carbonyl iron, iron III oxide, iron (II, III) oxide and iron sulphide.

*Carbonyl Iron (Fe):* Carbonyl iron is produced by the chemical decomposition of purified pentacarbonyl and have been highlighted as a good candidate to develop iron electrodes, the main reason is that is has been claimed that this type of iron has very few impurities (0.5% for grade R) which sometimes favours the HER during charge such as nickel and manganese that have a lower over potential towards the HER with respect to iron. Using carbonyl iron in hot-pressed electrodes, specific capacities of 275 mA h $g^{-1}$ at C/5 discharge rate have been reported in several occasions by Narayanan [41,46,47,55].

*Iron II, III oxide ($Fe_3O_4$):* The electrochemical characterisation of magnetite in combination with different carbon nanostructures have been reported, [59] the synthesis and performances of nano-$Fe_3O_4$ supported on carbon nanofibers with capacities of 786 mA h $g^{-1}$ and 75% coulombic efficiency at the $30^{th}$ cycle with a $V_{cut\ off}$ = -0.1 V *vs.* Hg/HgO. Similarly in a more recent article high performing $Fe_3O_4$ polyhedrons reached a capacity of 604 mA h $g^{-1}$ at 120 mA $g^{-1}$ and a charging efficiency of 83.9%.

*Iron III oxide ($Fe_2O_3$):* the electrochemical properties of $Fe_2O_3$/C nanoparticles deposited over carbon (to improve its limited conductivity) have been reported with capacities as high as 875 mA h $g^{-1}$ during the first cycles and even after 50 cycles the capacity was still *ca.* 575 mA h $g^{-1}$, part of the success to increase the capacity of $Fe_2O_3$ have been the improvement of the iron distribution over the surface of different carbon nanostructures. [60–62].

*Iron sulphide FeS*: In general by nanostructuring the iron electrode in combination with high surface area carbon structures it is possible to improve both the conductivity and to obtain iron electrodes with higher capacities than those that only use iron mixed with carbon materials. Nevertheless it is important to study both types of techniques to address up to what point the extra manufacturing cost and improvement in performance is feasible when compared with simpler

manufacturing processes and materials. Following this approach simple composite FeS/C can be synthesised by simpler routes and have been tested to manufacture iron electrodes with capacities of 325 mA h $g^{-1}_{Fe}$ at 300 mA $g^{-1}$.

It was noticed that during the experiments cycling iron electrodes with sulphides, the sulphides that are present in the electrolyte diminish with time, most certainly these sulphides must react at the surface of the counter electrode reason why its concentration tends to diminish over time.

Since there are many reported iron electrodes that have been tested in slightly different conditions such as discharge rates or using different cut off potentials, sometimes the mass of the electrode is not reported, or sometimes is not clear if the energy density is reported by mass of electrode or mass of iron, for this reasons it was suggested to try out different iron materials under the same conditions and determine which one would be better in hot pressed iron electrodes.

## 3.6 Strategies to improve the iron electrode performance

In this section various different approaches based on the literature review associated to the performance of iron electrodes as anodes in alkaline media is presented.

- Improve conductivity: Mix iron active material with high surface carbon material: Nano-structuring the Fe/C material using different carbon nanostructures will ensure both a high surface area and good conductivity of the overall electrode ensuring a good distribution of the iron active material.
- Control the porosity: Ensure that the overall iron electrode is porous enough to allow easy access of the electrolyte within all its structure. This can be done by the addition of a sacrificial material that will dissolve in the electrolyte such as potassium carbonate. An increased porosity will help to reach all the active material during its operation which will help to improve the utilization of the iron active material, besides this pore structures are required to manage the expected volume change of the iron active material when cycling.

- Use of metal meshes and foams: Pack the Fe/C active material within a conductive material that helps to give the overall electrode mechanical stability and works as well as the current collector the use of metal foams, metal meshes are ideal for this purpose.
- Sulphides additives in the electrode and/or electrolyte composition: Modify the electrode-electrolyte interface using additives within the iron electrode composition to diminish the passivation of the iron electrodes when cycling at high current density. These additives include iron sulphide and bismuth sulphide for the electrode and lithium hydroxide, sodium sulphide, octane thiol, alkane thiols, in the electrolyte.
- Improve the manufacturing of the iron electrodes by ball milling the active materials or develop novel techniques to mix the iron active material with carbon as part of the synthesis process.
- Use of different iron active materials and characterise its use at different current densities such as magnetite, maghemite, hematite, goethite, carbonyl iron, iron sulphide and to compare its performance among themselves.
- Sintering the iron material to ensure a better mechanical integrity of the electrode (this technique might not be advisable in combination with nano-structuring the iron material since any nano-structuring may be lost during this process)

## 3.7 Iron electrode conceptual design

As it has been mentioned in this chapter one of the most important challenges to further the development of the IAB is the development of an optimised iron electrode capable to deliver high capacity with a reasonable high round trip coulombic efficiency. Conceptually this could be achieved including various design elements in the iron electrode structure, these are described here and schematically presented in Figure 10, do bear in mind that the actual electrode is not that regular.

a) A conductive and high surface area support material such as carbon black that would increase the overall conductivity of the iron electrode, especially of the iron oxides formed during the discharge.

b) A suitable binder material such as PTFE able to confer the electrode mechanically integrity.

c) The chosen iron active material, there are many options reported in the literature including carbonyl iron, iron sulphide (FeS), goethite (FeOOH), magnetite ($Fe_3O_4$), hematite ($Fe_2O_3$).

d) Additives to reduce the hydrogen evolution reaction during charge and additives to mitigate the iron electrode self-discharge.

e) A pore former that will dissolve in the electrolyte to increase the inherent porosity of the iron electrode, managing the micro and meso porous structure of the electrode could be a strategy to improve its performance and mechanical integrity whilst improving the utilization of the iron active material.

f) Current collector that may help as well to keep the integrity of the electrode such as stainless steel meshes or metallic foams.

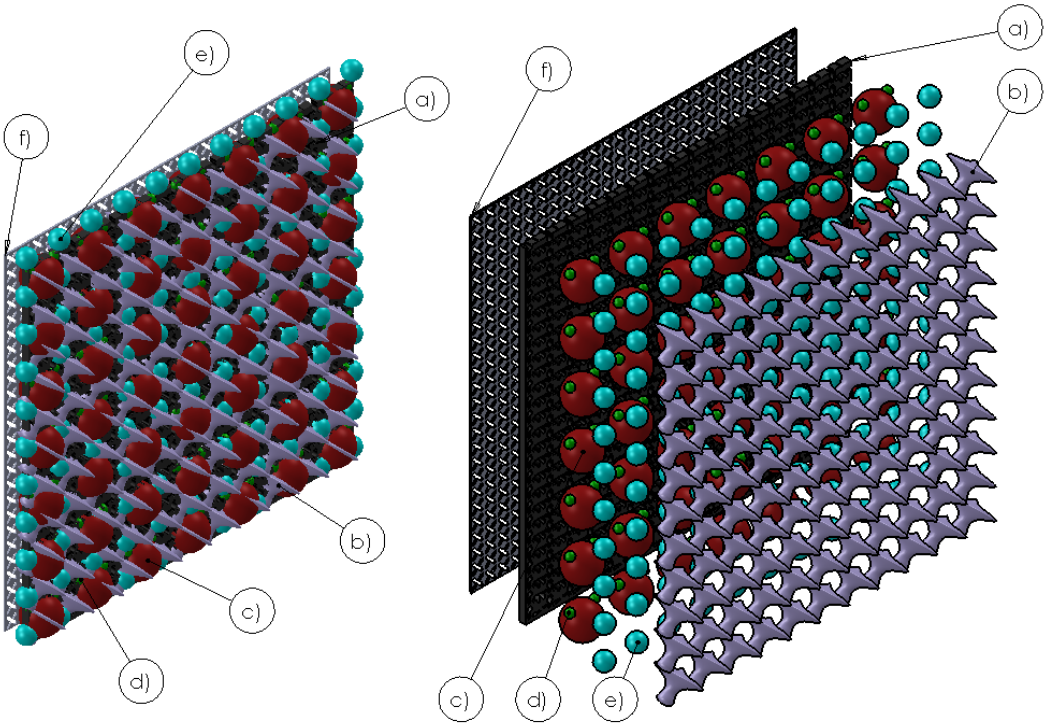


Figure 10. Iron electrode conceptual design. a) High surface area support material (*e.g.* Ketjenblack), b) Binder (*e.g.* PTFE), c) Iron active material (*e.g.* $Fe_2O_3$, $Fe_3O_4$, FeOOH, Carbonyl iron, FeS), d) Additives to diminish HER (*e.g.* $Bi_2O_3$, $Bi_2S_3$, FeS) e) Pore former (*e.g.* $K_2CO_3$) f) Current collector (*e.g.* stainless steel mesh and metal foams).

# Chapter 4: The positive air electrode

This chapter focuses on the positive gas diffusion electrode (**GDE**), addressing what the main design challenges associated to this IAB component are and which the strategies to improve its performance are. The development of a high performing GDE depends in great measure of the performance of the chosen bifunctional catalyst to promote the oxygen reactions. For this reason in this chapter a literature review on the main bifunctional catalysts have been included. Finally, the main design factors affecting the performance of GDE together with the potential strategies to improve its performance are discussed.

One of the most challenging features of MABs is the design and manufacture of the bifunctional GDE where both the oxygen reduction reaction (**ORR**) and the oxygen evolution reaction (**OER**) occurs. The challenge itself resides in the fact that it is over this structure where a three-phase interface (solid-liquid-gas) is tailored to allow the oxygen in the air to reach the catalysts whist promoting both electron and ionic conductivities with both the electrolyte and the current collector, respectively.

## 4.1 The oxygen reduction reaction (ORR) electro-catalysts

During the discharge cycle, oxygen-reduction will take place at the air electrode. The kinetics and mechanism of this reaction have been extensively studied [26]. The strong interest to develop low-temperature fuel cells during the 60s and 70s lead to the development and characterisation of different nanomaterials as catalyst to promote the reaction rate and to lower the high over potentials for the ORR. Simultaneously a deeper understanding of the mechanism of reaction under different conditions and in the presence of a vast number of catalyst have been previously reported [63–67].

The kinetics of ORR depends on various factors such as type of cathode material, electrolyte and temperature but in general terms there are two overall pathways for this reaction, the direct 4-electron and the 2-electron pathways that occurs

differently in alkaline and acid media. Given that most MABs are only compatible in alkaline electrolyte, only this case will be mentioned.

The direct 4-electron pathway is favoured by platinum, platinum family metals, platinum alloys, silver, gold-100 in alkaline solution, metallic iron in neutral solutions, and some metal oxides such as perovskites and pyrochlores [68]. On the other hand the 2-electron peroxide pathway is favoured on: graphite and most other carbons, oxide covered metals such as Ni or Co and some transition metal macrocycles. It has been reported that mercury, carbon, oxide covered metals and most transition metal oxides favours the peroxide pathway as well [69].

The direct 4-electron pathway in alkaline media is

$$O_2 + 2H_2O + 4e^- \longrightarrow 4OH^- \qquad E^0 = 0.401\ V\ vs. SHE \qquad Eq.(30)$$

The 2-electron or peroxide pathway in alkaline media occurs in two possible ways, each one involving two steps, the first one,

$$O_2 + H_2O + 2e^- \longrightarrow HO_2{}^- + OH^- \qquad E^0 = -0.065\ V\ vs\ SHE \qquad Eq.(31)$$

Followed by

$$HO_2{}^- + H_2O + 2e^- \longrightarrow 3OH^- \qquad E^0 = 0.867\ V\ vs\ SHE \qquad Eq.(32)$$

Or either decomposition of peroxide

$$2HO_2{}^- \longrightarrow 2OH^- + O_2 \qquad Eq.(33)$$

The direct 4-electron pathway involves a number of intermediate steps that reduce to $OH^-$ and/or water. These intermediate steps may require an adsorbed peroxide intermediate that does not get into the solution this is a key observation to distinguish both pathways, since in the 2-electron pathway peroxide should be detectable in the solution that may result in $O_2$ that is recycled in the process described by equation (30).

In order to detect the presence of peroxide being formed during the oxidation it is possible to use a rotating ring disk electrode. Broadly, it consist of a conductive disk surrounded by a conductive ring separated by an isolating material. These type of electrodes can rotate to ensure that a laminar flow is being formed. Once

hydrodynamic steady conditions are meet, it is possible to perform either a potentiostatic or a galvanostatic protocol on both the rotating disk, and/or the rotating ring. Usually a potential to promote the ORR is applied to the rotating disk, and a protocol to reduce and detect the associated presence of the $2HO^{2-}$ radical associated to the peroxide path according to eq. (33), is applied on the ring.

A vast number of proposed reaction mechanism has been suggested by both experimental observations and theoretical analysis. Just to exemplify a couple of them, in Figure 11 the model suggested by Damjanovic *et al* [70], and the model of (Bagotskii *et al.* 1969) for the ORR in aqueous electrolytes are presented, these two models are similar both of them start with $O_2$ in bulk solution, that migrates to the vicinity of the electrode surface where it reacts to form an adsorbed peroxide $H_2O_2$ on the surface of the electrode, from where it may detach and become $H_2O_2$ in the bulk solution or where it may be further reduced to $H_2O$, furthermore there exist the possibility of some of the $O_2$ in the surface of the electrode to be spontaneously reduced directly to $H_20$. The main difference between these two mechanisms is that the latter one consider that the adsorbed $H_2O_2$ may oxidise back to $O_2$. How fast these reactions occur is reflected on the values of $k_1$, $k_2$, $k_3$ and $k_{-2}$.

$$\begin{array}{c} O_{2,b} \longrightarrow O_{2,*} \xrightarrow[k2]{} H_2O_{2,a} \xrightarrow[k3]{} H_2O \\ \downarrow \\ H_2O_{2,b} \end{array} \qquad \begin{array}{c} O_{2,b} \longrightarrow O_{2,*} \underset{k-2}{\overset{k2}{\leftrightarrows}} H_2O_{2,a} \xrightarrow[k3]{} H_2O \\ \downarrow \\ H_2O_{2,b} \end{array}$$

Figure 11. Example models for the ORR. On the left model suggested by Damjanovic *et al.* [70], on the right model proposed by Bagotskii *et al.* [26]. Subscript "a" means adsorbed on electrode surface, "b" means in bulk solution, "∗" means in the vicinity of electrode surface.

It is important to mention that in many occasions various models are able to interpret the same experimental data, and that various oxygen reduction pathways may be possible depending on the specific conditions. Furthermore, specific mechanism have been described over the surface of specific electrode materials, for example,

Over graphite, Morcos *et al.* reported the following mechanism [71]:

$$O_2 \rightarrow O_2\ (ads) \qquad Eq.(34)$$

$$O_2(ads) + e^- \rightarrow O_2^{\cdot -}(ads) \qquad Eq.(35)$$

$$2O_2^{\cdot -}(ads) + H_2O \rightarrow O_2 + HO_2^- + OH^- \qquad Eq.(36)$$

$O_2^{\cdot -}$ is the superoxide radical ion. For the previous mechanism, the second reaction (35) has been reported as the rate-determining step.

In a similar way, there are specific mechanisms over other electrode surfaces such as carbon black [72], glassy carbon and perovskites involving various oxygen containing species which are out of the scope of this research.

## 4.2 The oxygen evolution reaction (OER) electro-catalysts

Noble metals such as Pt, Au, Ir, Rh can be used as electro-catalyst for the OER, during the process an oxide layer of the originally oxide free metal will be formed as a bi-product. Metal oxides such as $RuO_2$, $IrO_2$, NiO, perovskites are usually better electro-catalyst for oxygen evolution than the bulk metals by themselves.

Ruthenium oxide unlike other metal oxides has a metallic alike conductivity (2 x $10^4$ to 3 x $10^4$ $\Omega$ $cm^{-1}$) making it an interesting option in an electrode specialized for oxygen evolution. Besides, it has a good corrosion resistance in acid media and a slow corrosion rate in alkaline electrolyte. Ruthenium metal is as well a good electro-catalyst but it suffers strong corrosion.

Nickel and its alloys show a good electrocatalytic activity for the OER and are relatively inexpensive in comparison to ruthenium or iridium oxides. Nickel oxyhydroxide β-NiOOH is usually the preferred electro-catalyst for oxygen evolution on nickel anodes, but it is important to keep the potential lower than 1.8 V since this may induce the transformation of $Ni^{3+}$ to $Ni^{+4}$ that forms an oxide with lower conductivity and lower electro catalytic activity.

Other metal oxides have as well good oxygen evolution electro catalytic properties just a few are stable at the anodic potentials at which the OER is observed. Some transition metal oxides have shown very good results such as the spinel $NiCo_2O_4$.

The detailed mechanism of reaction for the OER depends on many factors including the electrode substrate, the catalyst and the potential at what the reactions occurs. Besides if all the possible intermediates states are considered the amount of possible pathways is vast, nevertheless it is agreed that the rate-determining step is the discharge of $H_2O$ in acid or the discharge of $OH^-$ in alkaline electrolytes [26].

$$(H_2O)_{ads} \longrightarrow (OH)_{ads} + H^+ + e^- \quad Eq.(37)$$

Followed by a fast-intermediate reaction, either (38) or (39)

$$(OH)_{ads} + (OH)_{ads} \longrightarrow (O)_{ads} + H_2O \quad Eq.(38)$$

Or

$$(OH)_{ads} \longrightarrow (O)_{ads} + H^+ + e^- \quad Eq.(39)$$

Before the final evolution reaction step (40)

$$(O)_{ads} + (O)_{ads} \longrightarrow (O_2)_{ads} \quad Eq.(40)$$

And final detach from the surface into the bulk solution (41)

$$(O_2)_{ads} \longrightarrow O_2 \quad Eq.(41)$$

For example [73] a detailed study on the mechanisms over perovskites such as nickelates, cobaltates, ferrites, manganites and suggest a pathway that lead to the intermediate formation of $H_2O_2$ where the rate determining step is given by breaking of the surface-OH bond, an alternative mechanism have been suggested by [74] where the rate determining step was dependent on the electrode surface-OH bond strength.

## 4.3 The bifunctional catalyst

Another challenge for the development of MAB is related to the slow kinetics of both oxygen reactions. In order for these reactions to occur at a reasonable rate for a battery a suitable catalyst layer must be used [13]. In this sense the election of a specific bifunctional catalyst is crucial to develop a high performing GDE for rechargeable MAB. Ideally the chosen bifunctional catalyst should be electrochemically stable over a fairly wide window to include both the ORR and

the OER potentials which typically occurs at *ca.* -0.65 V and 0.65 V *vs* Hg/HgO respectively.

In order to measure and compare the catalytic activity of a bifunctional catalyst, it is usual to perform a cyclic voltammetry where the voltage is varied within a potential window and to measure the resulting current which is proportional to the rate of reaction under study, this approach is similar to the one reported by [5,6] .

The general experimental set up for this type of experiments is a half-cell configuration using a Pt mesh counter electrode, delimiting a suitable potential window to observe both the OER and the ORR, in this case from [-0.65, 0.65] *vs* Hg/HgO, supplying either $O_2$ or air at the back of the GDE at a known rate (*i.e.* 100 ml $min^{-1}$) and to set up a slow scan rate (*i.e.* 1 mV $s^{-1}$) after having performed some initial scan rates usually at faster scan rates (*i.e.* 10-50 mV $s^{-1}$) to clean the surface of the working electrode. For the aqueous IAB the electrolyte is highly concentrated KOH (*i.e.* KOH 6 M), the reference electrode for alkaline media is Hg/HgO as schematically shown in Figure 12.

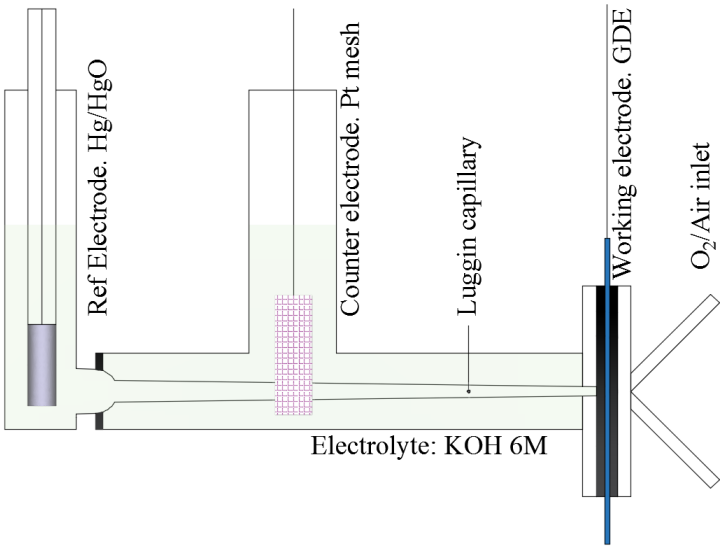


Figure 12. Schematics to compare the performance of various bifunctional catalyst in GDE.

With this experimental set up it is possible to compare the performance of various GDE obtaining in each case a plot such as the one presented in Figure 13, where the comparison of 3 bifunctional GDE is presented. Two of these bifunctional catalyst contain Pd catalyst with different loadings, and the case with no loading. From this experiment is possible to conclude that the best performing electrode was

the one with the highest loading of Pd corresponding to the dark green line. It is appreciable that the magnitude of the current density at each extreme is higher than the current densities achieved by the other catalyst formulations at a given potential, which implies a faster reaction rate.

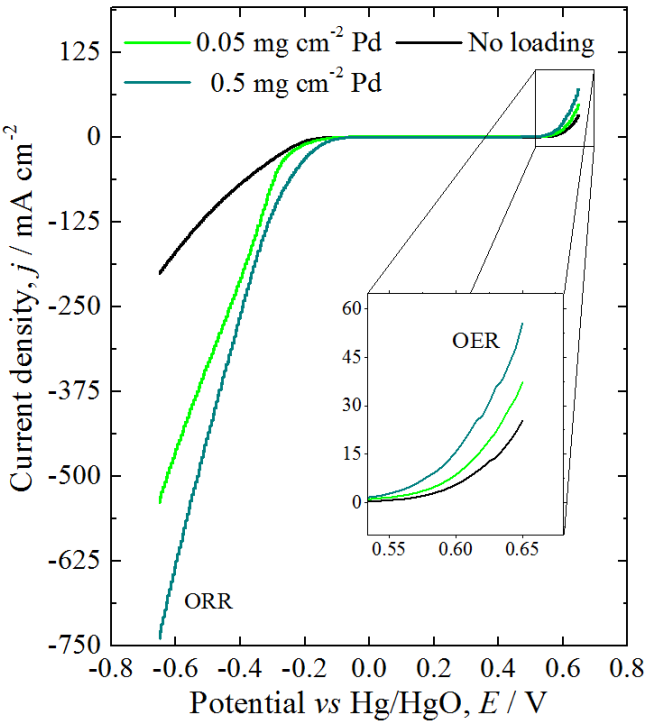


Figure 13. Typical cyclic voltammograms of a gas diffusion electrodes with different loadings of the Pd/C bifunctional catalysts. The left arm corresponds to the ORR while the extreme right to the OER. Adapted from [6].

It would be desirable to use only one single bifunctional catalyst in the GDE in practice this is not possible since good and long lasting bifunctional catalyst are rare and usually involve the use of noble metals such as Pt and Pd that must be used sparingly or in combination with other more widely available alternatives such as perovskites [75] or spinels [67,76,77].

The synthesis and electrochemical characterisation of novel catalyst is an active area of research. As part of the NECOBAUT collaboration a bi-functional air electrode using very small loadings of palladium was developed and the detailed characterisation can be found in [4], in general there were promising results since the performance of this type of GDE showed a better performance for the ORR in comparison with some commercially available GDE such as the Pt/C GDE manufactured by Gasketel. This was noticed when comparing the charge-discharge

profiles with both electrodes and observing that the potential for the Pd/C in-house GDE was E = 0.01 V *vs*. Hg/HgO, which was 60 mV higher that the Gasketel commercial electrode; furthermore a more consistent performance was observed over various cycles. For this reason, for this project it was suggested to follow a similar methodology to produce GDE, but in this case using a mixture of the Pd/C catalyst with Ni-Fe HCF to improve the performance of the existing in-house air electrodes [5]. In Figure 14 a compendium showing various cycling voltammetries corresponding to different bifunctional catalyst reported in the literature is presented.

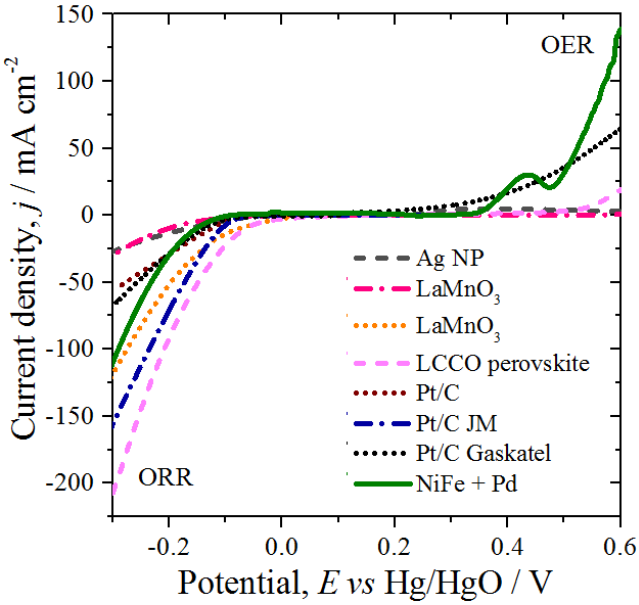


Figure 14. Cyclic voltammetry comparison between seven reported bifunctional catalyst and the in-house Pd (0.5 mg $cm^{-2}$) + Ni-Fe HCF (5 mg $cm^{-2}$) GDE, adapted from [5].

It is appreciable that LCCO perovskite (pink dashed line) is the one with the less negative onset potential for the ORR but on the other hand its activity for the OER is very low, it would be interesting in the future to combine LCCO perovskite with the Ni-Fe HCF which is the one that improves the OER electro catalytic activity which was one of the reasons why later LSFCO perovskite was studied in chapter 5.

## 4.4 Factors affecting gas diffusion electrode performance

There are several aspects that may affect the operation lifetime of the GDE. These includes: carbonation, catalyst dissolution, carbon corrosion, mechanical failure and leaking [26].

*Carbonation.* The presence of $CO_2$ in the air that may react with the electrolyte leading to the neutralisation of the alkaline electrolyte and precipitation of carbonate that may block the pores in the air electrode limiting its performance over time, reason why the use of an oxygen permeable membrane has been suggested to increase the lifetimes of GDE [78–80].

*Corrosion of support material*. The oxygen intermediate species evolved during the charge may attack the substrate, alter the activity of the catalyst or eliminate the wet-proofing film. Research to develop and test new support materials that can overcome these problems is widespread, for example, carbon nanomaterials (carbon cloth, carbon paper, carbon nanotubes) are produced and tested as support material.

*Mechanical failure and leaking*. If the support material is corroded this may lead to further structural damage. Usually the air electrode will also work as a barrier that holds the electrolyte inside the cell. At the edges, it should be able to withstand the pressure of the required O-rings to avoid electrolyte leakage. This seal may break if the air electrode is not structurally strong enough. In some instances, carbon particles can dislodge during charge and reach the iron electrode, where they contribute to a decrease in its porosity and subsequent capacity decline [38].

*Dissolution of catalyst*. Some catalyst material may dissolve over time, for example, Ag is a good electro catalyst for the ORR in alkaline media but will slowly dissolve over time however it may be acceptable in air electrodes for at least 1000 h at 50 mA $cm^{-2}$ rate at room temperature in primary cells. Another example is Pd that has as well a good electro catalyst performance and according to Thacker, it may dissolve as well over time. This dissolution will be observed as gradual decrease in the ORR rate during discharge [81].

## 4.5 Bifunctional gas diffusion electrode conceptual design

Summing up, the required elements in the GDE are described below and presented in the corresponding diagram in Figure 15 :

g) Oxygen permeable membrane: a porous membrane that only allows the transport of oxygen of the air and do not allow $CO_2$ to reach the electrolyte since this may form carbonates and may block the gas diffusion layer and lower the life cycle of the air electrode.

h) Gas diffusion layer: this structure should be porous enough to allow the oxygen to meet with the catalyst, and the electrolyte during the ORR.

i) Current collector: usually a metal mesh or metal foam to improve the overall conductivity of the air electrode and reduce the ohmic losses. This layer is usually the one that will allow the electrical connections of the cell.

j) Catalyst support material: a high-electrochemical-surface-area material is used for this layer such as carbon nano-powder or carbon nanotubes that will be mixed with the catalyst for the OER and ORR or the bifunctional catalyst.

k) The bifunctional catalyst: this is the most important aspect of the air electrode because it allows the ORR to happen at a fast-enough rate to be used in a battery. The traditional ones are usually noble metals (Pt, Pd, Ir, IrO) or non-noble metals alternatives such as $MnO_2$, transition metal oxides such as spinels, and perovskites.

l) The hydrophobic binder material: this material should allow the catalyst layer to have a sufficient mechanical integrity over the lifetime of the battery. The binder usually provides the hydrophobic property to the side of the air electrode that is in contact with the electrolyte and should be sufficient in order to avoid leakage though the air electrode.

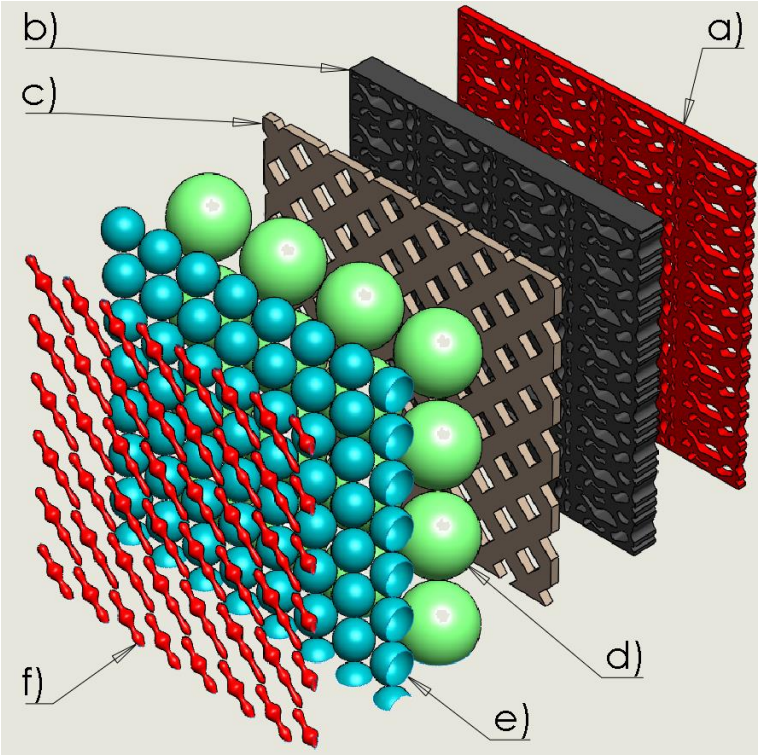


Figure 15. Air-electrode conceptual design. a) oxygen permeable membrane, b) gas diffusion layer, c) current collector, d) catalyst support material, e) bifunctional catalyst, f) hydrophobic binder material.

The three-phase layer have to be set up when manufacturing the air electrodes. A way to achieve this is by carefully using a hydrophobic layer on the airside and a hydrophilic layer on the electrolyte side. The balance between these two layers is of crucial importance to develop a long-life air electrode that would not allow the electrolyte to leak over the lifetime of the battery.

Other important aspect to consider is the porosity of the material. Micro and meso-porous structures can ensure favourable mass transport properties of the air electrode but must still give the mechanical rigidity needed to support the mechanical stress that the O-rings or gaskets may put upon the GDE during the assembly of the battery [44]. In order to study the porous structure of the electrode, computing tomography imaging can be a very useful technique to gain insight of the pore sizes, tortuosity and other geometrical parameters within the air electrode [82,83].

Summarizing the main challenges to develop high performing GDE for an alkaline IAB are:

1. To achieve the right balance between hydrophobicity and hydrophilicity to create a suitable 3 phase interface where the ions in the electrolyte can interact with the catalyst layer and is porous enough to allow the diffusion of oxygen without leaking and ensuring a reasonable lifetime for the battery whilst supplying a suitable high surface corrosion resistant conductive material.
2. To find a cost effective bifunctional electro catalyst by optimizing the loading and by developing efficient manufacturing techniques to disperse the catalyst layer over the high surface support material.
3. To optimize the micro and mesoporous structure of the GDE to ensure a suitable oxygen diffusion and reduce the possibility of blockage by carbonation.
4. Give the overall GDE enough mechanical strength and a suitable frame to avoid leaks over when assembled with the rest of the cell components.

Some of the suggested strategies to develop high performance GDE includes:

1. To use ultra-low loadings (0.5 - 5 mg $cm^{-2}$) of electro-catalyst and to disperse it over high surface materials to optimize its performance and make this component cost-effective.
2. To research the possibility to reuse or recycle the various components of the air electrode components.
3. Use X-ray tomography to study the meso and micro porous structure of GDE to determine parameters that allow us to study and ensure optimum $O_2$ transport within the GDE structure.

# Chapter 5: Iron electrode experiments and results

In this chapter the experimental procedures to manufacture hot pressed iron electrodes (**HPIE**) is outlined, together with the electrochemical characterisation of various iron formulations aiming to determine how to improve and optimise the iron electrode charge-discharge capacity[8]. There has been many reported strategies to improve the iron electrode performance as was described in chapter 3, which were followed to set up a series of experiments to compare how the iron electrode would behave under various scenarios. In this chapter the results of these experiments are presented.

## 5.1 Experiments performed on the iron electrode

Various formulations were tested in order to study the electrochemical performance of HPIE for the aqueous IAB, here below they are concisely listed and described:

1. ***Optimisation of hematite ($Fe_2O_3$) to carbon ratio***: After comparing the performance of various iron active materials, it was noticed that hematite dispersed on high surface carbon black ($Fe_2O_3$/KB) have a superior discharge capacity, so further experiments included varying the proportion of hematite to carbon.
2. ***Discharge capacity comparison of two synthesis methods for $Fe_2O_3$/C electrodes.*** This work was done in collaboration with our Italian collaborators who synthetized this material that shown higher discharge capacities.
3. ***Comparison of different iron active materials in hot-pressed iron electrodes***. This type of experiments included preparing and electrochemically testing various formulations using different iron materials reported in the literature. These active materials included: carbonyl iron, hematite, goethite, magnetite and iron sulphide. This set of experiments is intended to be submitted as a publication in the following months.

[8] The term charge-discharge cycle in this chapter refers to the fact that the iron electrode would be in principle paired in an iron air battery where it would be the anode, strictly speaking in a half cell configuration these correspond to a reduction-oxidation cycle.

4. ***Effects of ball milling on the performance of HPIE***. The same active materials that were mentioned in the previous paragraph were ball milled before manufacturing the HPIE, the observed effects of ball milling on the discharge capacity performance are discussed.
5. ***Influence of potassium carbonate as a pore former in the discharge capacity of hematite iron electrodes:*** this set of experiments aimed to determine if there was an observable difference in the discharge capacity of hematite iron electrodes when a pore former was added into the electrode formulation.

## 5.2 Preparation of hot pressed iron electrodes (HPIE)

For the following experiments different types of iron electrodes were produced by preparing an iron active paste (depending on the case it is a mixture of an iron active material, mixed or nanostructured with carbon, with 5% w/w potassium carbonate as pore former; and *ca.* 4% of bismuth sulphide) mixed together with 10% w/w PTFE, and hot pressed at 140 °C and 625 kPa between two stainless steel meshes for 10 minutes (MTI hydraulic hot press).

The iron active materials and different commercially available materials used to prepare the HPIE are listed and described below:

- $Fe_2O_3$/C synthetized by Adam method

This material was prepared by a molten-salt fusion method [84,85] where the iron precursor $FeCl_2$, was dispersed in iso-propanol under magnetic stirring followed by addition of the necessary amount of $NaNO_3$. The mixture was left to evaporate for several hours and the resulting powder was calcined in air at 500 ºC for 1 h. The fused salt-oxide obtained after calcination in air was washed with distilled water to remove the remaining salts, filtered and dried in an oven at 80 °C for 12 h. The iron oxide so obtained was then mixed in the ball-milling apparatus for 4 h with 3 different proportions of carbon amount of carbon (Table 7, Ketjenblack, from Azkonobel) in the presence of ethanol to favour the mixing of the solid ingredients. In order to suppress hydrogen evolution (a competing reaction with reduction/oxidation of the iron species), 4 wt. % $Bi_2S_3$ was added as well to the $Fe_2O_3$-C composite formulation during ball milling.

- $Fe_2O_3$/C synthetized by the oxalate method

Additionally $Fe_2O_3$/C was synthetized by an organic colloidal preparation that consisted in the formation of colloidal particles by the use of oxalic acid (oxalate method). The iron precursor, iron nitrate, is dissolved in a solution containing the oxalic acid at pH ≈ 6.5 and at 80 °C. Subsequently $H_2O_2$ is added to decompose the complex and form a precipitate that is collected by filtration, dried and subsequently calcined in air at 600 °C for 1 h in a ventilated furnace to obtain $Fe_2O_3$. This iron oxide is subsequently blended in a planetary mill with Ketjenblack and $Bi_2S_3$ in the desired proportions (shown in

Table 7) for 4 h at 100 rpm in the presence of ethanol.

Table 7. Synthesis details for iron electrodes formulations.

| ***Label*** | ***Synthesis*** | ***$Fe_2O_3$*** | ***Ketjenblack*** | ***$Bi_2S_3$*** |
|---|---|---|---|---|
| Adams -1 | Adams 500 | 49.5% | 46.5% | 4.0% |
| Adams -2 | Adams 500 | 71.0% | 25.0% | 4.0% |
| Adams -3 | Adams 500 | 85.5% | 10.5% | 4.0% |
| Oxalate | Oxalate 600 | 49.5% | 46.5% | 4.0% |

- Iron(II,III) oxide >97% Sigma Aldrich
- Iron(III) oxide >97% Sigma Aldrich
- Iron oxy-hydroxide Sigma Aldrich
- Carbonyl iron powder >99% Sigma Aldrich
- Iron (II) Sulfide Technical grade Sigma Aldrich.
- PTFE 60 wt % solution Sigma Aldrich
- 1-Octanethiol Sigma Aldrich (>98.5%)
- Stainless steel fine mesh: The Mesh Company, #500 mesh, 0.026mm aperture, 0.025 mm wire diameter, SS316 grade.
- Stainless steel medium mesh: The Mesh Company, #200 mesh, 0.077mm aperture, 0.05 mm wire diameter, SS316 grade.
- Stainless steel wide mesh: The Mesh Company, #40 mesh, 0.41mm aperture, 0.22 mm wire diameter, SS316 grade.

## 5.3 Iron electrode half-cell prototype

The iron electrodes were tested in a three-electrode 3D printed cell using a nickel plate counter electrode, and a Hg/HgO (1M KOH) reference electrode, in an aqueous 6 M KOH solution, as shown in Figure 16, overall cell dimensions 36 mm x 57 mm x 8 mm, exposed electrode area 25 mm x 40 mm, the inter electrode gap was *ca* 2 mm.

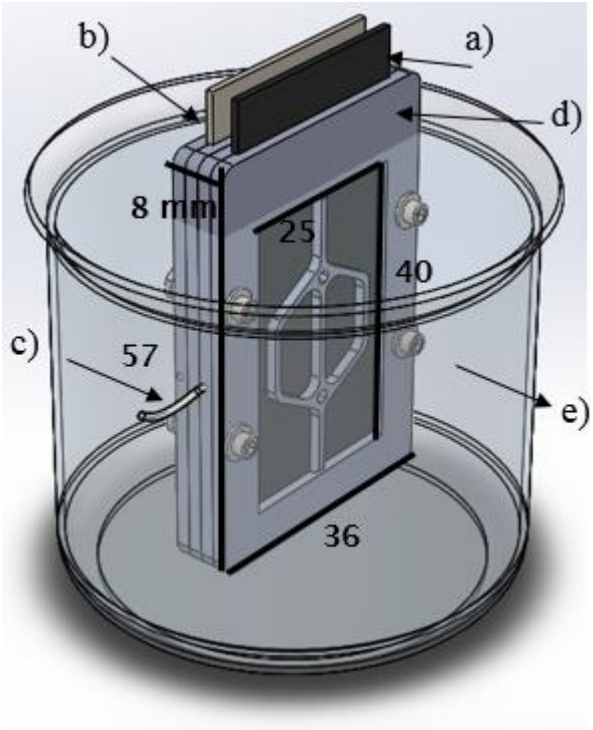


Figure 16. Experimental cell arrangement. a) Hot-pressed iron working electrode, b) Nickel plate counter electrode, c) Luggin capillary connected to Hg/HgO reference electrode, d) ABS 3D printed electrodes support. Interelectrode gap: 2 mm, e) Electrolyte: 6M KOH solution.

## 5.4 Effect of Fe/C ratio on the capacity of $Fe_2O_3$/C HPIE

The principal aim of the following set of experiments was to compare the performance of iron III oxide (hematite) with carbon black when mixed in different proportions. There are three different iron/carbon ratios: 0.7, 2 and 5.7, which correspond to 45%, 64% and 78% of Fe in the formulation. The details of each

formulation can be found in Table 8, and the details of the synthesis of these active materials have been described in the previous section.

Table 8. Formulations ICR1-ICR3 to test different iron to carbon ratios.

| | ***Active Material*** | | ***Formula / mg*** | ***Fe act. material %*** | ***C*** | ***$Bi_2S_3$*** | ***PTFE*** |
|---|---|---|---|---|---|---|---|
| ICR1 | Iron (III) oxide / C | $Fe_2O_3$/C | 271 | 45% | 42% | 4% | 9% |
| ICR2 | Iron (III) oxide / C | $Fe_2O_3$/C | 188 | 64% | 23% | 4% | 9% |
| ICR3 | Iron (III) oxide / C | $Fe_2O_3$/C | 155 | 78% | 10% | 4% | 9% |

Each hot-pressed electrode was Galvano-statically cycled for at least 20 charge-discharge cycles at the C/5 rate (considering the capacity up to the second plateau C = 1273 mA h $gr^{-1}_{Fe}$) with an Ivium n-stat potentiostat by overlaying the charge-discharge curves the outcome of this experiment can be presented as in Figure 17. Similar curves were obtained for the remaining ICR2 and ICR3 electrodes, and from this plots it is possible to plot the discharge capacity in each cycle, and distinguish the delivered capacity up to the first plateau ($E_{cut\ off}$ = -0.75 V *vs* Hg/HgO.) and up to the end of the second plateau $E_{cut\ off}$ = -0.55 V *vs* Hg/HgO.

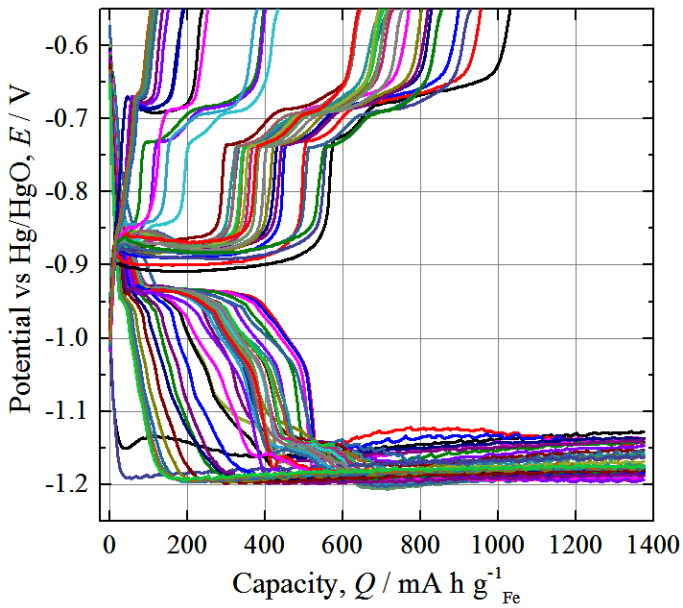


Figure 17. Charge-discharge profiles at the C/5 rate for electrode ICR1.

In Figure 18, the respective discharge capacity histograms for electrodes ICR1, ICR 2 and ICR 3, to obtain these histograms the accumulated capacity in [mAh $g^{-1}_{Fe}$] was obtained from cero to the desired cut off potential. In blue, the accumulated

discharge of the first discharge plateau (capacity up to $E_{cut\ off}$ = -0.75 V *vs* Hg/HgO) is depicted and in purple, the capacity associated to the second plateau up to $E_{cut\ off}$ = -0.55 V *vs* Hg/HgO. The total capacity can be read as the value correspondent to the top of the stacked bars (*i.e.* for the 3$^{th}$ cycle of electrode ICR1, the contributions from the 1$^{st}$ and 2$^{nd}$ plateaux are *ca.* 500 m A g$^{-1}_{Fe}$, and 410 m A g$^{-1}_{Fe}$ respectively, so the total discharge capacity adds up to *ca.* 65.).

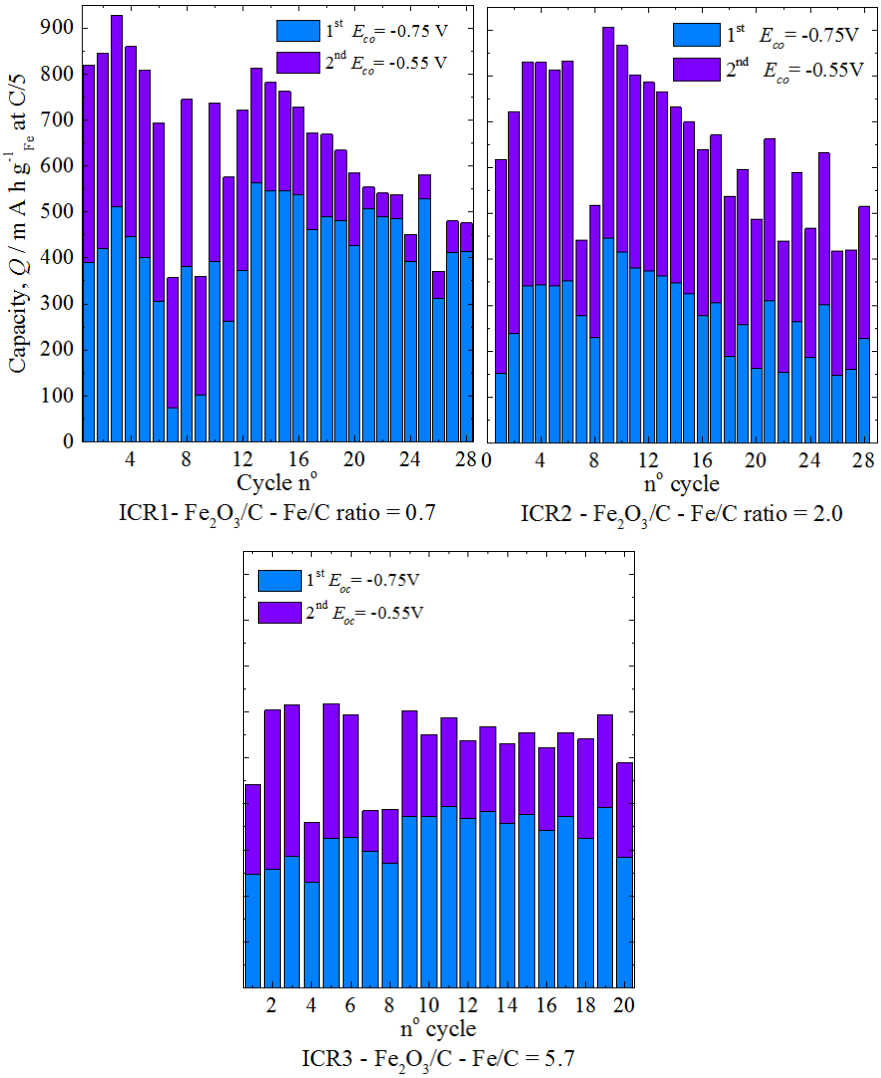


Figure 18. Discharge capacity of electrodes ICR1, ICR2 and ICR3. These formulations only differ in the proportion of iron to carbon being 0.7, 2.0 and 5.7 respectively.

The corresponding descriptive statistics, (mean, min, max, std, dev) for the accumulated capacity for both plateaux, for each one of the three electrodes ICR1, ICR2 and ICR3 were determined and are presented in Figure 19. From these statistics it is appreciable that, the maximum discharge capacity per gram of iron was achieved with ICR1 (915 mA g$^{-1}_{Fe}$), corresponding to the formulation with the

highest amount of carbon, but the highest mean discharge capacity (**MDC**) was achieved by ICR2 (650 m A h $g^{-1}_{Fe}$) corresponding to the formulation with a ratio of iron to carbon of 2.0. Overall, the MDC values would represent better the performance of the iron electrodes than the maximum value achieved.

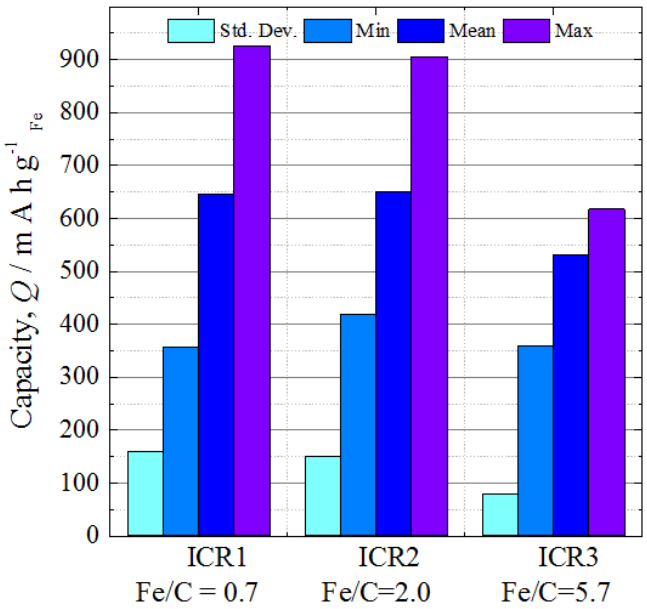


Figure 19. Discharge capacity of hot pressed $Fe_2O_3$/C electrodes at the C/5 rate (mA $g^{-1}$ Fe). Left: Fe/C = 0.7 Center: Fe/C 2.0 Rigth: Fe/C = 5.7

The MDC of ICR1 and ICR2 are very similar (*ca.* 650 mA h $g^{-1}_{Fe}$), under these conditions ICR2 would be a more attractive formulation since is rendering similar results than a formulation with a larger amount of carbon black leading to a less voluminous formulation. On the other hand, when comparing these results with ICR3 and its MDC of 525 mA h $g^{-1}_{Fe}$ it is observable that if not enough carbon is added to the formulation, its performance is compromised. This could be either due to the limited electrical conductivity of the discharge products or due to a significantly smaller surface area to disperse the iron active material in comparison with ICR1 and ICR2.

## 5.5 Effect of synthesis method of $Fe_2O_3$/C on the discharge performance of HPIE

Besides comparing the influence of the iron to carbon ratio, a set of experiments were carried out in parallel to compare $Fe_2O_3$ dispersed over Ketjenblack by the 2

different synthesis methods:SM1 (Is the same ICR1 electrode from the previous section) prepared by the Adams method, and electrode SM2 prepared by the oxalate method (see details in Table 9) . Note that the proportion of iron to carbon in this set of experiments was held at 0.7 ensuring a high electrical conductivity.

Table 9. Formulations ICR1-ICR3 to test the electrochemical performance of hematite synthetized by the oxalate and the Adams methods.

| | ***Active Material*** | | ***Act. mat mass / mg*** | ***C black / mg*** | ***$Bi_2S_3$ / mg*** | ***PTFE / mg*** | ***% of Iron in Active Material*** | ***Fe*** | ***Fe/C*** | ***Fe/$Bi_2S_3$*** |
|---|---|---|---|---|---|---|---|---|---|---|
| SM1/ ICR1 | Iron (III) oxide / C | $Fe_2O_3$/C | 246 | 114 | 10 | 25 | 35% | 85 | 0.7 | 9 |
| SM2 | Iron (III) oxide / C | $Fe_2O_3$/C | 246 | 114 | 10 | 25 | 35% | 85 | 0.7 | 9 |

After continuous galvanostatic charge-discharge at the C/5 rate (255 mA $g^{-1}_{Fe}$), the corresponding discharge capacity with a cut off voltage of $E_{oc}$ = -0.55 V *vs* Hg/HgO is presented in Figure 20, for both cases.

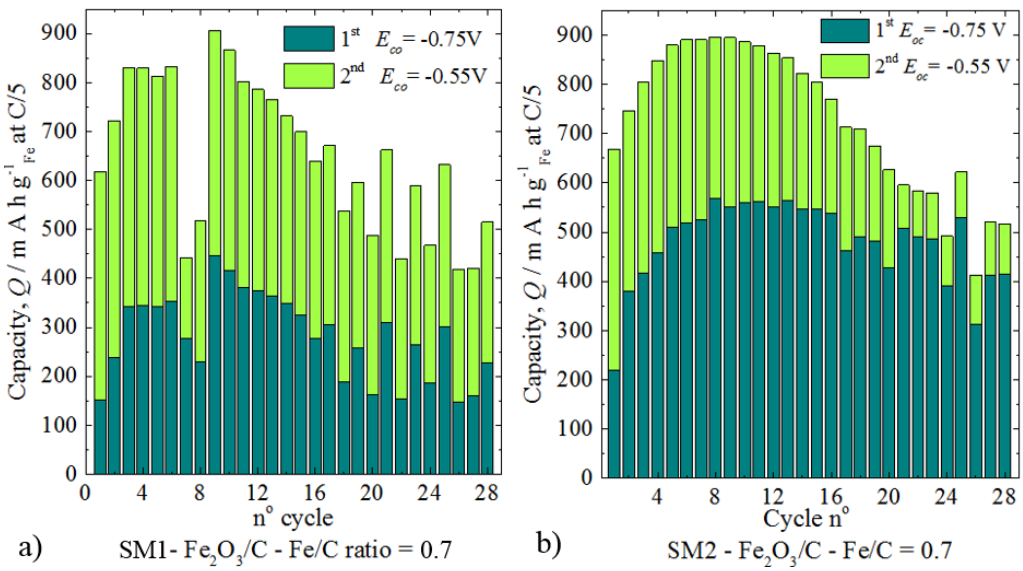


Figure 20. Discharge capacity of $Fe_2O_3$/C electrodes at the C/5 rate (255 mA $g^{-1}_{Fe}$) synthetized by: a) SM1-Adams method b) SM2-Oxalate method

When comparing the histograms presented in Figure 20 it is observable that the performance of both SM1 and SM2 reached similar discharge capacity values, but there is a much larger variation from cycle to cycle observed in SM1, *i.e.* from the $7^{th}$ to the $8^{th}$ cycle there is variation as high as 400 mA h $g^{-1}_{Fe}$, this difference could

be related to a sudden release in the $H_2$ bubbles that were observed during the charging process or to a strong passivation of the electrode during those cycles.

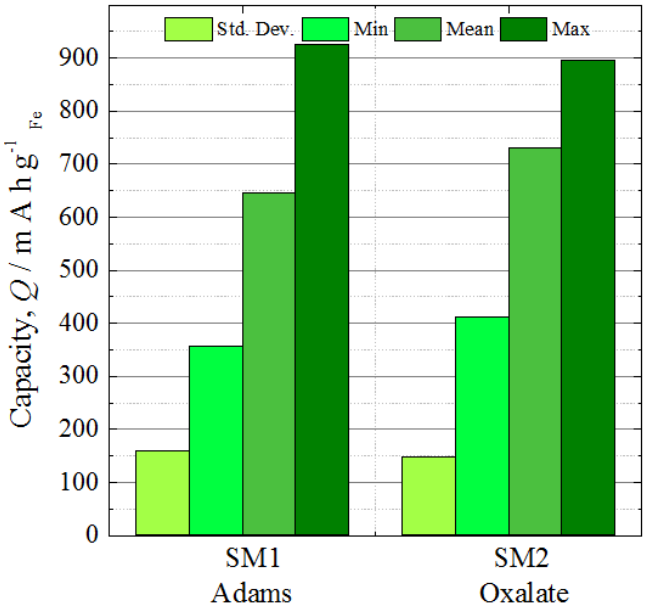


Figure 21. Descriptive statistics of the discharge capacity at the C/5 rate of electrodes E1, and E4: Left: Adams at 500°C Rigth: Oxalate method (*n.b.* Fe/C = 0.7)

The behaviour described in the previous discussion with electrodes SM1, SM2 is confirmed by their descriptive statistics (Figure 21). The mean discharge capacity of SM1 and SM2, are 650 mA h $g^{-1}_{Fe}$ and 725 mA h $g^{-1}_{Fe}$. Although the MDC is higher for SM2 the absolute maximum was achieved by SM1 with almost 915 m A h $g^{-1}_{Fe}$, followed very closely by electrode SM2 with 900 mA h $g^{-1}_{Fe}$. From the previous discussion it may seem that formulations prepared by the Adams and the oxalate method have very similar performances being the later one marginally better.

## 5.6 Effect of ball milling on different iron active material formulations

The objective of the following experiments was to compare various commercially available iron active materials, and to determine if by ball milling the active materials it was possible to improve their respective performance, the formulations of these electrodes are presented in Table 10 below.

Table 10. Formulations E1-E10, with the mass of each component (their percentage by weight, in the mixture, in brackets).

| ***Electrode*** | ***Active material*** | | ***Iron in the active material*** | ***Mass of active material / mg*** | ***Mass of carbon black / mg*** | ***Mass of $Bi_2S_3$ / mg*** | ***Mass of PTFE / mg*** | ***Mass of Fe /mg*** |
|---|---|---|---|---|---|---|---|---|
| E1 | Iron sulphide | FeS | 63% | 135 (75%) | 18 (10%) | 9 (5%) | 17 (10 %) | 85 |
| E2 | Carbonyl iron | Fe | 100% | 85 (68%) | 18 (14%) | 9 (7%) | 14 (11 %) | 85 |
| E3 | Iron (II,III) oxide | $Fe_3O_4$ | 72% | 118 (73%) | 18 (11%) | 9 (6%) | 16 (10 %) | 85 |
| E4 | Iron (III) oxide | $Fe_2O_3$ | 70% | 121 (73%) | 18 (11%) | 9 (5%) | 17 (11 %) | 85 |
| E5 | Iron oxyhydroxide | FeOOH | 64% | 134 (75%) | 18 (10%) | 9 (5%) | 17 (10 %) | 85 |
| | | | | | | | | |
| E6 | Iron sulphide | FeS | 63% | 165 (77%) | 22 (10%) | 7 (3%) | 21 (10% | 104 |
| E7 | Carbonyl iron | Fe | 100% | 241 (70%) | 52 (15%) | 17 (5%) | 33 (10%) | 241 |
| E8 | Iron (II,III) oxide | $Fe_3O_4$ | 72% | 160 (74%) | 25 (12%) | 8 (4%) | 22 (10%) | 115 |
| E9 | Iron (III) oxide | $Fe_2O_3$ | 70% | 300 (75%) | 45 (11%) | 15 (4%) | 38 (10%) | 210 |
| E10 | Iron oxyhydroxide | FeOOH | 64% | 204 (76%) | 28 (10%) | 9 (3%) | 26 (10%) | 130 |

Electrodes E1-E5 correspond to the five different active materials that have been reported in the literature and that would be interesting to compare under similar conditions. Additionally, similar formulations were prepared in which the active materials were mixed together by ball milling as opposed to manual mixing, in order to determine the influence of this additional step in the performance of the iron electrodes. These five additional electrodes were prepared using powder which were very similar to formulations E1-E5, but in all of these new cases the active material was ball-milled for 15 minutes at 30 Hz using a ball mill mixer. These electrodes were labelled as E6-E10. It has been suggested that ball milling, besides helping to achieve a more homogenous formulation, could help to reduce the size of the active material grain size and this could lead to the development of higher performing electrodes.

For each one of the ten hot pressed iron electrodes (E1-E10), a continuous galvanostatic charge-discharge cycling curve at the C/5 rate was measured for several days. For example for the iron sulphide electrode (E1) a total of 49 cycles were measured over 12 days as seen in Figure 22. At the beginning, this electrode showed very short discharge plateaux but its performance improved over time. This initial period of improvement is usually considered to be due to the formation of

the iron electrode. This formation process consist in charging and discharging repeatedly until a stable discharge capacity is obtained [41,45,48].

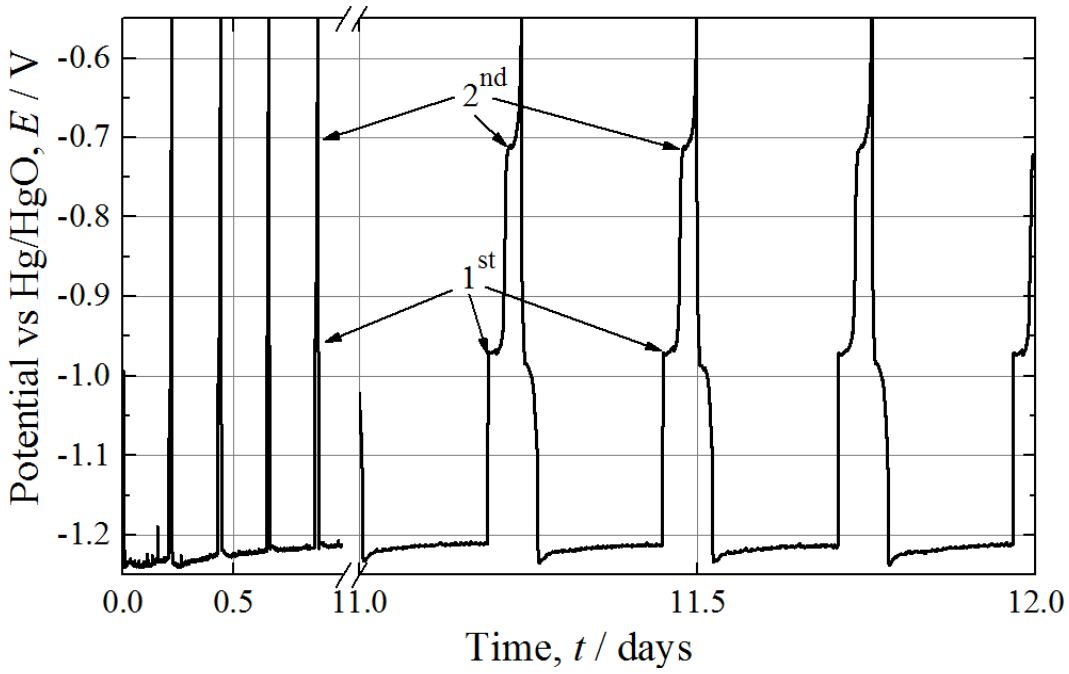


Figure 22. Galvanostatic charge-discharge for the E1 - iron sulphide formulation at C/5 rate ($m_{Fe}$ = 85 mg and $I_{C/5}$ = 22 mA, $V_{co}$ = -0.55 V vs. Hg/HgO). The 1st and 2nd plateaux of some cycles are indicated with arrows.

For clarity, all the charge discharge cycles have been overlaid and are presented in Figure 18. In this experiment, the electrode was charged up to 1,273 mA h $g^{-1}_{Fe}$, which corresponds to the theoretical capacity (no overcharge). The electrode efficiency can be estimated from Figure 23. For example, for the best discharge cycle, this electrode would have had a coulombic efficiency of *ca.* 25%. The mean potential of the four expected charge and discharge plateaux can also be extracted from Figure 23. It is clear that both discharge plateaux for iron sulphide occur at a relatively stable potentials during the 49 cycles at *ca.* -0.96 V and -0.70 V *vs.* Hg/HgO, respectively.

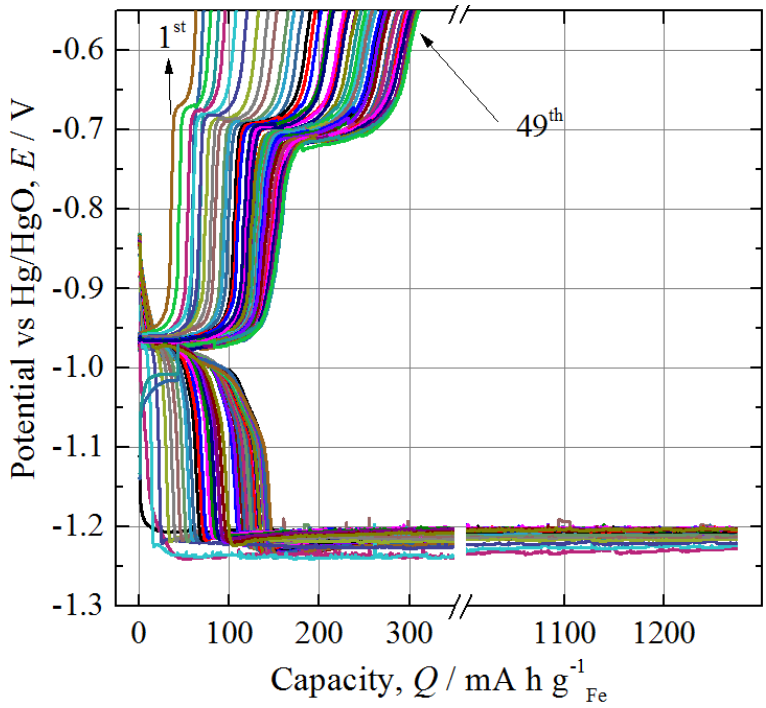


Figure 23. E1- iron sulphide electrode 49 charge-discharge overlaid cycles at C/5 rate ($i_{C/5}$ = 22 mA).

By analysing each discharge curve, it is possible to determine the capacity associated with each plateau; the 1st plateau is described by the discharge capacity up to $E$ = -0.75 V *vs*. Hg/HgO, while the total discharge capacity is described by the discharge capacity up to $E_{cut\ off}$ = -0.55 V *vs*. Hg/HgO. The total discharge capacity for each cycle is presented in Figure 24 and the contributions of each plateau towards the total discharge capacity are discernible. It has been reported that iron electrodes require a formation period up to 30 cycles [46] before reaching a more stable performance. Figure 24, is consistent with this observation, where a continuous increment in performance, especially during the first 25 cycles, where the discharge capacity increased from 25 to 240 mA h $g^{-1}_{Fe}$ before reaching a final capacity of *ca.* 300 mA h $g^{-1}_{Fe}$ by cycle 45.

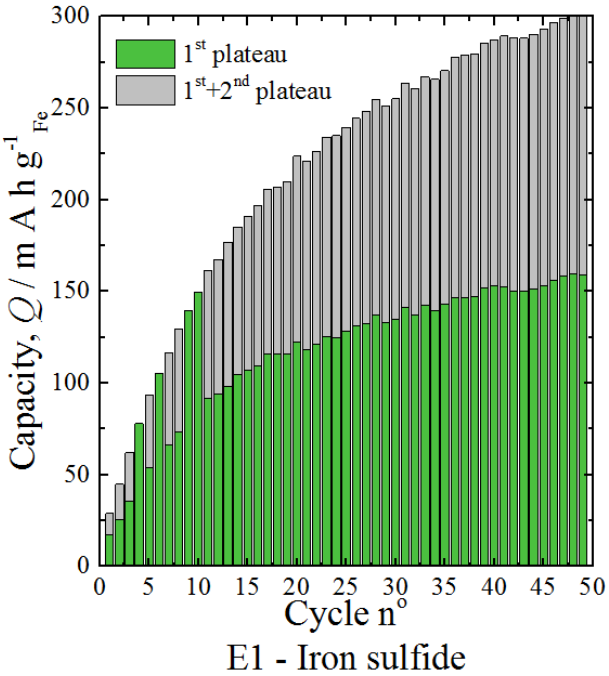


Figure 24. E1- iron sulphide electrode discharge capacity of each cycle.

It has been suggested that ball milling the active materials could improve the performance of iron electrodes. For this reason an electrode is presented for comparison that is similar to E1, but which had its active material subjected to a ball-milling process for 15 minutes at 30 Hz E6 (Figure 25).

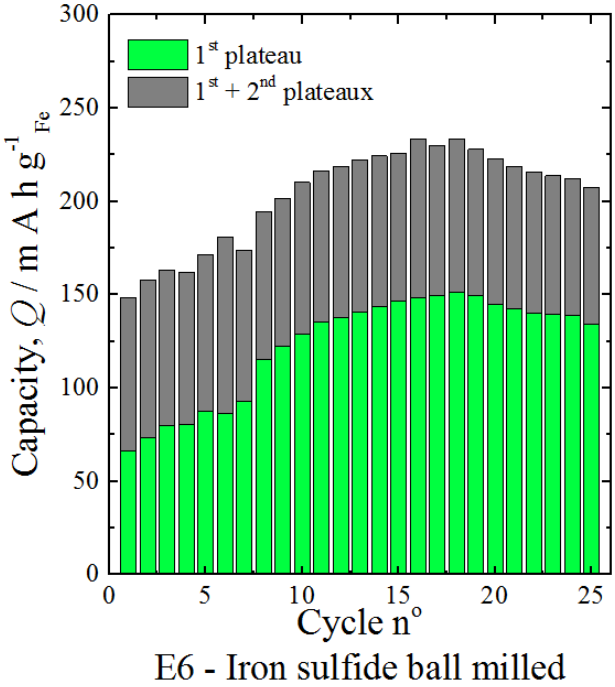


Figure 25. E6 - ball milled iron-sulphide electrode detailed discharged capacity of each cycle

When comparing electrodes E1 and E6, (Figure 24 and Figure 25), it is clear that ball milling had an accelerating effect on the formation process of the iron sulphide electrode, which was particularly noticeable over the first few cycles. The initial discharge capacity for the ball milled electrode (E6) is higher, starting at 150 mA h $g^{-1}_{Fe}$ in contrast with 25 mA h $g^{-1}_{Fe}$ for its non-ball milled counterpart (E1). To achieve a capacity of 175 mA h $g^{-1}_{Fe}$ with the E1 electrode, 15 cycles were required, while this capacity was achieved in just 7 cycles with the ball milled electrode E6. The performance of these two electrodes containing the same active material is summarised in Figure 26. Both electrodes showed a similar mean discharge capacity of *ca.* 210 mA h $g^{-1}_{Fe,}$ there is a larger variation in performance for E1 than for E6, that can be observed from the difference in maximum and minimum values or directly in the standard deviation values (for E1 *ca.* 75 mA h $g^{-1}_{Fe}$ and for E6 three times less).

Ideally, the best iron electrode would have the highest mean discharge capacity value and a small standard deviation, ensuring that it has a relatively consistent performance over time. All of the electrodes were tested for 7-12 days and the number of cycles measured during this time depended on the discharge capacity of the electrode; at least 20 cycles were measured for each electrode.

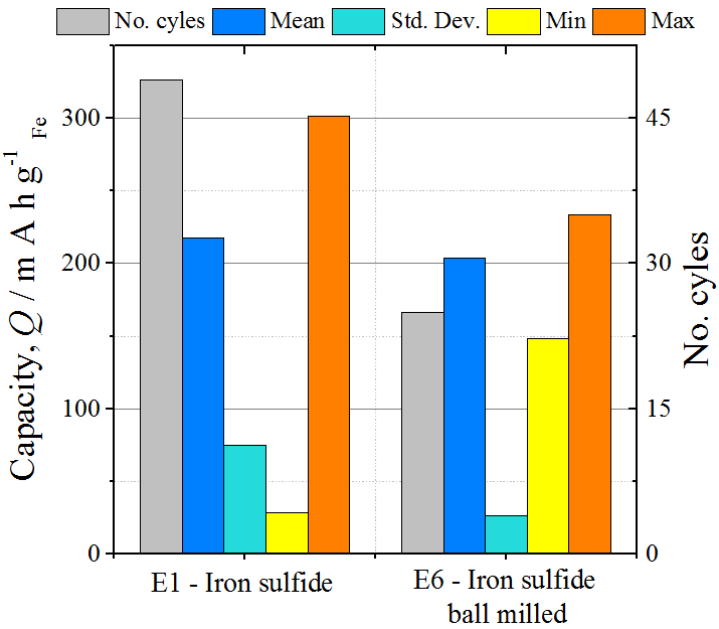


Figure 26. E1 and E6 – Iron sulphide electrodes discharge capacity performance

## 5.7 Discharge capacity of various iron active materials electrodes E2-E5

A similar data analysis from galvanostatic charge-discharge curves was carried out for the remaining eight electrodes. Their respective discharge capacity histograms are presented in Figure 27 for the non-ball milled electrodes, E2-E5 and in Figure 28 for balled-milled ones, E7-E10.

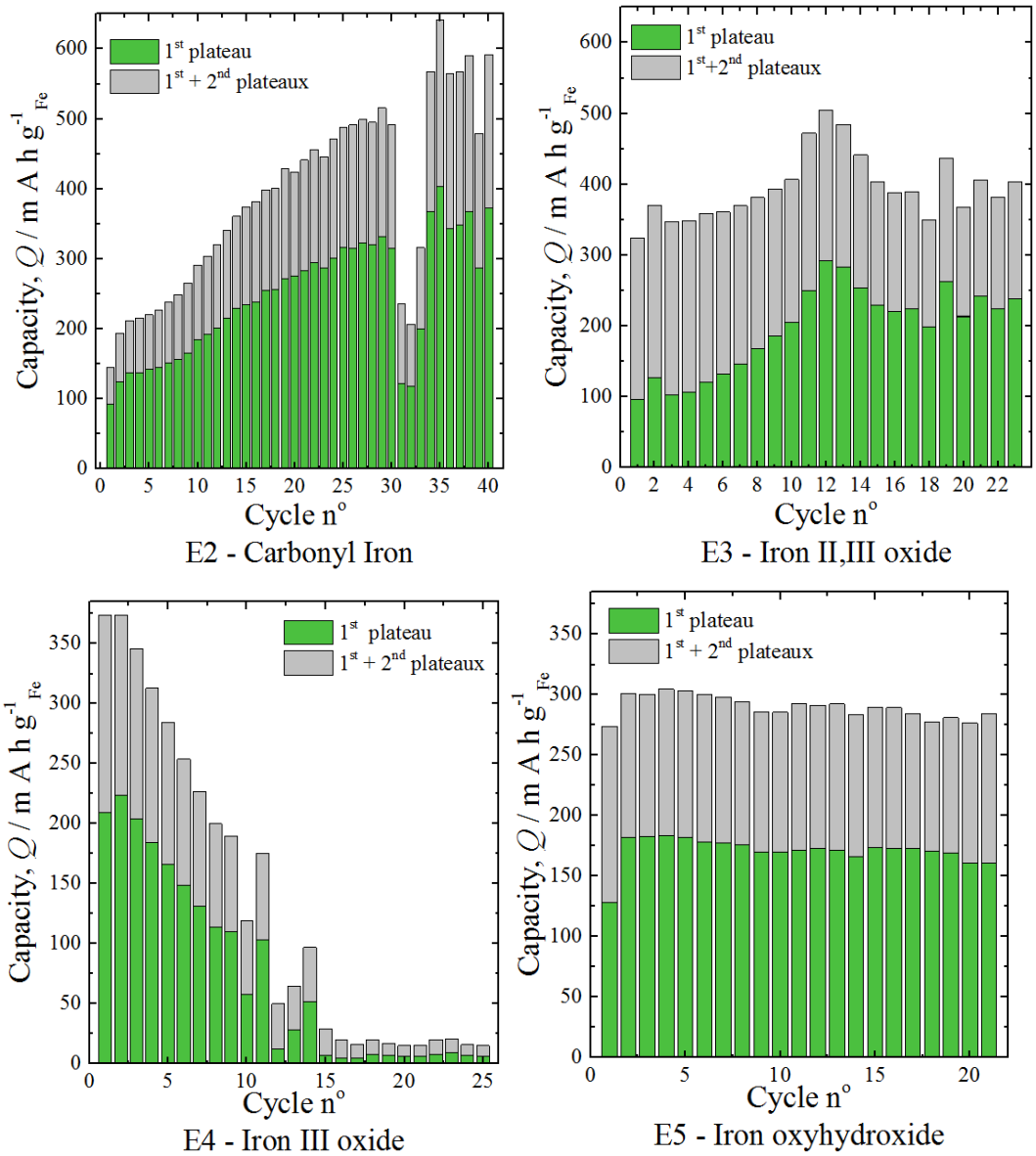


Figure 27. E2-E5 Iron electrodes detailed discharged capacity during each cycle.

In Figure 27, it is interesting to compare how the charge-discharge cycles evolved for the different active materials, for example for the E2 – carbonyl iron electrode the first cycles improve fast at the beginning, during the first 17 cycles but then the

improvement slows down until a final value of *ca.* 600 mA h $g^{-1}_{Fe}$ was achieved. It is also noticeable that there is a considerable drop in the capacity in cycles 31-33. This may be attributable to the previously reported passivation of the iron electrode and trapped hydrogen bubbles within the porous structure of the electrode that do not allow all the active material to be utilised within its core [7,11]. For the E3 – iron (II,III) oxide (magnetite) and the E5 – iron oxyhydroxide (Goethite) electrodes, the discharge capacity remains stable during its operation with mean values of *ca.* 350 and 300 mA h $g^{-1}_{Fe}$, respectively without much variation. Strangely, the performance for the E4 – iron (III) oxide starts with a high capacity around 365 mA h $g^{-1}_{Fe}$ and then decreases sharply and after just 10 cycles its discharge capacity is just 100 mA h $g^{-1}_{Fe}$ and less of 50 mA h $g^{-1}_{Fe}$ from cycle 15 and onwards. This may indicate a strong passivation of the E4 iron electrode, which could be related to the inherent low conductivity of the Fe (III) oxide if it is not combined with a good conductive support material.

## 5.8 Discharge capacity of various ball milled iron formulations electrodes E7-E10

For comparison, in Figure 29 the MDC histograms of the ball milled iron electrodes (E7-E10) are presented. The E7 – ball milled carbonyl iron electrode and the E9 – ball milled iron III oxide electrode did not show such drastic changes between cycles but their capacities were not as high with a MDC of 258 mA h $g^{-1}_{Fe}$ and 120 mA h $g^{-1}_{Fe}$ , respectively. On the other hand, E10, a ball milled iron oxyhydroxide (Goethite) electrode, had a MDC of 395 mA h $g^{-1}_{Fe}$. Much variation can be observed from cycle to cycle, for example the difference between cycle 29$^{th}$ and 30$^{th}$ is as high as 250 mA h $g^{-1}_{Fe.}$ The E8 – iron (II, III) oxide (magnetite) electrode in contrast with the other ones showed a high MDC of 610 mA h $g^{-1}_{Fe}$, the highest discharge capacity of 707 mA h $g^{-1}_{Fe}$ and small changes between cycles.

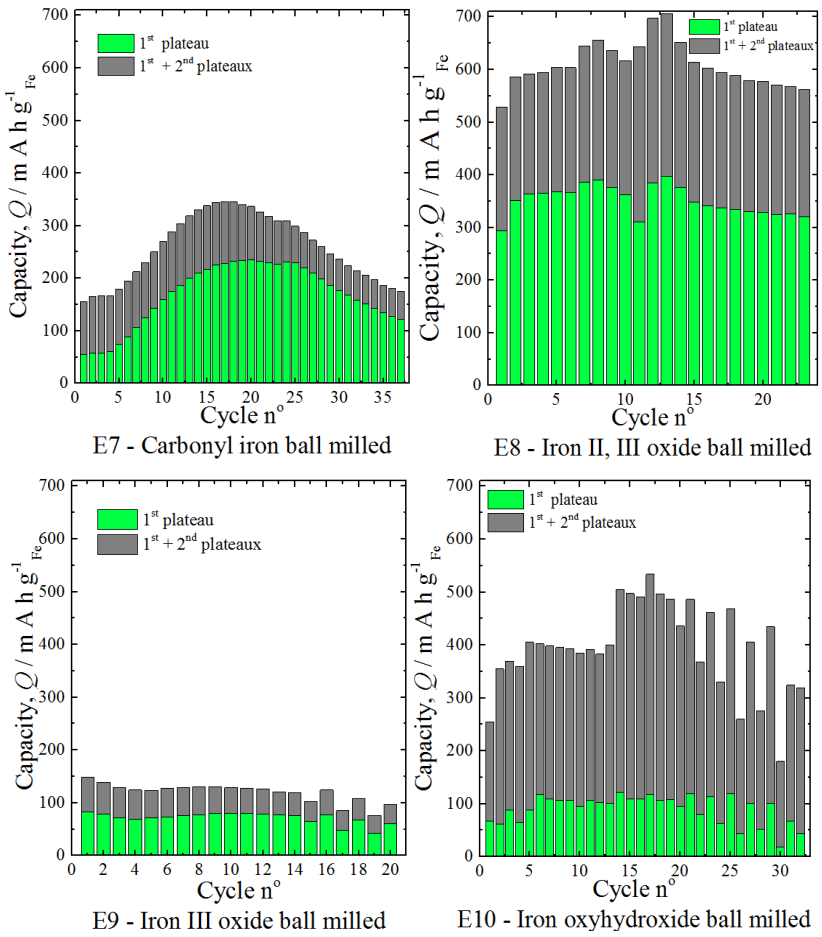


Figure 28. E7-E10 Iron electrodes manufactured with ball milled materials. Detailed discharged capacity of each cycle.

## 5.9 Discharge capacity comparison of all hot-pressed iron electrode formulations, electrodes E1-E10

To determine how the ball milling process affects the performance of the electrodes in more detail, a brief summary of the performance of the 'in-house' prepared electrodes (E1-E10) is presented in Figure 29. It is observable that the Ball milling has acted to strongly increase the capacity of the $Fe_3O_4$ electrodes, but has decreased the capacity of the $Fe_2O_3$ and carbonyl iron electrodes. The FeOOH electrode E8 showed a modest increase in capacity and the FeS electrode E6 showed a modest decrease compared to their non-ball milled counterparts. The effect of the ball milling process on the performance of the electrodes (E1-E10) is summarized in Figure 9. The ball milling has exerted a stabilising effect on all of the electrodes except for FeOOH as evidenced by the lower standard deviations for the electrodes E6-E9. On the whole, the best-performing electrode was E7, ball milled $Fe_3O_4$, with an average discharge capacity of 610 mA h $g^{-1}_{Fe}$. The reason why ball milling has improved the capacity of some iron materials and not others is not evident from the appearance of the electrodes and requires further examination at the microscopic scale as has been done in section 5.10.

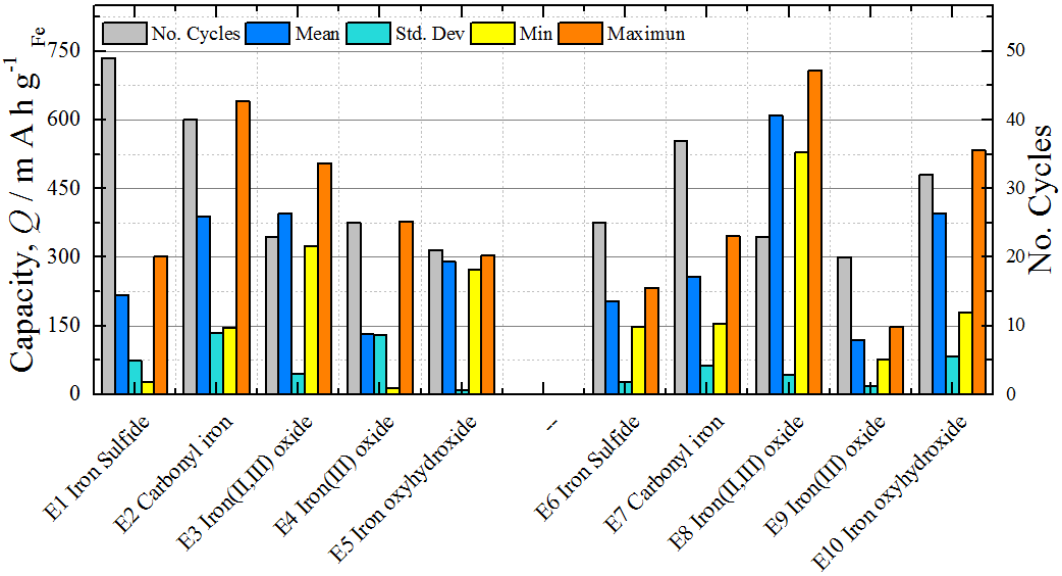


Figure 29. Iron electrodes discharge capacity at the C/5 rate performance summary.

## 5.10 Morphology change on ball milled iron active materials

Figure 30 shows SEM the micrograph images of the iron active materials which were not ball milled before cycling (E1-E5) and their different particle size and morphology can be appreciated. Carbonyl iron and iron sulphide particles can be found in the range of 100-5000 nm. The former has a particle shape that is close to spherical, and the latter has a more prismatic shape. Hematite and magnetite are more homogenous with smaller particle sizes of *ca.* 100 nm and 200 nm, respectively. Finally, goethite shows a very distinctive needle-like structure *ca.* 150 nm across and up to 2000 nm length. The larger size of the carbonyl and iron sulphide particles could explain why electrodes E1 and E2, underwent many cycles before reaching a more stable performance since it takes more time for the ions to be able to penetrate through the structure of the larger particles, as can be seen in Figure 30 and Figure 31. The smaller size of the hematite particles is in agreement with the larger capacity observed, but also be the reason why it passivates the fastest, explaining the observed behaviour of the E4 electrode.

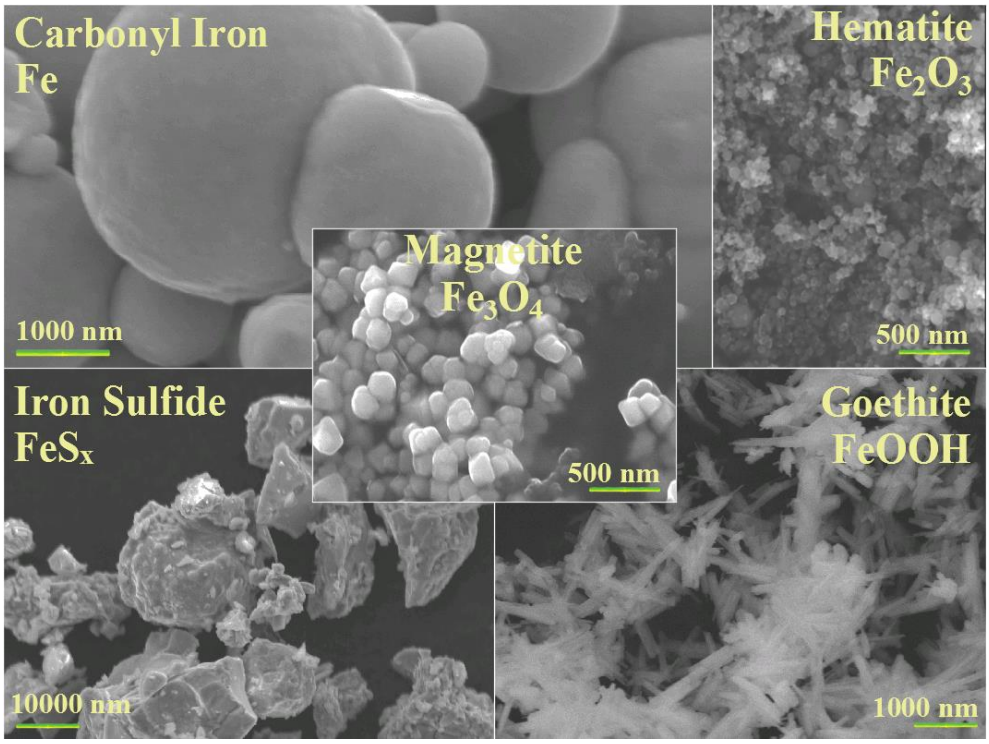


Figure 30. SEM images of different iron active materials before ball milling corresponding to E1-E5 formulations

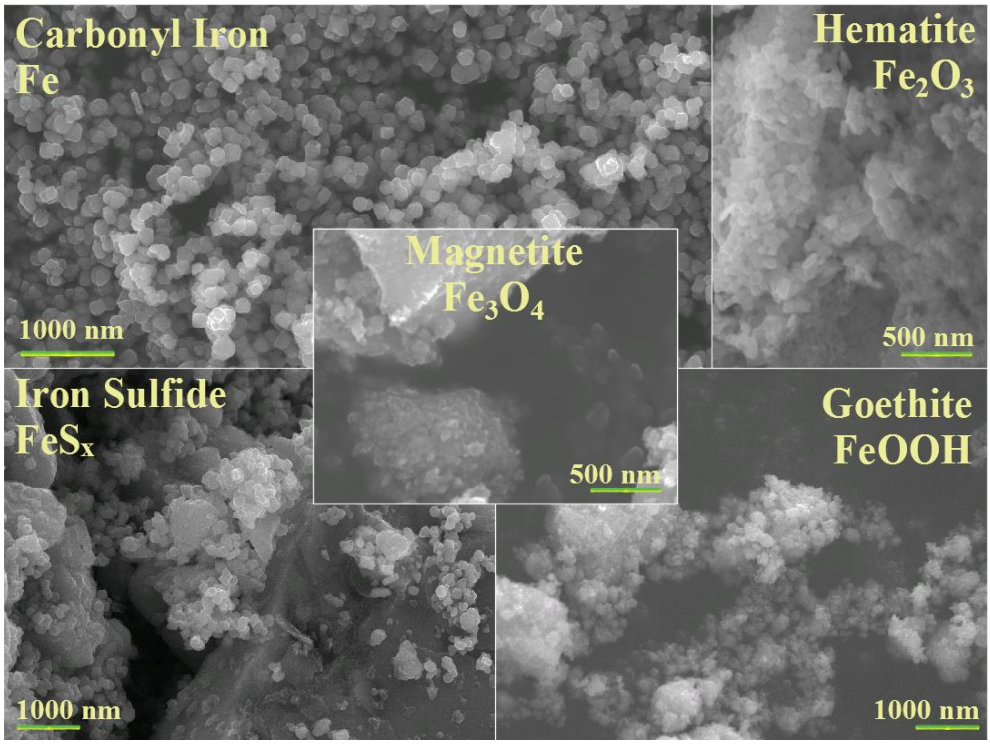


Figure 31. SEM images of different iron active materials after ball milling corresponding to E6-E10 formulations

## 5.11 Discharge capacity comparison with other reported iron electrodes

Finally furthering the analysis of the hot-pressed electrodes (E1-E10), the characteristics of similar iron electrodes in the literature (LR1-LR6) are presented in table 11. Although the reported electrodes use the same active materials, the experimental conditions are not the same, sometimes they included an additive in the electrolyte or electrode, or they report the discharge rate considering only the capacity of the 1st plateau (960 mA h $g^{-1}_{Fe}$) with a cut off potential close to -0.75 V *vs* Hg/HgO. Some electrodes consider the capacity of both plateaux (1273 mA h $g^{-1}_{Fe}$) and have a more positive cut off potential than -0.55 V *vs.* Hg/HgO, some of them even further up to -0.1 V *vs.* Hg/HgO. There is also some variation when reporting the discharge rate either per unit mass, per unit area, or as a C rate related to a specific reaction (1st or 2nd plateau). These additional details can be observed in Table 11. It is important to take this into account since, in general, higher C rates gives lower discharge capacities.

Table 11. Comparison between similar iron electrodes reported in the literature

| | Number of cycles | Mean | Max | Specific Discharge rate | $V_{cut\ off}$ | Electrolyte | Ref |
|---|---|---|---|---|---|---|---|
| | | *mA h g$^{-1}$* | *mA h g$^{-1}$* | | *V vs Hg/HgO* | | |
| *LR1 Iron sulfilde (FeS) 80% + Iron (Fe) 20%* | 7 | 165 | 221 | 192 mA h g$^{-1}$ | -0.8 | 5.1 M KOH 0.3 M LiOH + 0.44 M $K_2S$ | [54] |
| *E1 – Iron sulphide* | 49 | 217 | 301 | 255 mA g$^{-1}$ | -0.55 | 6M KOH solution | n/a |
| *E6 – Iron sulphide ball milled* | 25 | 203 | 233 | 255 mA g$^{-1}$ | -0.55 | 6M KOH solution | n/a |
| *LR2 carbonyl iron sintered, Fe* | 10 | 238 | 258 | 48 mA g$^{-1}$ | -0.75 | KOH (30% w/w) aqueous solution | [55] |
| *LR3 carbonyl Iron, Fe* | 150 | 259 | 404 | 100 mA g$^{-1}$ | -0.8 | 6M KOH solution | [86] |
| *E2 – carbonyl iron* | 40 | 388 | 640 | 255 mA g$^{-1}$ | -0.55 | 6M KOH solution | n/a |
| *E7 – carbonyl iron ball milled* | 37 | 258 | 345 | 255 mA g$^{-1}$ | -0.55 | 6M KOH solution | n/a |
| *LR4 iron (II, III) oxide, $Fe_3O_4$* | 5 | 310 | 360 | 0.5 mA cm$^{-2}$ | -0.75 | 8M KOH + 10mM $K_2S$ | [87] |
| *LR4 iron (II, III) oxide, $Fe_3O_4$* | 5 | 670 | 730 | 0.5 mA cm$^{-2}$ | -0.55 | 8M KOH + 10mM $K_2S$ | [87] |
| *E3 – iron (II,III) oxide* | 23 | 395 | 504 | 255 mA g$^{-1}$ | -0.55 | 6M KOH solution | n/a |
| *E8 – iron (II,III) oxide ball milled* | 23 | 609 | 706 | 255 mA g$^{-1}$ | -0.55 | 6M KOH solution | n/a |
| *LR5 iron (III) oxide, $Fe_2O_3$* | 50 | 579 | 836 | 2 mA cm$^{-2}$ | -0.1 | 8M KOH + 10mM $K_2S$ | [60] |
| *LR6 iron (III) oxide, $Fe_2O_3$* | 29 | 215 | 510 | 0.2 mA cm$^{-2}$ | -0.1 | 8M KOH | [61] |
| *E4 - iron (III) oxide, $Fe_2O_3$* | 25 | 131 | 377 | 255 mA g$^{-1}$ 6 mA cm$^{-2}$ | -0.55 | 6M KOH solution | n/a |
| *E9 - iron (III) oxide ball milled* | 20 | 119 | 148 | 255 mA g$^{-1}$ 11 mA cm$^{-2}$ | -0.55 | 6M KOH solution | n/a |

The information presented in Table 11, is graphically shown in Figure 32, including the MDC and the maximum discharge capacity of the in-house hot pressed electrode E1-E10 for comparison.

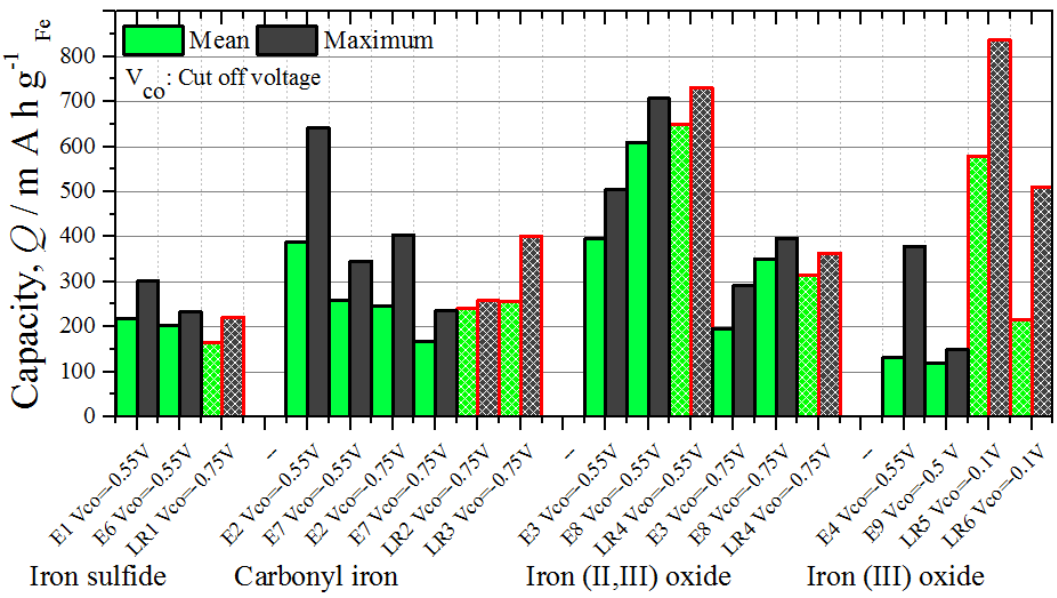


Figure 32. Iron electrode comparison. Note that the references taken from the literature electrodes LR1-LR6, [54,55,60,61,86,87] respectively, have been highlighted to distinguish them from the in-house hot pressed electrodes E1-E10.

The comparison of the iron electrodes capacity developed in this work and those reported in the literature (Figure 32 and Table 11) is discussed below.

*Iron sulphide FeS*: In the first subset of columns of Figure 32 the performance of the electrode reported in [54], consisting of a 80% FeS + 20% Fe electrode (LR6) cycled at 192 mA $g^{-1}_{Fe}$ with a cut off potential of $V_{co}$ = -0.8 V *vs*. Hg/HgO is presented. If only the 1st plateau is considered both E1 and E6 electrodes had a very similar performance with a mean discharge capacity of *ca.* 120 mA $g^{-1}_{Fe}$ , which is just 63% of the discharge capacity achieved by the LR1 formulation (at mA $g^{-1}_{Fe}$), in both cases at the C/5 discharge rate capacity. It is important to mention that this formulation had a slightly different electrolyte, 5.1 M KOH 0.3 M LiOH + 0.44 M $K_2S$; this concentration was suggested from [45] as an optimized empirical formulation.

*Carbonyl Iron*: In the second subset of columns the performance of the carbonyl iron electrodes E2 and E7 is presented, and compared with two similar electrodes reported in the literature, labelled as LR2 a carbonyl sintered electrode with 5% of carbon black [55], and LR3 a hot pressed pure carbonyl iron electrode [86].

Since these electrodes had been tested with different cut-off voltages in Figure 32, the discharge capacity with different cut-off voltages is also presented, firstly

considering both discharge plateaux ($E_{cut\ off}$ = -0.55 V *vs*. Hg/HgO), and then considering only the capacity of the 1st plateau (V = -0.75 V *vs*. Hg/HgO). The latter case can be compared with the LR1 and LR2 electrodes in similar conditions.

When comparing these electrodes at the same cut-off potential, it is noticeable that the discharge capacity contained in the 1st plateau of the E2 carbonyl is similar to those for both LR2 and LR3, *ca.* 240 mA h $g^{-1}_{Fe.}$ However, it is worth mentioning that the E2 electrode results have been achieved at a higher discharge current density of 255 mA $g^{-1}_{Fe}$ in comparison with 50 mA $g^{-1}_{Fe}$ and 100 mA $g^{-1}_{Fe}$, of the LR1 and LR2 electrodes respectively. This means that the E2 sample would most likely perform better in terms of capacity than LR2 and LR3 at the current density used in these reports.

Reference [55] also reported the discharge performance at the C/2 rate for a carbonyl iron electrode, with an initial value of 350 mA h $g^{-1}_{Fe}$ after formation and 100 mA h $g^{-1}_{Fe}$ after 100 cycles, and a mean value of *ca.* 225 mA h $g^{-1}_{Fe.}$ This shows that there is a typical variation in the discharge capacity of this type of electrode that was also observed here in the E2 formulation with a minimum value of 92 mA h $g^{-1}_{Fe}$ and a maximum of 403 mA h $g^{-1}_{Fe}$.

The use of carbonyl iron has been reported many times in hot-pressed electrodes resulting in specific discharge capacities of 275 mA h $g^{-1}$ at the C/5 discharge rate [41,46,47,55], which compares well with E2 and E7, that have a mean discharge capacity of 390 mA h $g^{-1}_{Fe}$ and 255 mA h $g^{-1}_{Fe}$ respectively, when considering both discharge plateaux.

*Iron (II, III) oxide ($Fe_3O_4$ magnetite):* in the third subset of columns in Figure 32, the performance of the E3 and E8 electrodes is compared with a similar iron (II, III) oxide electrode reported in the literature [87] labelled as LR4. The LR4 electrode was reported with a mean capacity of 745 mA h $g^{-1}$, a maximum discharge capacity of 786 mA h $g^{-1}$ with a $V_{cut\ off}$ = -0.1 V *vs*. Hg/HgO when cycled at 0.5 mA $cm^{-2}$. Since the area and mass are not reported for the LR4 electrode, the current density can only be compared per unit area rather than per mass of iron, in the case of the electrodes E3 and E7 it was 11 mA $cm^{-2}$ and 16 mA $cm^{-2}$ respectively. Taking this into consideration, whilst it is true that the reported capacity of the LR4 electrodes is very high, the current densities are considerably smaller and a less negative cut

off potential was used. In reference [87], 5 of 30 discharged profiles were presented from which it was possible to estimate the discharge capacity at the cut-off voltages of $E$ = -0.55 V and -0.75 V *vs*. Hg/HgO to compare with the E3 and E7 electrodes. Considering this, the E7 electrode achieved a high discharge capacity of 610 mA h $g^{-1}_{Fe}$ (81% of LR4) but at a much higher current density of 16 mA $cm^{-2}$ (32 times higher than LR4) or equivalent to a $I_{C/5}$ = 255 mA $g^{-1}_{Fe}$.

*Iron III oxide ($Fe_2O_3$):* in a similar way, the fourth subset of columns compare the E4 and E9 electrodes with two electrodes that use the same active material: LR5, an $Fe_2O_3$ dispersed over a mesoporous carbon nanofiber reported in [60], and LR6, an $Fe_2O_3$ dispersed over acetylene black reported in [61]. Both electrodes had a much higher performance than E4 and E9 $Fe_2O_3$ electrodes that had just been mixed with carbon black rather than being dispersed by a chemical method. Unlike the other cases where similar performances were achieved, in this case there is a large variation that cannot be attributed just to the difference in discharge rates.

Whilst E4 and E9 had a MDC of *ca.* 125 mA h $g^{-1}_{Fe}$ at 6 mA $cm^{-2}$ and 11 mA $cm^{-2}$ discharge rates respectively, the LR5 and LR6 had a MDC of 579 and 215 at 2 mA $cm^{-2}$ and 0.2 mA $cm^{-2}$ respectively, which confirms that improvement in the dispersion method of the $Fe_2O_3$ particles over carbon nanostructure as presented in [60–62] can increase the capacity of the electrode (although at the expense of greater electrode synthesis time and cost).

## 5.12 Conclusions and further work on the iron electrode

A series of experiments to compare the discharge capacity (in mA h $g^{-1}_{Fe}$) of ten different hot-pressed iron electrodes formulations using five different active materials with and without ball milled was performed. The results indicated that:

- The iron III oxide showed a good initial capacity (375 mA h $g^{-1}_{Fe}$), which however faded away very quickly, just after 10 cycles. This could be associated with the low conductivity of this particular oxide, which suggests that this iron material always needs to be well dispersed over a conductive support material to achieve a higher capacity, as has been shown in similar

type of electrodes. In further studies, it would be interesting to compare the performance of this material when it has been distributed more homogenously or nanostructured over a more electrically conductive material such a carbon black [88,89] (*ca*. 4 S $cm^{-2}$).

- The carbonyl iron and iron sulphide electrodes clearly underwent a more distinctive formation phase which was more observable than for the other formulations. In the particular case of the iron sulphide, this formation process was accelerated via ball-milling. On the contrary the ball milling seems to have had a negative effect in the discharge capacity of the carbonyl iron.
- The iron II, III oxide seems to have benefited from the ball-milling process. Having an initial capacity of 395 mA h $g^{-1}_{Fe}$, the electrode assembled with ball milled composition increased to 610 mA h $g^{-1}_{Fe}$, and it was the most promising material iron electrode in these studies.

When comparing the performance of our 'in-house' electrodes with others reported in the literature, the following can be highlighted:

- The use of carbonyl iron has been reported in many occasions in hot-pressed electrodes with mean specific discharge capacities of 275 mA h $g^{-1}$ at C/5 discharge rate [41,46,47,55] in the first discharge plateau, which is in agreement with E2 that had a mean discharge capacity of 250 mA h $g^{-1}_{Fe}$ in the first plateau with the possibility to be extended up to 390 mA h $g\text{-}1_{Fe}$ when considering both discharge plateaux. Ball-milling does not improve the performance of carbonyl iron.
- The iron II, III oxide ball milled electrode E8 achieved a high discharge capacity of 610 mA h $g^{-1}_{Fe,}$ that is slightly lower than others reported in the literature (81% of LR4) but at a much higher current density of 16 mA $cm^{-2}$ (32 times higher than LR4) equivalent to a $I_{C/5}$ = 255 mA $g^{-1}_{Fe}$).
- The iron III oxide E4 and E9 electrodes have a much lower capacity (*ca*. 125 mA h $g^{-1}_{Fe}$) than the ones reported in the literature where this material has been nanostructured with nanofibers LR5 and LR6 (just 15% and 25% of the reported values respectively). This nanostructuring process seems to be a requirement to make this $Fe_2O_3$ material to have a high performance in

hot-pressed iron electrodes to make up for its low electrical conductivity in comparison with other iron materials, reason why it requires to be well dispersed on a conductive support.

- The goethite electrodes showed a very stable performance, as evidenced by small standard deviation in the measured discharge capacity (9 mA h $g^{-1}_{Fe}$ for E5) and did benefit from the ball milling process, increasing in capacity by 105 mA h $g^{-1}_{Fe}$. This is the first time that this type of active material has been reported for hot pressed iron electrodes.

# Chapter 6: Bifunctional air electrode experiments and results

In this chapter the experimental description results and discussion on GDE is presented. The technique that was used to develop our in-house GDE is the one that was previously described in [4] where Pd was used as a bifunctional catalyst to develop a GDE using carbon cloth as a support material. This line of research was continued using novel bifunctional materials such as $La_{0.6}Sr_{0.4}Fe_{0.8}Co_{0.2}O_3$ perovskites and Ni-Fe hex-cyanoferrate and their combinations. Part of this research included testing various catalyst loadings to optimise its performance. As part of the characterisation of this component SEM images of the bifunctional catalysts and the GDE were taken in combination with x-ray tomography.

## 6.1 Bifunctional electro-catalyst preparation

The Pd/C GDE comprised three main parts bound together by hot-pressing: 1) a gas diffusion layer, 2) a catalyst layer and 3) a current collector. In order to produce the gas diffusion layer described previously in Figure 15 chapter 4, a paste was made from 80 wt.% of high surface area carbon (*ca.* 64 $m^2$ $g^{-1}$, supplied by IMERYS Graphite & Carbon) mixed with 20% wt. PTFE (DISP 30 solution, DuPont) and 10 $cm^3$ water per 1 g of solids. The paste was rolled evenly over a 5 cm × 5 cm piece of carbon cloth (0.11 mm thickness, treated with 25% wt. PTFE from FuelCell.com) then hot-pressed at 180 ºC and 250 kPa for 10 minutes to a thickness of approximately 100 µm.

The catalyst layer included 30 % wt. catalysts/C sonicated for 15 minutes in a 5% wt. Nafion solution containing aliphatic alcohols (from Sigma Aldrich), with a weight ratio of 3:2 catalysts to Nafion. The sonication resulted in a black viscous ink that was evenly spread on top of the gas diffusion layer (which was not allowed to dry out in order to prevent it from detaching from the carbon cloth before hot-pressing). The mass of the 30% wt. Pd/C catalyst was calculated to ensure the desired loading of each specific catalyst on the surface of the electrode. Finally, a piece of expanded nickel mesh (Dexmet, 32 mesh, 0.05 mm thick) was cut to size

and placed on top of the catalyst layer. The three layers comprising the air electrode were placed in a hydraulic press (Carver, model 3851) whilst still slightly wet and pressed for 2 minutes at 140 °C and 250 kPa.

The electrode was coated using non-stick silicone paper to prevent it from sticking onto the plates of the hot-press. The electrode was carefully removed from the press and left to cool at room temperature (20 °C).

The resultant bi-functional air electrode schematic is shown in Figure 33 and in Figure 34 the resulting GDE is presented together with a SEM of its cross section.

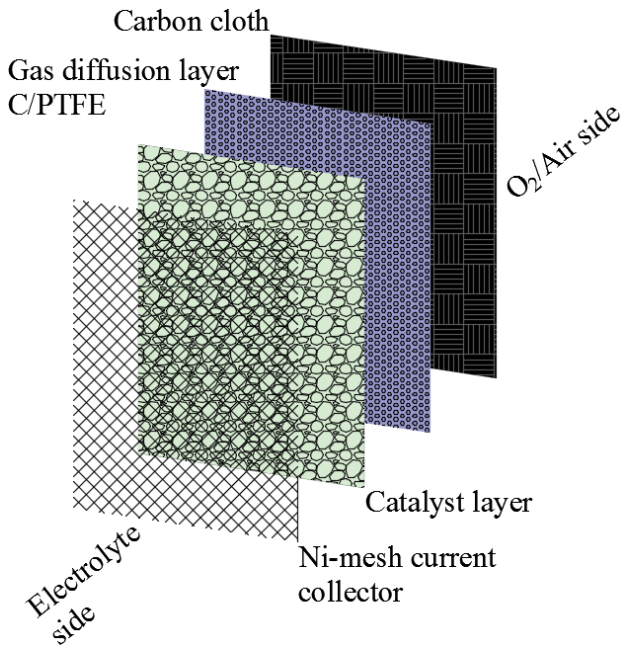


Figure 33. Bi-functional air electrodes schematics. Carbon cloth as support material 80% carbon and 20% PTFE as hydrophobic layer, a Pd catalyst loading of 0.5 mg $cm^{-2}$ and Ni mesh as current collector hot pressed at 140 °C and 250 kPa.

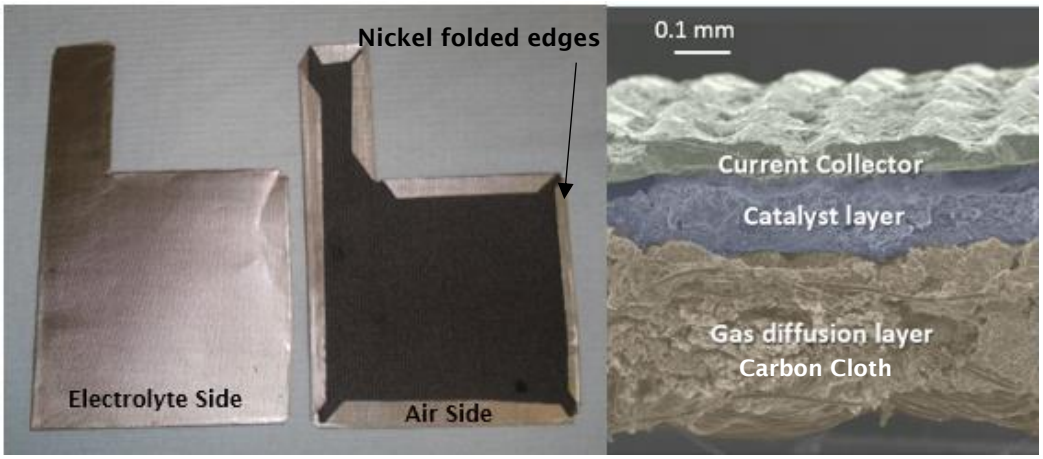


Figure 34. Left: Bi-functional in-house manufactured (5cm x 5cm x 0.5 mm) air electrode. Right: SEM image of its cross-section [4].

## 6.1 Bifunctional catalyst preparation

In the following experiments the performance of three different electro-catalyst loadings and its combinations were studied. In this sections the information related to the synthesis of these materials is described.

*Ni-Fe hex cyanoferrate catalyst synthesis*

A 50 $cm^3$ aqueous solution containing 0.12 mol $dm^{-3}$ $NiSO_4.6H_2O$ and 0.03 mol $dm^{-3}$ $FeSO_4.7H_2O$ was added to a 50 $cm^3$ solution of 0.1 mol $dm^{-3}$ $3[Fe(CN)_6]$ and stirred overnight at 1200 rpm and 20 C. The solution was centrifuged to separate the Ni-Fe HCF catalyst, which was then dried at 60 C for 24 hours. To increase the conductivity, the resulting material was mixed with 10 wt.% carbon black (supplied by IMERYS Graphite & Carbon, 220 $m^2$ $g^{-1}$ surface area), by ball milling at 30 Hz for 3 minutes.

*Pd/C catalyst synthesis*

The detailed synthesis of this material has been described elsewhere [90,91]. Briefly, a solution of $Na_6Pd(SO_3)_4$ at acidic pH was stirred for 1 hour. In the meantime, the carbon support (C, supplied by IMERYS Graphite & Carbon, 220 $m^2$ $g^{-1}$ surface area) was dispersed in aqueous solution at 80 C by means of ultrasonic agitation in a water bath to form a slurry. The former solution was added to the metallic precursor solution and subsequently decomposed with $H_2O_2$ at pH

5.5 until no further reaction was visible, obtaining the colloidal from of PdOx/C. After filtration, the collected powder was reduced in a $H_2$/Ar stream at room temperature (23 C) for 30 minutes to obtain the 30 wt% Pd/C catalyst.

*LSFCO perovskite catalyst synthesis*

The LSFCO catalyst was synthesized by a method described elsewhere [66,92]. The as-synthesized LSFCO was mixed with the carbon black, C, supplied by Imerys Graphite & Carbon (220m$^2$ g$^{-1}$ specific surface area) in a ball-milling procedure in isopropanol at 1.6 Hz for 2 h in a 1:1 ratio (by weight %), to form the 50 wt% LSFCO/C catalyst.

## 6.2 Electro-chemical characterisation of GDE

A potentiostat (Ivium n-stat) was connected to a 3-electrode glass cell fitted with a glass jacket to circulate water (Julabo, model F12-EH water bath), a 1 cm$^2$ platinum mesh counter electrode and a Hg/HgO (1 mol dm$^{-3}$ KOH) reference electrode (Hach-Lange, - 0.115 V *vs.* SHE). The GDE was clamped onto a glass flange of the 3-electrode cell, exposing a 0.785 cm$^2$ circular area to the 6 M KOH electrolyte. Oxygen gas was circulated at atmospheric pressure to the back of the GDE at a volumetric flow rate of 100 ml min$^{-1}$.

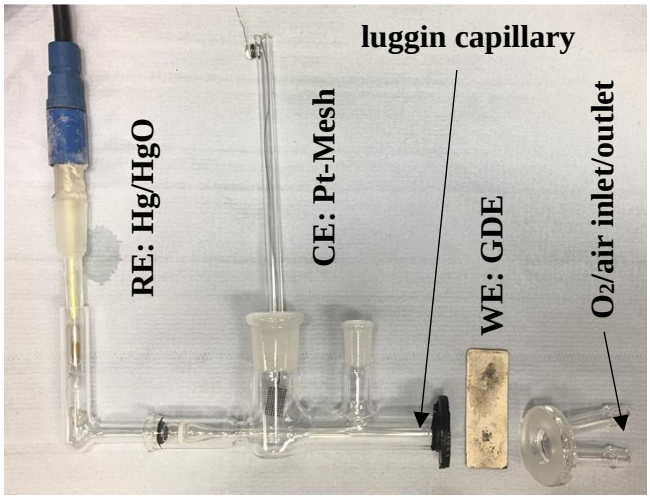


Figure 35. Experimental set up to test the GDE. Pt mesh counter electrode in 6 M KOH electrolyte, oxygen/air supplied to the back part of the air electrode at 100 ml min$^{-1}$ and Hg/HgO as reference electrode.

With the experimental set up described in the previous paragraph three different types of experiments were performed initially various formulations, using Palladium, Ni-Fe HCF, LSFCO perovskites and a combination of the three of them for the loading optimisation studies (see next section).

1. The first one is a cyclic voltammetry of the GDE using different catalysts to observe the onset potentials for the ORR and OER and to compare the observed current density in each case. Cyclic voltammograms were recorded at a linear sweep rate of 1 mV $s^{-1}$. A fresh piece of electrode was used for each scan or each series of charge-discharge cycles.

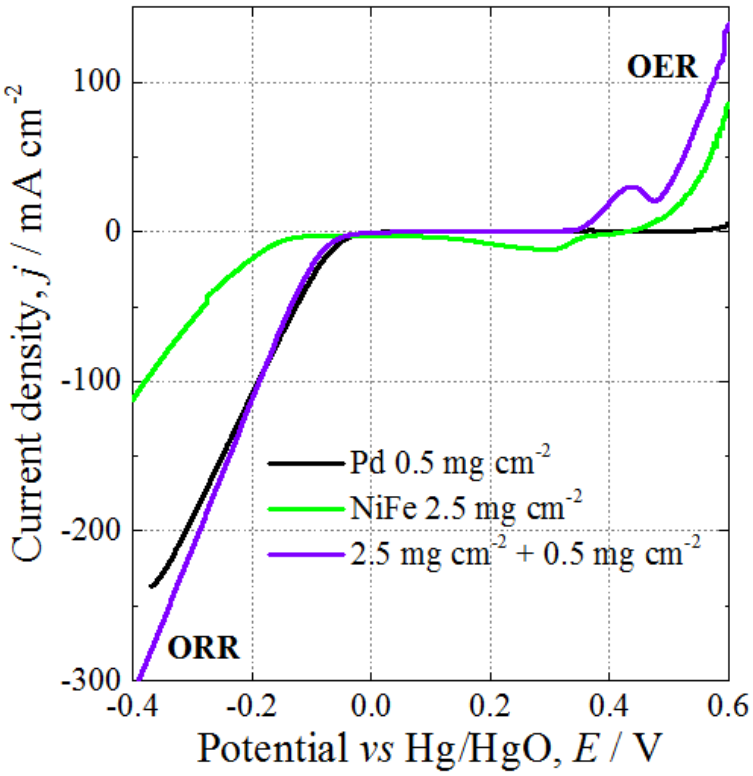


Figure 36. Cyclic voltammograms for 3 different electro-catalysts formulations for GDE. Scan rate 1 mV $s^{-1}$ in 6 M KOH, with 100 mL $min^{-1}$ $O_2$ flow into the back of the electrodes.

In Figure 36 the forward scan of the cyclic voltammetry is presented to compare the performance of the Pd/C and the Ni-Fe HCF. As expected according to the literature review Pd has a strong ORR activity, which is reflected on a high current almost twice as high for Pd/C than for Ni-Fe HCF (-240 mA $cm^2$ and -110 mA $cm^2$ observed at *ca* -0.4 V vs Hg/HgO respectively). On the other hand the Ni-Fe has a better OER than Pd/C, which is reflected on a larger current density of *ca* 80 mA

$cm^2$ for the Ni-Fe HCF in comparison to just 5 mA $cm^2$ for the Pd/C electro-catalyst observed at 0.6 V vs Hg/HgO.

What is interesting is the performance of the combination of both catalyst Pd/C + Ni-Fe HCF which shows and synergic effect with an enhanced performance for both the ORR and the OER which reached a value of -300 mA $cm^2$ for ORR and 140 for the OER at -0.4 V and 0.6 V vs Hg/HgO respectively.

2. The second type of experiments is a 30 min reduction – 30 min oxidation protocol (cycling between the OER-ORR) at 20 mA $cm^{-2}$ for 96 hr, this is to observe if there is some degradation when cycled for longer periods.

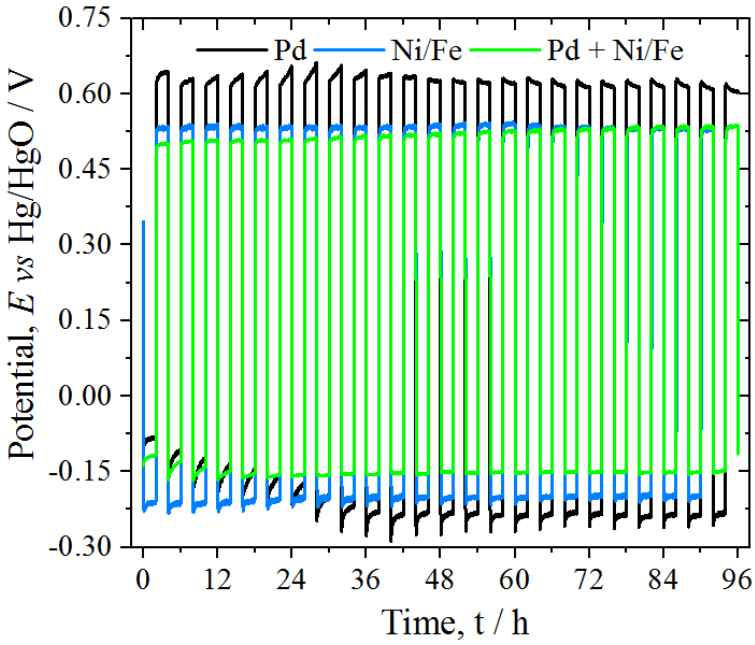


Figure 37. Reduction (30 mins) – oxidation (30 mins) profiles of GDE using 3 different electro-catalysts in GDE at 20 mA $cm^{-2}$ in 6 M KOH, with 100 ml $min^{-1}$ $O_2$ flow into the back of the electrodes.

From Figure 37, it is observable that for the Pd electrode there is a more noticeable degradation in performance for the OER with each cycle during the first 10 cycles, which may be attributable to the carbon corrosion occurring close to the OER.

The Ni/Fe GDE did not show any considerable change in performance during the experiment and the GDE with the combination of both catalyst showed a very slight deterioration during the first 3 cycles as well during the charging phase (towards the OER), afterwards the performance of the electrode appears to be very steady and consistent with little variation between cycles.

3. The third type of experiments will be reduction-oxidation profiles (30 minutes reduction, 30 minutes oxidation) at various current densities ranging from [40-2000] mA cm$^{-2}$. These profiles will allow us to see if the GDE can perform steadily for longer periods and if they are able to withstand different current densities as can be seen in Figure 38.

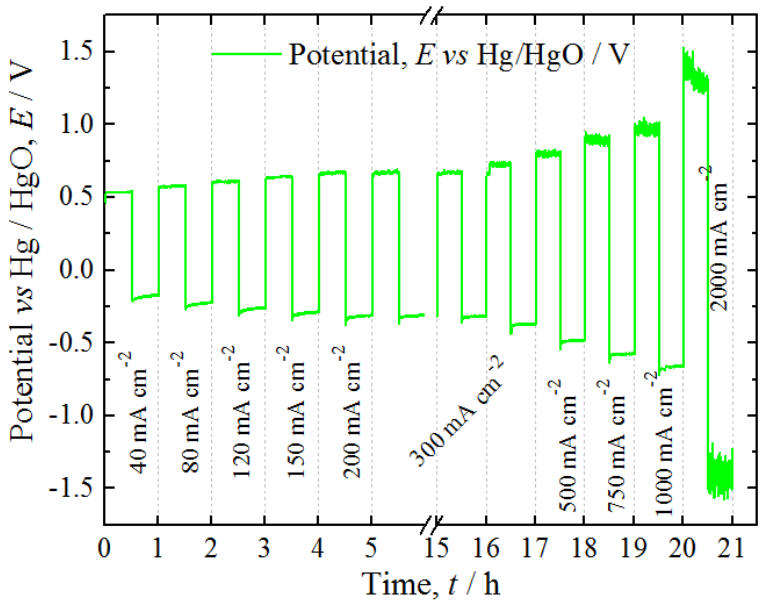


Figure 38. Reduction-oxidation profiles of the Ni/Fe + Pd/C catalysed gas diffusion air electrodes at [40 - 2000 mA cm$^{-2}$ current density in 6 M KOH, with 100 ml min$^{-1}$ $O_2$ flow into the back of the electrodes.

From Figure 38 as expected the associated over potentials are larger at larger current-densities, what is very appealing to see is that even at a relatively high current-density of 300 mA cm$^{-2}$, the performance of the electrode was steady over various cycles. That is why it was decided to apply higher currents-densities until a considerable effect in its performance was observed, which is what can be observed when 1000 mA cm$^{-2}$ and 2000 mA cm$^{-2}$ current-densities were applied.

The performance degradation observed at high current densities could be related to the corrosion of C at such high potentials (>0.9 V vs Hg/HgO), even though certain types of commercial carbon have been pre-treated to be more corrosion resistant, under normal conditions carbon offers good resistance during the ORR in alkaline media, but that is not the case for the OER.

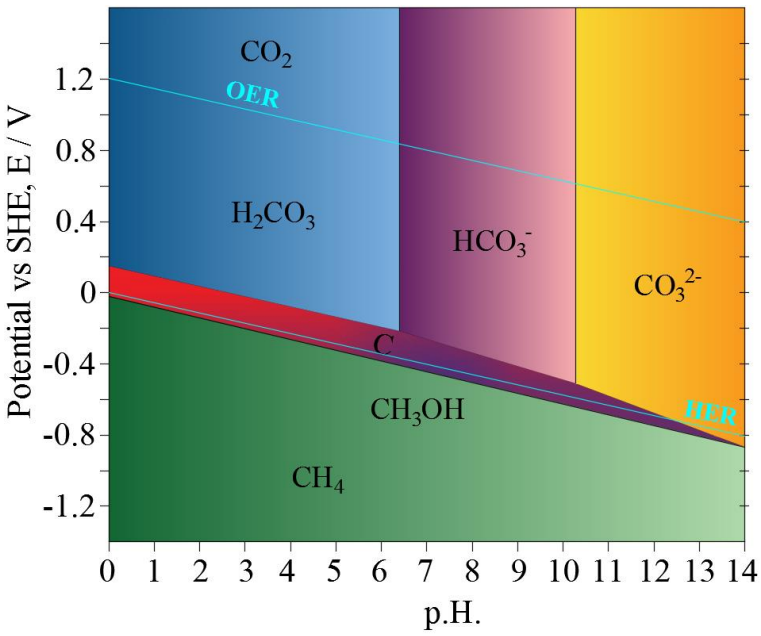


Figure 39. Simplified Pourbaix diagram for C, adapted from [93,94] .

In the Pourbaix diagram for C presented in Figure 39, it is appreciable that the OER in both alkaline and acid media, occurs at a potential that is far away from the equilibrium potential for C (compare the position for the OER reaction and the region where C is stable). This means that when applying the required potential to promote the OER, the carbon substrate is driven out of its equilibrium window promoting its corrosion to $CO_3^{2-}$ within the electrolyte.

From the same experiment it is possible to plot the potential at what the OER and the ORR are occurring at various current-densities as observed in Figure 40. Again it is appreciable how much the associated over potential losses increase at higher current densities with a particularly high increase for both the OER and ORR when it was increased from 1000 mA $cm^{-2}$ to 2000 mA $cm^{-2}$.

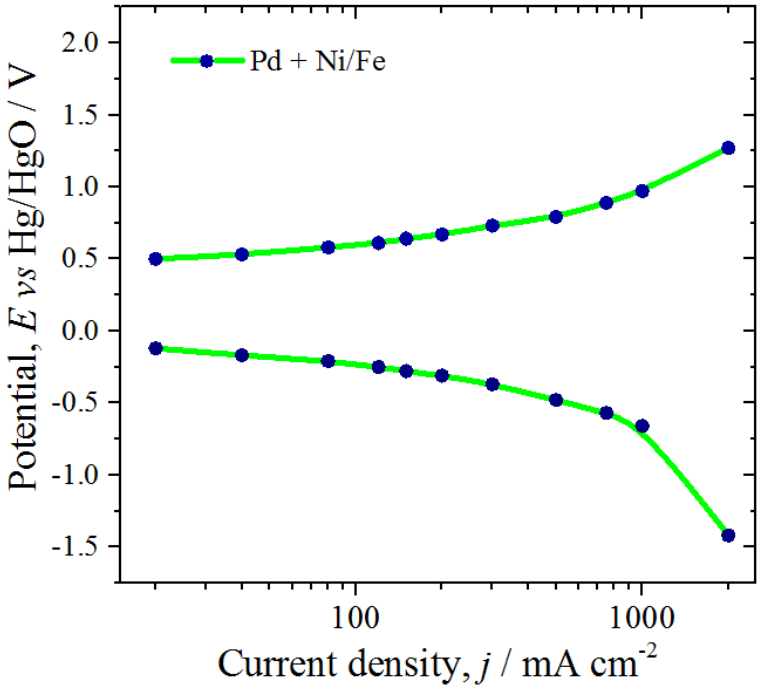


Figure 40. Charge-discharge potential E at various current densities for the GDE with Ni/Fe + Pd.

## 6.3 Bifunctional air electrode catalyst loading optimization

In order to continue this line of research presented in section 6.2, it was decided to carry some additional experiments to optimise the loadings of the Pd, Ni/Fe and LFSCO electrocatalyst. For example in Figure 41 five additional GDE electrodes were compared, each one of them have a different Pd loading. From these results it seems that the optimum loading is 2.5 mg $cm^{-2}$ and that adding more than this actually diminish its performance. Again it is observable that Pd has a very good performance towards the ORR in comparison with its catalytic properties towards the OER.

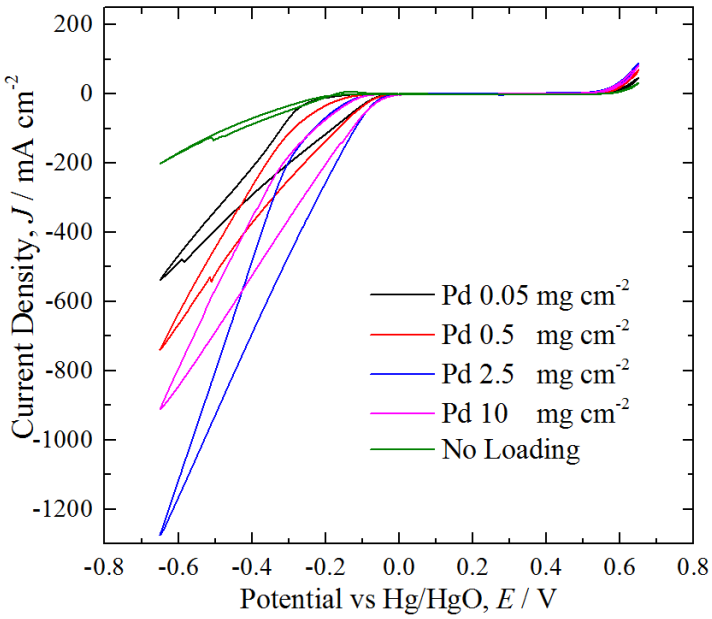


Figure 41. Cycle voltammograms for both the OER and ORR of Pd/C at various loadings ranging from 0.5 mg $cm^{-2}$ -10 mg $cm^{-2}$. Pt mesh counter electrode in 6 M KOH Oxygen (99.999%, BOC) supplied at 100 $cm^3$ $min^{-1}$ at a scan rate of 10 mV $s^{-1}$.

In a similar way the loading of Ni/Fe was varied between 0.5 mg $cm^{-2}$ to 10 mg $cm^{-2}$ in this case the best performance toward the OER was observed with a loading of 5 and 10 mg $cm^{-2}$ as can be seen in Figure 42.

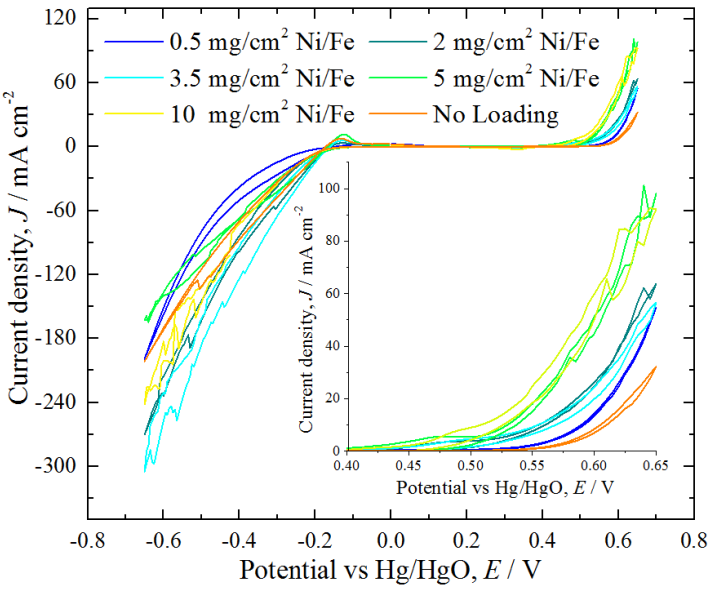


Figure 42. Cycle voltammograms for both the OER and ORR of Ni-Fe HCF/C at various loadings ranging from 0.5 mg $cm^{-2}$ -10 mg $cm^{-2}$. Pt mesh counter electrode in 6 M KOH Oxygen (99.999%, BOC) supplied at 100 $cm^3$ $min^{-1}$ at a scan rate of 10 mV $s^{-1}$.

From the previous results it would seem that a loading of Pd *ca.* 2.5 mg cm$^{-2}$ and 5 mg cm$^{-2}$ of Ni/Fe would be the ideal loading. Nevertheless it seems that there is a limit to the amount of catalyst that can be dispersed over the supporting carbon material (after certain amount it becomes hard to add an additional layer of catalyst over the carbon cloth that looks clearly saturated) that is why a loading of 2 mg cm$^{-2}$ for Pd + 4 mg cm$^{-2}$ for Ni-Fe HCF was used as a compromise together with some other similar loadings, as can be seen in Figure 43.

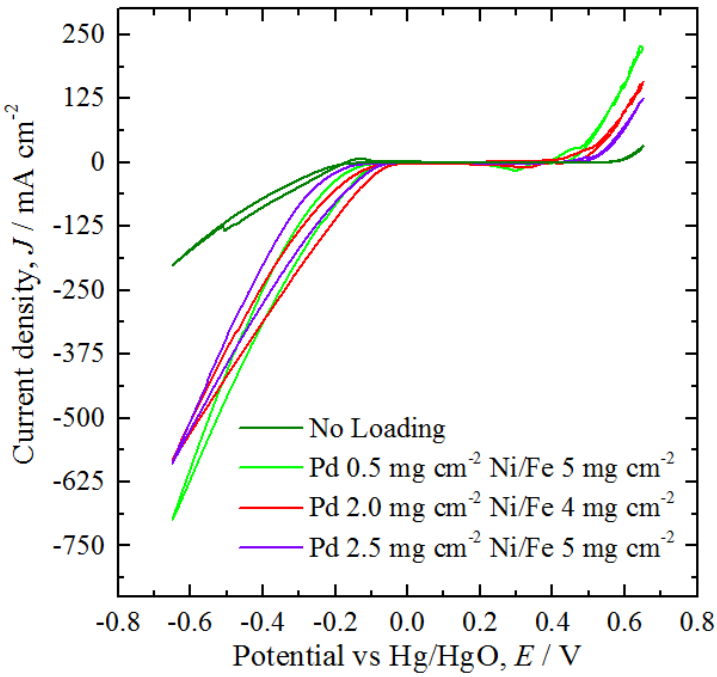


Figure 43. Polarization curves of various gas diffusion electrodes that only differs in the respective loading of both Ni/Fe hexacyanoferrate and Pd/C electrocatalysts loadings Scan rate at 10 mV s$^{-1}$.

At a different stage of my Ph.D. I continued researching novel materials as bifunctional catalyst and one of the materials that have been reported in the literature to have a good bifunctional activity are perovskites, in particular LSFCO-perovskites. In a similar way as in the previous section the cyclic voltammograms obtained using LSFCO is presented in Figure 44.

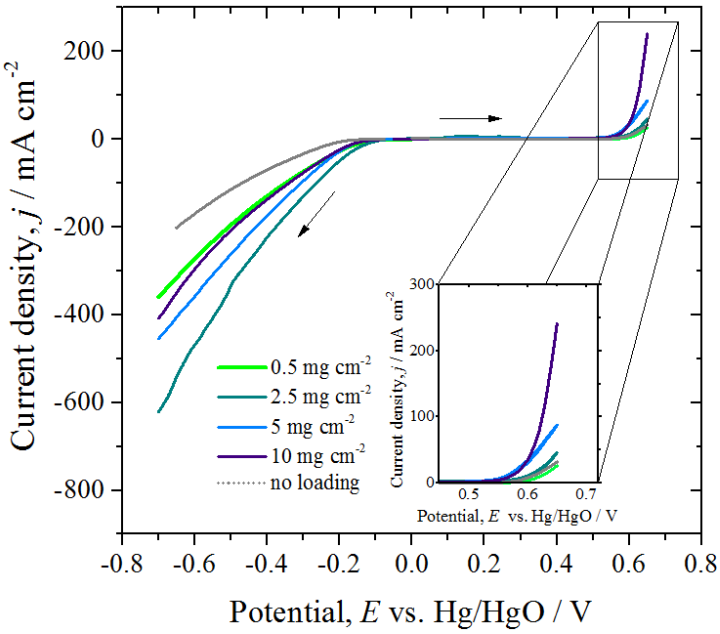


Figure 44. Cycle voltammograms for both the OER and ORR of LSFCO/C at various loadings ranging from 0.5 mg $cm^{-2}$ -10 mg $cm^{-2}$. Pt mesh counter electrode in 6 M KOH Oxygen (99.999%, BOC) supplied at 100 $cm^3$ $min^{-1}$ at a scan rate of 10 mV $s^{-1}$.

The next step was to investigate the performance of these catalyst when they are combined, the best performing formulations are presented in Figure 45,

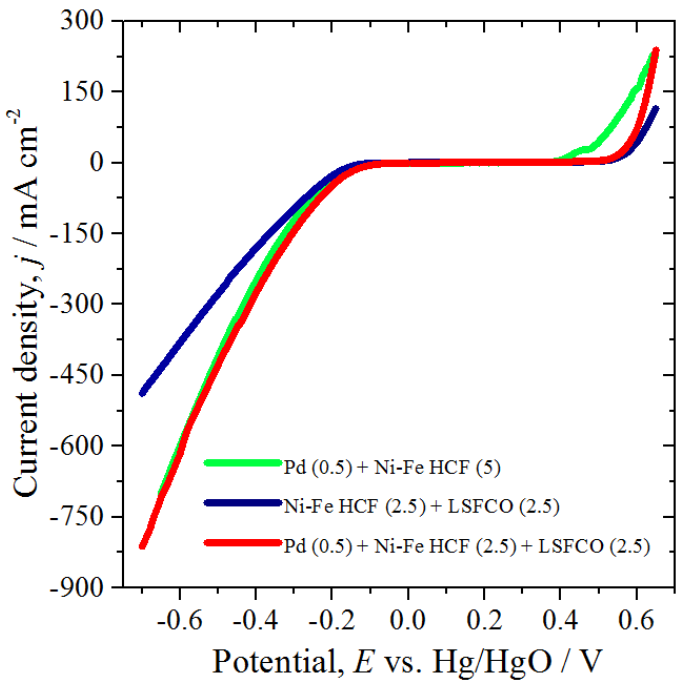


Figure 45. Cycle voltammograms for both the OER and ORR of 3 electro-catalysts combinations. Pt mesh counter electrode in 6 M KOH Oxygen (99.999%, BOC) supplied at 100 $cm^3$ $min^{-1}$ at a scan rate of 10 mV $s^{-1}$.

From this last set of cycling voltammograms it is appreciable that the best performance was achieved with a loading of 0.5 mg $cm^{-2}$ of Pd/C and 2.5 mg $cm^{-2}$ of Ni-Fe HCF and 2.5 mg $cm^{-2}$ LSFCO, followed very closely by the formulation with 0.5 Pd mg $cm^{-2}$ + 5 Ni-Fe HCF $mgcm^{-2}$.

Having this in mind it was decided to further the characterisation of these two formulations by setting up again a 30 min-reduction – 30 min-oxidation at the C/5 protocol for 96 hrs and to compare the measured potentials, these results are presented in Figure 46.

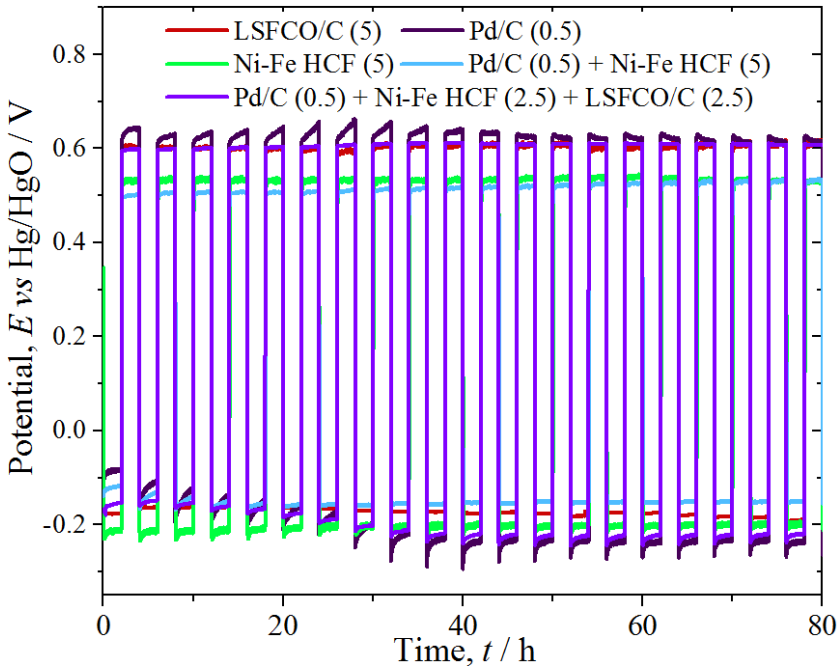


Figure 46. Reduction (30 mins) – oxidation (30 mins) GDE profiles comparison using 5 electro-catalysts at 20 mA $cm^{-2}$ in 6 M KOH, with 100 ml $min^{-1}$ $O_2$ flow into the back of the electrodes.

Finally to compare with our previous results (Figure 40) a reduction-oxidation protocol at various current densities ranging from 40 - 2000 mA $cm^{-2}$ was performed. These results and the comparison with previous ones can be observed in Figure 47.

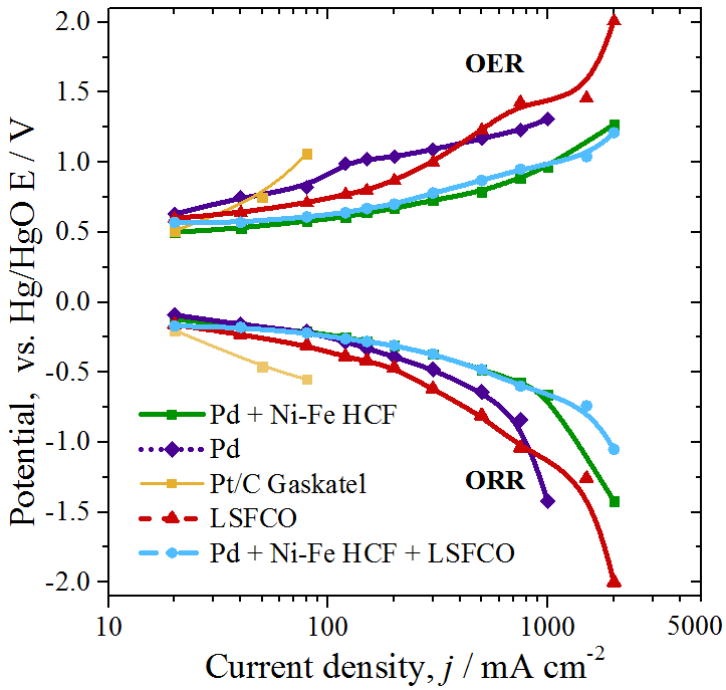


Figure 47. Reduction-oxidation potential as a function of the current density for various GDE formulations.

It is important to know the current density limit of each electrode to determine the maximum power that they can deliver in an IAB configuration as will be described in the chapter 8.

## 6.4 Computer assisted tomography to study the mesoporous structure of the GDE.

Furthering the characterisation of our in-house GDE, additional studies were performed using X-ray tomography. The aim of this study was to gain insight of the morphological and geometrical dimensions of the meso and micro porous structure of the GDE structure. With this technique the maximum resolution that can be achieved will be with a minimum voxel size of *ca.* 100 nm. This technique can provide outstanding three dimensional reconstructions which can enable us to better understand how fast oxygen can diffuse within its structure and to determine mass transport limiting rates or to determine if the catalyst layer is homogenously dispersed. Using this technique in Figure 48 a 3D reconstruction of a section of one of our GDE is presented where the 3 main features are discernible (this technique

identify different areas if they have different densities) from each other: 1) Conductive layer, 2) catalyst layer and 3) the carbon support layer.

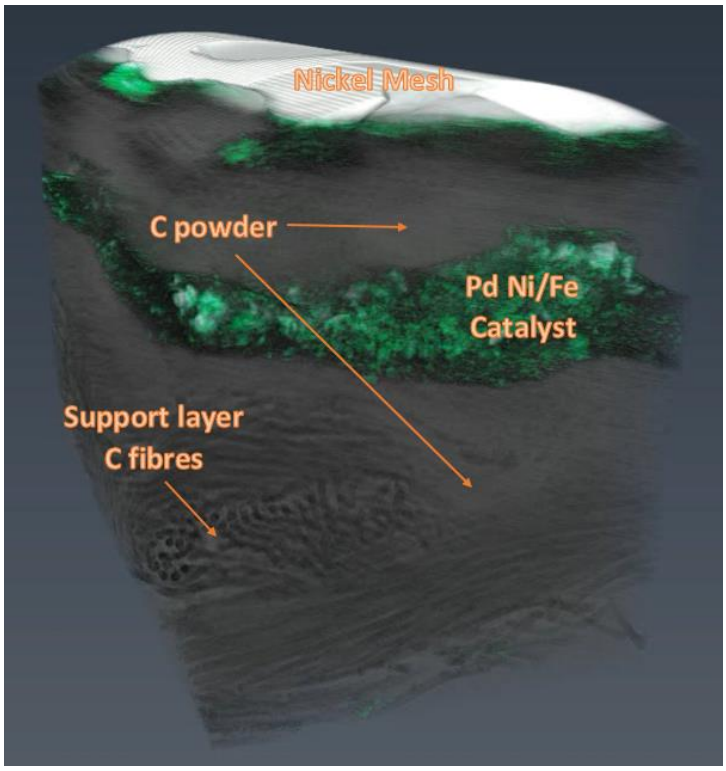


Figure 48. 3D reconstruction from tomography data of a gas diffusion electrode.

To learn about the morphology of the individual catalysts particles other techniques such as scanning electron microscopy (SEM) or transmission electron microscopy (TEM) are required as can be seen in Figure 49, where it is discernible the particle size and if the particles have a discernible crystal geometry up to a certain extent.

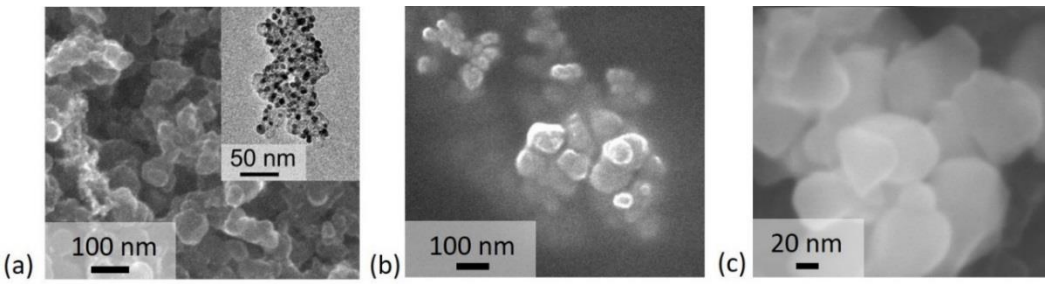


Figure 49. Electron microscope SEM and TEM of a) Pd/C, b) Ni-Fe HCF and c) LSFCO/C electro-catalysts, SEM performed on a 0.5-30 kV JSM 6500F thermal emission SEM and TEM performed using a 300 kV JEOL 3010 TEM on S147-3 copper grids coated with perforated carbon film (Agar Scientific).

## 6.5 Conclusions and further work on the air electrode

Some promising results were originally achieved using the Pd/C catalyst in this type of GDE, as was reported originally in [4]. Among the reported results, a performance-comparison of the bifunctional catalyst showed that it had a superior performance when compared to some commercially available Pt/C GDE from Gaskatel and Johnson Matthey (Figure 14).

Using only one bifunctional catalyst in a GDE would be ideal, nevertheless there are not many bifunctional catalyst with good electrocatalytic activity towards both the OER and ORR. On the other hand electrocatalytic materials with a good electrocatalytic activity toward either the OER or ORR are more abundant. Having this in mind, it was observed that by combining different types of electrocatalytic materials together a synergic effect can be achieved (Figure 36).

Following this line of research the subsequent research on the Pd/C + Ni-Fe HCF produced air electrodes with a better performance than the Pd/C on their own (confirmed by the cyclic voltammetry experiments presented in Figure 36). These electrodes were cycled at what could be considered high current densities for a GDE (>300 mA $cm^{-2}$) for various cycles, without observing some immediately evident deterioration (Figure 38 and Figure 40). Similarly, at a later point over this line of research, this synergic effect was observed when testing the LSFCO perovskite which showed by itself a high electrocatalytic activity towards the ORR (Figure 44) and a good bifunctional activity when combined with the Pd/C and Ni-Fe HCF (Figure 45).

Pd/C seems to provide promising bifunctional electrocatalytic activity towards the OER and ORR, nevertheless is a noble metal reason why implementing this technology would only be possible if the required amount of Pd is minimum, that is why ultra-low loading of this catalyst are used (*ca.* 0.5-5 mg $cm^2$). A quick estimation at the present time of 1 g of Pd show a commercial price of 27 GBP per gram. Loadings of 0.5-10 mg $cm^2$ translate into a cost of 1.35- 27 pences $cm^{-2}$.

The next step was to optimise the loading of the three electrocatalysts trying to determine up to what extend adding more catalyst would have no effect and once knowing this loading to prepare an electrode using the resulting loadings together. Unfortunately there was a limit to the amount of material that can be deposited on the surface of the support material reason why this lead to some compromises. (For

example the desired loading would have been Pd/C, NiFe HCF and LSFCO, but were used instead respectively).

As a result of loading optimisation studies it was found out that a loading of 0.5 mg $cm^2$ of Pd + 2.5 mg $cm^2$ of LSFCO and 2.5 mg $cm^2$ of Ni-Fe HCF have been the best formulation so far, showing the highest current densities at both -0.6 V and 0.6 V vs the Hg/HgO, which corresponds to the ORR and the OER respectively (Figure 45).

In the future it will be possible to continue this line of research by testing novel bifunctional catalyst and its combinations, it would be as well very interesting to develop novel techniques to deposit the catalyst layer more homogenously and to compare the performance with the electrodes that had been reported as result of this research. It has been suggested that research of GDE of this type could benefit from researching the optimum C/PTFE ratio used in the hydrophobic layer of these types of electrodes.

Finally in the future it would be interesting to develop a mathematical model of the oxygen diffusion within the structure of GDE, for this purpose the information obtained from the X-ray tomography studies would be useful and would lead to the optimisation of the gas diffusion layer in this type of electrodes.

Finally the reader is encouraged to revise the following publications since many of the results presented in this chapter later were further analysed and discussed in them. [5,6]

# Chapter 7: Engineering design of an IAB

In this chapter the focus is placed on the engineering design of the IAB laboratory cells. In this chapter the various prototypes that were developed and used to test the iron and air electrodes in a battery configuration that later allowed the development of a whole battery stack and to scale up the cell will be described.

## 7.1 The importance of cell design

The engineering of the electrodes and the research aiming to improve its performance are the most crucial aspects related to the development of a battery. Nevertheless, these elements must be orchestrated with other components in a final battery stack that may consist of tens or hundreds of cells, together with other systems such as: a battery management system, an electrolyte flowing system, air pumps, electrode connections, safety fuses, and other potential elements. The engineering design of the battery consider all these complexities when aiming to develop a prototype for a particular application.

Engineering design is a complex activity involving the use of scientific principles, technical information and imagination to meet a specific solution. It is usually an iterative process involving going back to old ideas until the best solution is achieved.

Engineering design incorporate broadly speaking at least four main phases:

1. Analysis of the problem to outline the product design specifications.
2. Fast sketch to explore different conceptual designs.
3. Schematic design that may lead to some preliminary prototypes.
4. After an iterative process, a detailed design of the successful prototype is improved.

Traditionally battery prototypes are constructed in a one by one basis due to the large number of part involved, this manufacturing process is usually labour intensive and requires skilled workshop techniques such as cutting, milling and drilling. Besides subsequent redesign are required with are tedious and costly in

terms of labour, time and materials [95]. In this sense, the use of novel fast manufacturing techniques is advantageous.

The ability to respond quickly to the modification in the designs and to quickly adapt to the new demands of a competitive market is crucial to the design and manufacture companies. This ability to become an agile manufacturer must be reached without compromising the profits, innovation and quality. Given this interest, numerous studies and research are carried out in order to develop new fast prototyping (FP) techniques.

The most highlighted fast prototyping techniques in recent years have been: (1) stereo lithography, (2) laser-sintering, (3) fused deposition, (4) laser engineered net shaping, (5) 3D micro welding and (6) 3D printing [96].

Some of the advantages of 3D printing technologies over other FP techniques are: the availability of superior materials, the cost, the speed and the fact that it does not require a support structure. For all these reasons 3D printing has emerged in recent years as a competitive time and resource saving manufacturing process that allows the engineering design process to rapidly advance from a computer assisted model to a manufactured prototype in mater of hours. Given these advantages it is understandable why additive manufacturing, is driving major innovations in many areas such as engineering, manufacturing, art, education, and medicine [97].

## 7.2 Engineering design of the IAB battery cell

In a first instance, it was intended to use a modified flow-cell to test the IAB system, following this line of research it was of interest to characterise the current-density-distribution of this flow-cell under various flow regimes, this study has been detailed in [3], the details of this cell are presented in Appendix A.

At that time, it was not foreseen that due to the hydrogen and oxygen evolution during the charge and discharge processes of the battery, gas bubbles were formed inside the cell rendering the electrodes dry, which resulted in a poor battery performance. That is why a redesign of the battery cell was required with the following product design specifications:

1. It should allow the correct placement of a 50 mm × 50 mm iron electrode in parallel with two-air electrodes.
2. The whole iron electrode should be completely immersed in a KOH 6 M solution and only one face of the air electrodes must be in contact with the electrolyte.
3. The other side of each of the air-electrodes must be open to the air, or must allow a way to supply air/oxygen using a pump.
4. The components must be chemically compatible with the strong alkaline media KOH 6 M.
5. The system must be leak proof or provide a way to deal with leaks during the operation.
6. The cell design should consider that during charge or discharge gas will be evolved and therefore the design should provide a way for venting the gas and facilitate its removal from the electrode surface.
7. It should also provide a way to electrically connect the electrodes so they can be connected to the potentiostat during tests.
8. It should considered the possibility to connect two air electrodes per each iron electrode if needed.
9. The design should consider that many cells may be connected together in the future, so the possibility that the cells must be designed to be stackable must be considered.
10. The lighter and more compact the battery would be better to increase the gravimetric and volumetric energy and power densities.
11. Use environmentally friendly materials whenever is possible, or to consider as well the recyclability of the materials used in this design.

## 7.3 IAB preliminary designs

Once the product detailed specifications were outlined, a few solutions were sketched using a CAD software in this case Autodesk Inventor 2015. Some of the first models that were designed during this phase are show in this section.

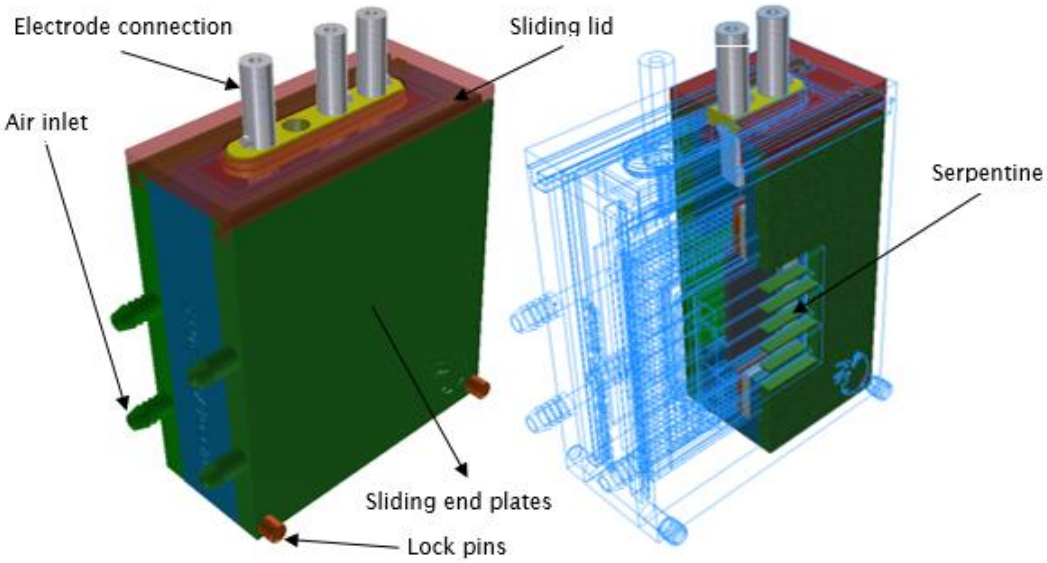


Figure 50. Conceptual design No 1. 3D CAD model.

The idea behind the design in Figure 50 was to avoid the use of screws. The compression required to seal the electrolyte were applied using a sliding plate to compress the gaskets. Unfortunately, this design apply considerable stress onto the air electrodes during the assembly and tend to damage them.

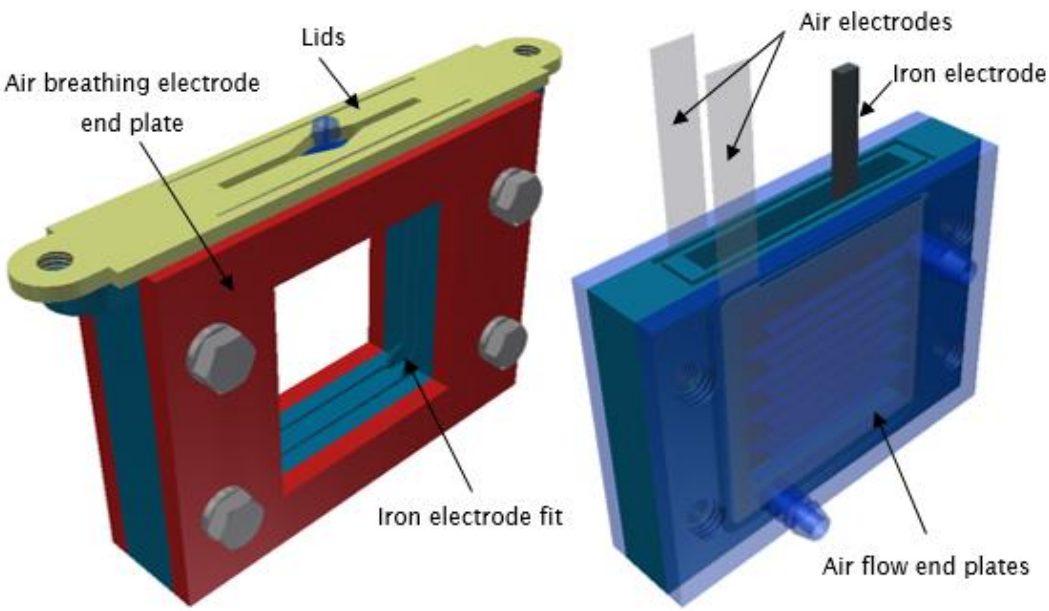


Figure 51. Conceptual designs No. 2 and No. 3.

Given the fact that the air electrodes were damaged with the previous cell designs a different approach using compression end plates were followed, as shown in Figure 51. On the left side an open window to try out the air electrodes as breathable

ones and on the right side of Figure 51 using a thin end plate to supply oxygen-air to the air electrodes.

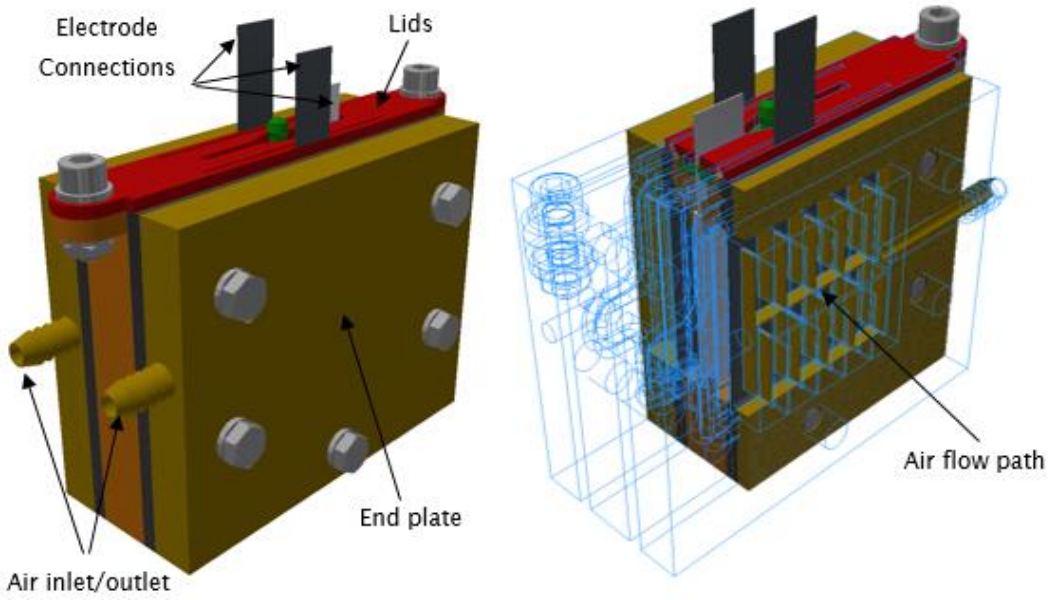


Figure 52. Conceptual design No.4. For this design consideration to allow the air to flow in a serpentine structure were maintained. The thickness of the end plates was increased to avoid the bending of these parts when it is under compression.

Each one of the previous designs provide insight of what can be improved. It was noted that avoiding leaks on the edges of the air electrode was not that straightforward since the air electrode was easily damaged when compressed in excess (subject to high sheer stress). Furthermore, the edges of the air electrode are not smooth but coarse. The most successful solution is the inclusion of sealing lumps at the edges of the cell window to increase the normal stress around these edges. Instead of leaving the surface completely flat, a “Gaussian-shaped” lump around the air electrode window helps to increase the compression of the gaskets around this area. This conceptual design called prototype 5 is shown in Figure 52 and a more compact option in Figure 53.

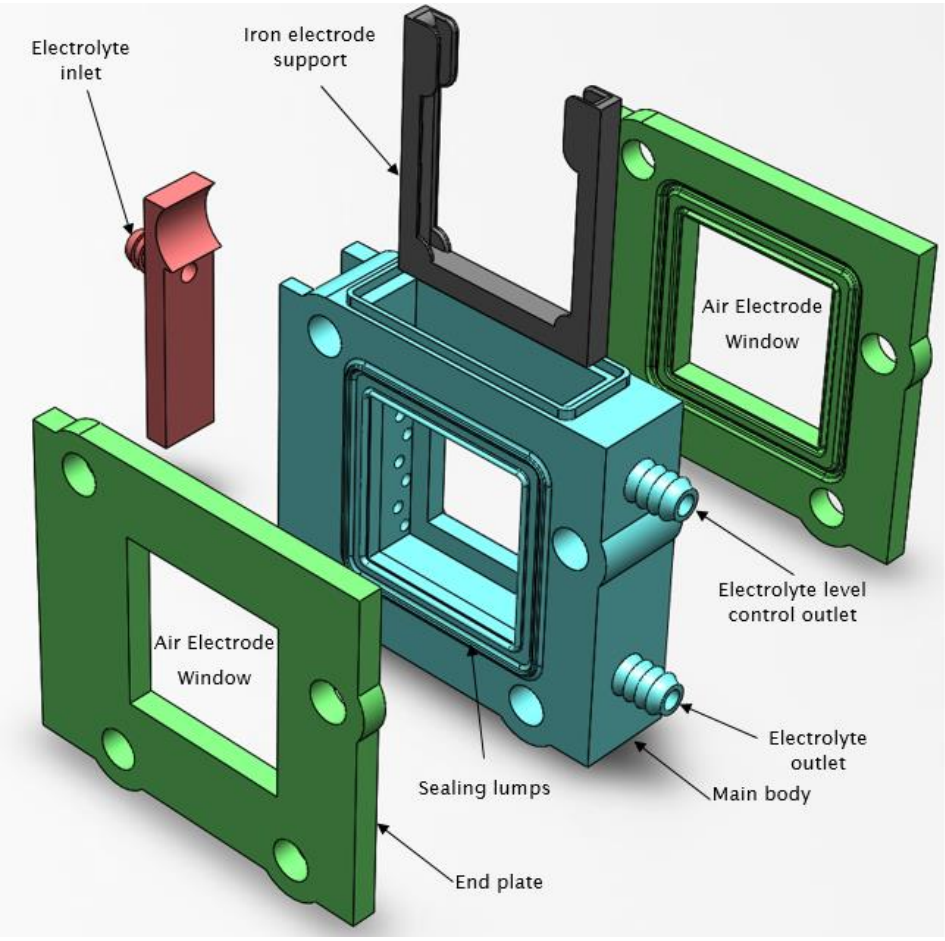


Figure 53. This cell is a flow cell to ensure that the electrolyte level is always enough to avoid leaving the electrodes dry during operation. This model has not yet been 3D printed or tested.

## 7.4 3D printing the laboratory prototypes

There are many types of 3D printers; the simplest ones have a nozzle that heat up the material up to its melting temperature, in the case of ABS *ca.* 270-300 º C.

Depending on the size and density selection, the part will experience temperature stresses that may deform the part in small amounts while cooling down. If the deformation due to thermal stresses is not relevant, a simple 3D printer can be used. Nevertheless, due to the size of the cell and the required density and finishing a 3D printer with a controlled temperature chamber is required to minimize these deformations. The “Dimensions 1200es” manufactured by Stratasys shown in Figure 54 have a temperature controlled chamber at 80 ºC and was very convenient to manufacture different cell prototypes.

In order to print a 3D model, the file is exported as a .SLT file that can be read with any 3D printing software. A complete cell with all its parts typically required eight hrs to be manufactured.

Figure 54. 3D printer "Dimensions 1200es"

## 7.5 Final design for the IAB laboratory cell

After 3D printing and testing out prototype 4 a modification to the end plates was carried out in order to include an oxygen/air flow supply. Since the previous design had a small leak, a 5$^{th}$ screw was added to compress the end plates more evenly. Figure 55, Figure 56 and Figure 57 show the general characteristics of prototype 5.

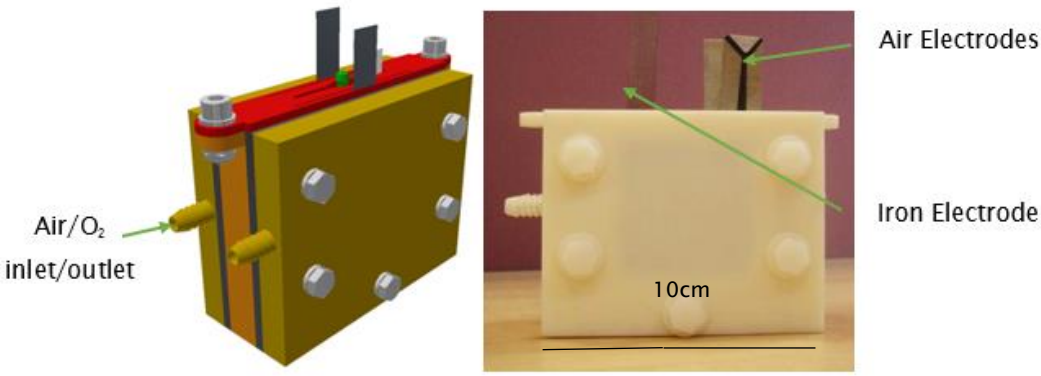


Figure 55. Prototype 5. Left. 3D CAD model assembly, Right. 3D printed cell assembled with all its components, weight 350 g, overall height = 9 cm, overall width 11.0 cm overall thickness = 3.9 cm. Electrode area 25 cm$^2$.

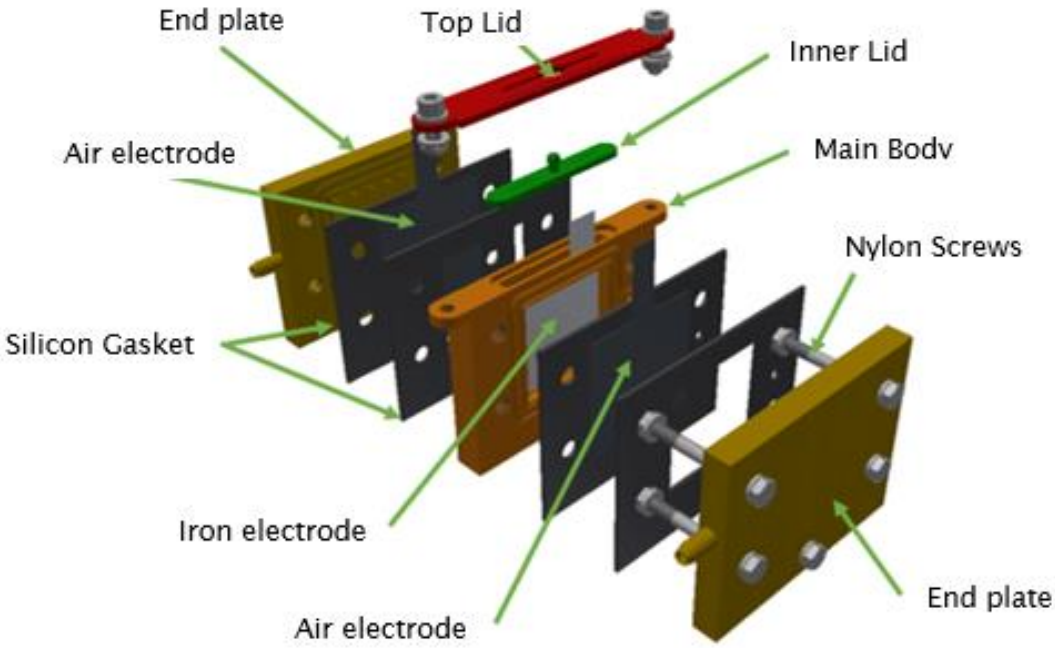


Figure 56. Prototype-5 exploded view. List of parts: 2 end plates, 4 silicon gaskets, 2 air electrodes, 1 iron electrodes, 1 main body, 1 inner lid, 1 top lid, 5 nylon screws.

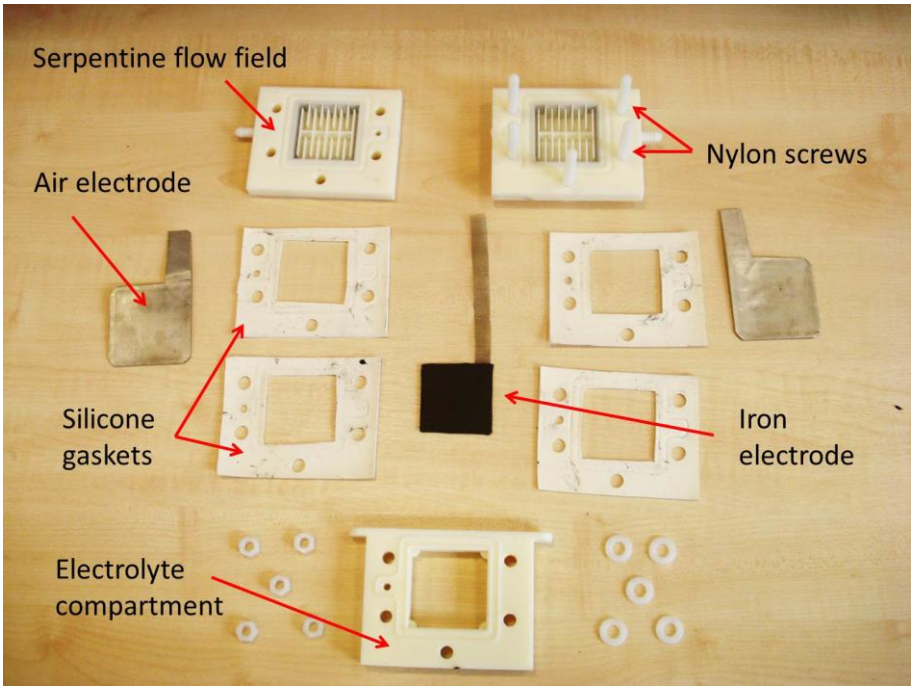


Figure 57. Prototype 5 disassembled. List of parts: 2 end plates, 4 silicon gaskets, 2 air electrodes, 1 iron electrodes, 1 electrolyte compartment body, 1 inner lid, 1 top lid, 5 nylon screws.

## 7.6 Design of an iron air battery stack

The next step after designing prototype 5, the possibility to design an IAB stack was investigated. The cell stack was designed using the previous prototype 5 design and by adding intermediate plates to direct the airflow to the air electrodes. Figure 58 shows the CAD prototype of the cell stack. This design was still considering the possibility of using two air electrodes per iron electrode since it was manufactured before discovering it was better to only use one air electrode per iron electrode.

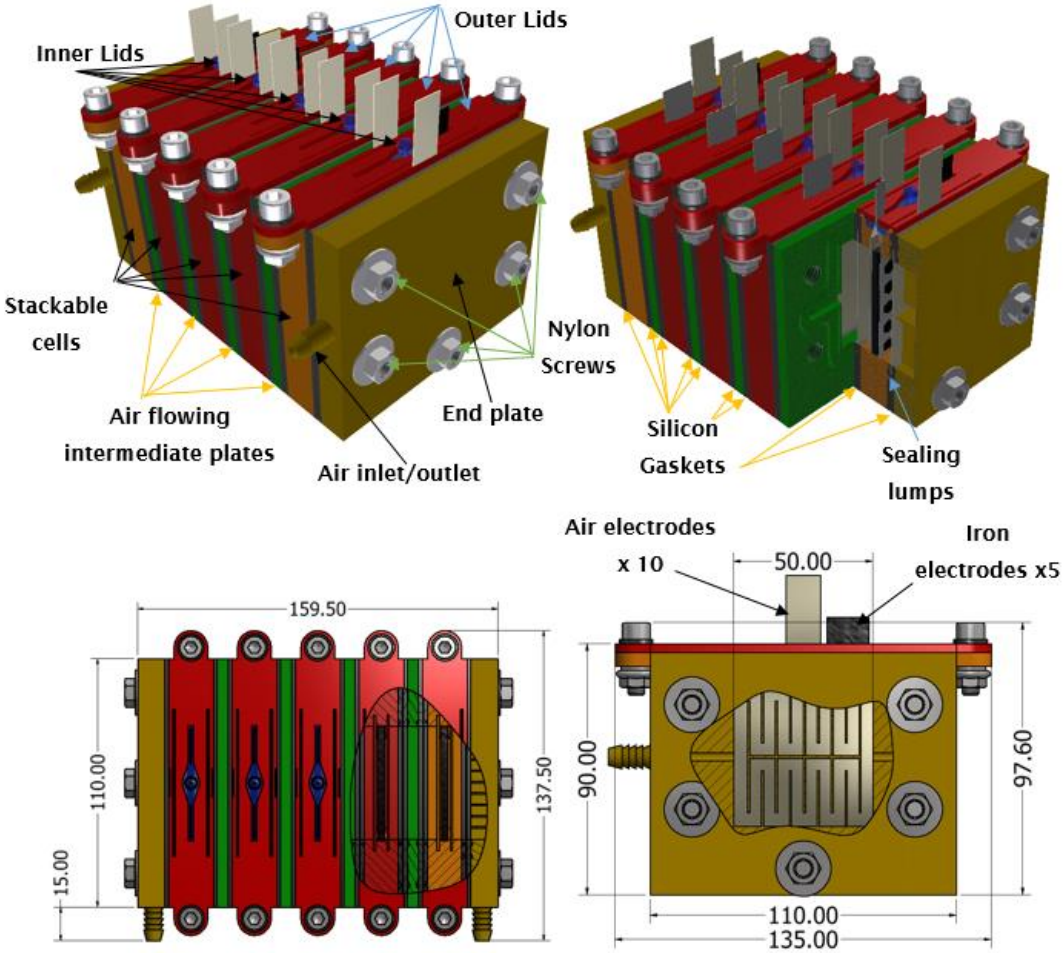


Figure 58. Iron air battery 5 cell stack CAD design done in Autodesk Inventor 2015. Units are in mm.

This design was 3D printed in ABS using a “Dimensions 1200es” manufactured by Stratasys, this 3d printer have a temperature controlled chamber that allow us to diminish the thermal stress of the parts therefore the bending during cool down is minimal. The final iron air battery stack with their respective iron and air electrodes is shown in Figure 60.

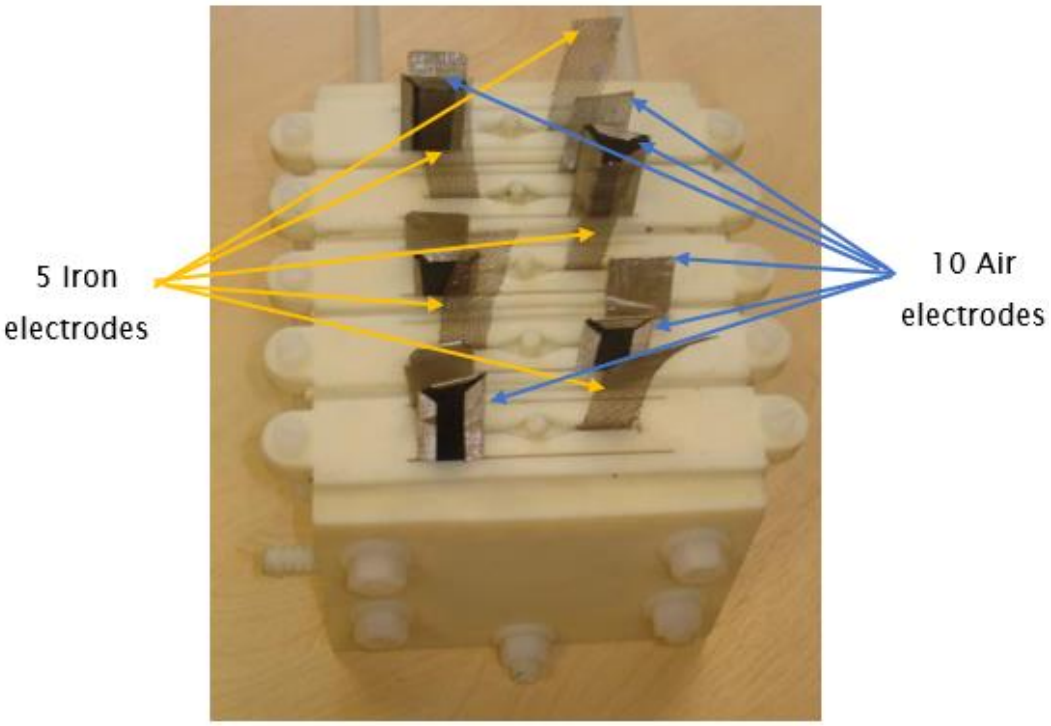


Figure 59. 3D printed IAB 5 cell stack.

As part of the NECOBAUT collaboration, other partner focused on the development of an outer shield. The outer case provides a robust cell prototype where the 3D printed stack can be placed inside as is shown in Figure 60.

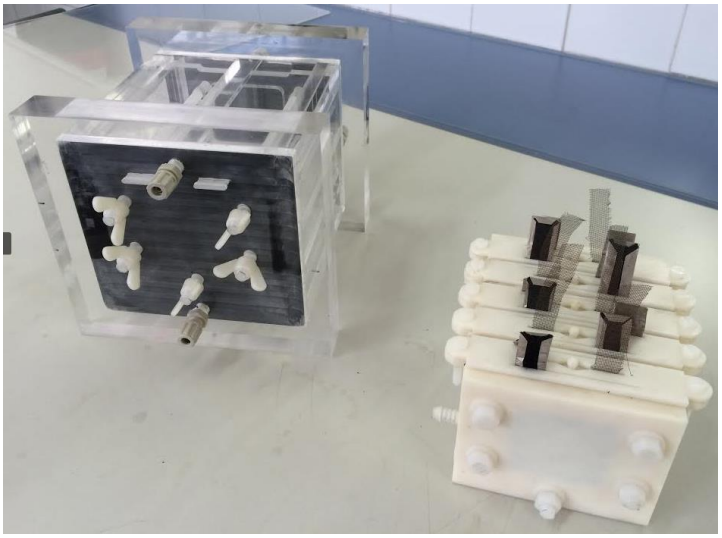

Figure 60. IAB 5-cells-stack 3D printed at UoS (right) and the outer protective case manufactured by Tecnicas Reunidas (left).

## 7.7 Scaling up the cell (200 $cm^2$ electrodes)

The final design requirement was to scale up the cell components, trying to bring the electrodes up from 25 $cm^2$ to 200 $cm^2$, for this purpose a similar design as prototype 5 was used but with larger frames. In Figure 61 and Figure 62 the CAD model and the 3D printed components for the large IAB cell are presented. For comparison purposes the 25 $cm^2$ cells the small's ones, and the stack are presented in the same picture.

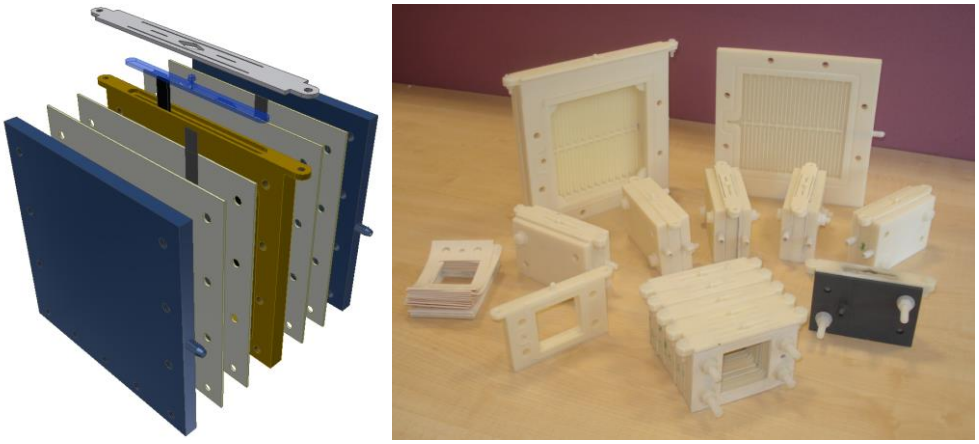

Figure 61. Large IAB cell design. Cell dimensions: overall height = 215 mm, Overall width = 147 mm, Overall thickness = 47 mm, Electrode area = 200 $cm^2$.

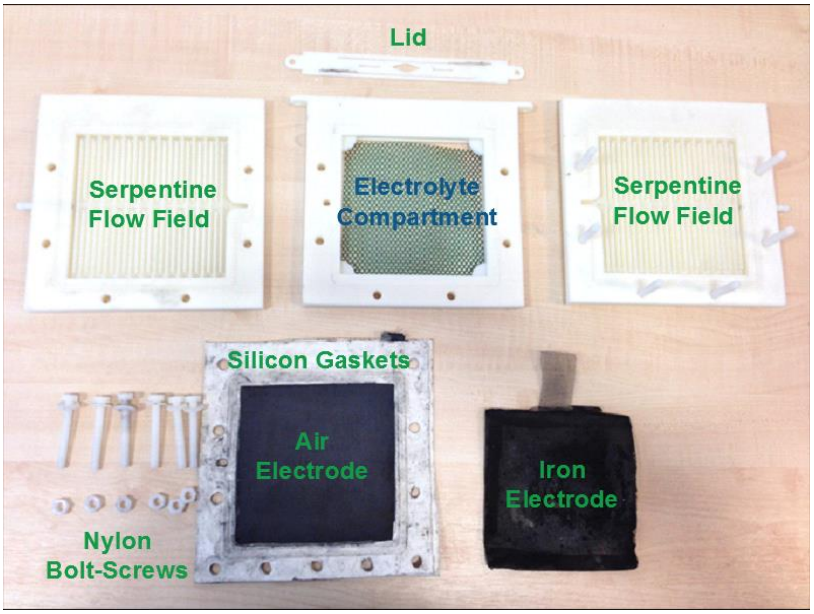


Figure 62. Large house-made IAB cell components.

# Chapter 8: Iron air battery performance and characterisation results

This chapter will focus on the experimental results of the different IAB prototypes that were tested during this Ph.D. research. It follows mostly a chronological order specially the first three sections where the results and knowledge gained from each prototype helped to improve the following one, until prototype-5 was developed and further electrochemical characterisation was performed using this laboratory prototype. The final sections will report the main results associated to the IAB stack and the various challenges that were encountered when scaling up the IAB in the 200 $cm^2$ cell. It would be advisable to the reader to refer to [7], since many of the results presented in this chapter were used later to prepare this publication.

## 8.1 Prototype 1. IAB flow cell

The first prototype was developed by the NECOBAUT collaboration and it is presented in Figure 63 and described in detail in Appendix A. It consist of a flow cell design using the iron electrode manufactured by TECNALIA and one air electrode enhanced with the Pd/C catalyst supplied by CNR-ITAE.

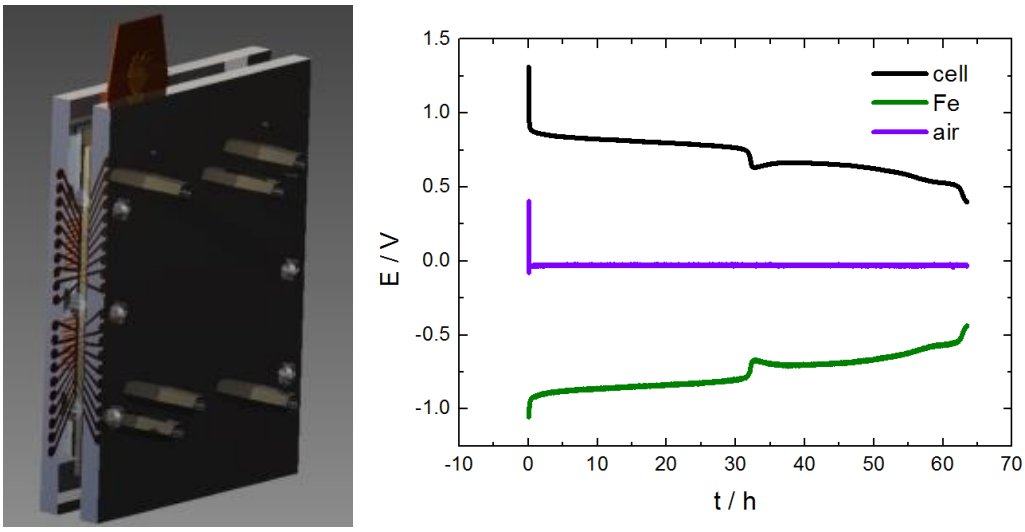


Figure 63. Left: first IAB flow cell prototype. Right: Discharge curve of IAB prototype iron electrode and improved air electrode (30% Pd-Vulcan with Ni mesh) at 1 mA $cm^{-2}$, with oxygen and electrolyte flow rates at 50 $cm^3$ $min^{-1}$. The individual electrode potentials were measured against an Hg/HgO (1M KOH) reference electrode. The average cell

voltage for the first discharge plateau was 0.82 V, and the total energy density was 451 W h $kg^{-1}_{Fe}$ at only 1 mA $cm^{-2}$, flow rate 5 $dm^3$ $min^{-1}$.

Many problems related to the entrapment of gas bubbles in the main chamber that lead to a poor battery performance were observed and it was not possible to measure a good charge-discharge profile at higher current densities than 1 mA $cm^{-2}$. In fact the discharge profile shown in Figure 63 was the only one that was acceptable and it was obtained at a very low current density, it was after many attempts that it was discovered that the gas bubbles that were formed during the charging process were trapped inside the main chamber and were rendering part of the electrode dry, reason why, it was not possible to obtain consistent results consecutively, for this reason the need to redesign the cell as was explained in the previous chapter.

## 8.2 Prototype 2. IAB static-bipolar-1cm inter-electrode gap cell

For the new cell design, given the problems using an enclosed chamber flow cell it was suggested to use a simpler static cell. The design suggestions included: (1) to make the cell with one iron electrode and two air electrodes, (2) to consider the management of the gas evolution during the charge and discharge cycles and (3) to include the possibility to use an additional nickel electrode during charge.

It was suggested that a more easily assembled battery could be useful in order to facilitate the setup of the experiments. This design featured a set of rails where the components were able to slide until reaching its final position.

Considering the proposed restrains and suggestions, prototype 2 was developed and 3D-printed as shown in Figure 64 together with the best charge-discharge profile obtained using this prototype. The assembly of this cell included as active materials one $Fe_2O_3$/C iron electrode manufactured by TECNALIA and two GDE with the Pd/C catalyst supplied by CNR-ITAE.

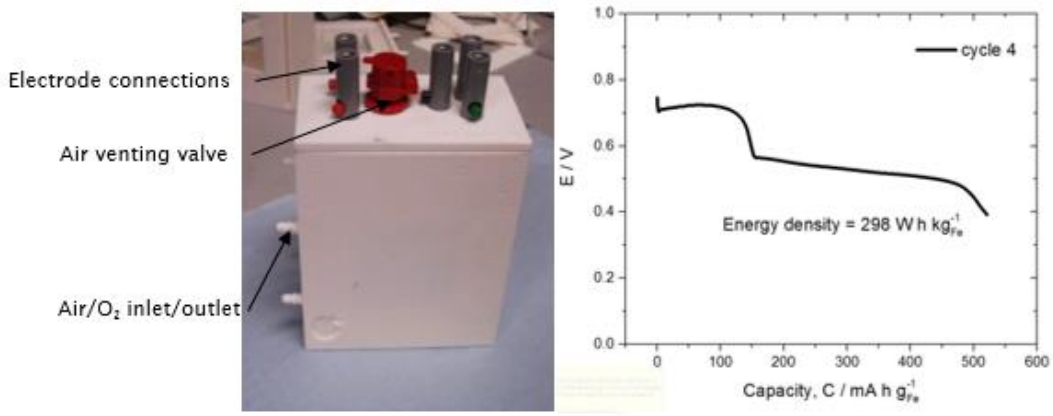


Figure 64. Left: Photograph of prototype-2 inter-electrode gap 1 cm. Right: Discharge profile for the best cycle at 10 mA $cm^{-2}$. The electrolyte was 6 M KOH and oxygen was flowed into the cell at a rate of 100 $cm^3$ $min^{-1}$.

The comparison of this prototype with the test obtained previously (Figure 63) shows that prototype 2 can be cycled at higher current densities since this design allows the oxygen bubbles to escape and the iron electrode was always wet during operation. With this cell, the energy density was 298 W h $kg^{-1}_{Fe}$ at 10 mA $cm^{-2}$, which was 10 times higher that with the previous results.

Unfortunately, prototype 2 was unreliable due to leaks and the individual electrode potentials could not be measured continuously since the air electrodes flooded after a few hrs of operation compromising its performance.

## 8.3 Prototype 3. Improved IAB screw less static design

By removing the space for the auxiliary electrodes a more compact design was developed. The inter-electrode gap was reduced to 6 mm, as shown on Figure 65. Using the same type of iron and air electrodes as in the previous experiments, the charge-discharge performance of the cell improved and the best one is presented in Figure 65.

Figure 65. Left. 3D-model of prototype-3, Middle. 3D-printed prototype-3, Right. Top view of the cell interior. Inter-electrode gap 64 mm.

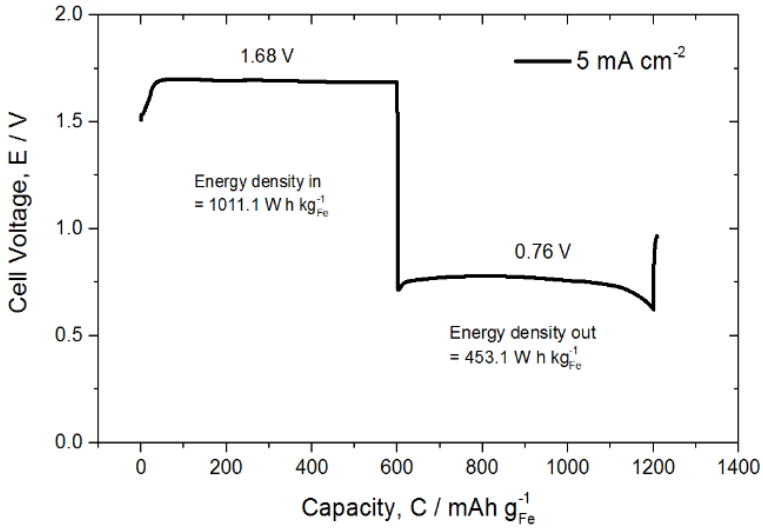


Figure 66. Discharge profile for the best cycle at 5 mA $cm^{-2}$ in prototype 3. The electrolyte was 6 M KOH and oxygen was flowed into the cell at a rate of 100 $cm^3$ $min^{-1}$.

In this case as can be seen in Figure 66, it was possible to achieve 453 W h $kg^{-1}_{Fe}$ at 5 mA $cm^{-2}$ without forcing air/oxygen supply through the air electrodes, the energy efficiency taken as the ratio of the energy output and the energy input was 44.8%, the voltage efficiency taken as the ratio of the output and input voltage was 45%.

## 8.4 Prototype 4. IAB static-design open cell

The test performed in prototype 3 (Figure 65, 453 W h $kg^{-1}_{Fe}$ at 5 mA $cm^{-2}$) were more satisfactory than the two previous ones (298 W h $kg^{-1}_{Fe}$ at 10 mA $cm^{-2}$ in

prototype 2 and 451 W h $kg^{-1}$ at 1 mA $cm^{-2}$ in prototype 1), but still some crucial problems with the screw-less design needed to be improved.

It was noticed that considerable shear stress was placed upon the air electrodes damaging them by detaching the carbon layer from the nickel mesh and the electrolyte leaks were difficult to manage at the border between the junction of the air electrode and the air chamber. Furthermore, the cell by itself had to be bulky since ABS is not as rigid as other materials so a relatively thick layer (5mm) of material was needed in order to support the inner stress of the gaskets to seal the leaks.

Overall, the advantages of having no screws were small compared with the additional complications in the design and testing. That is why a new design was suggested. In this case, a simple electrolyte chamber and two frames form the air electrode were employed and tightened with screws and bolts as shown in Figure 67., the inter electrode gap was keep at 6 mm.

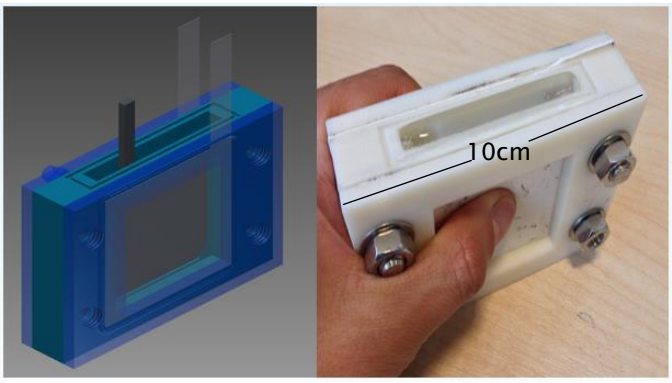


Figure 67. Static open cell design. In this cell the inter electrode gap was 6 mm.

When this cell was tested in a 3-electrode configuration, the following charge-discharge profile was obtained (Figure 68). In this cell, 427 W h $kg^{-1}_{Fe}$ at 10 mA $cm^{-2}$ was achieved; the electrolyte, iron and air electrodes were the same as in previous configurations.

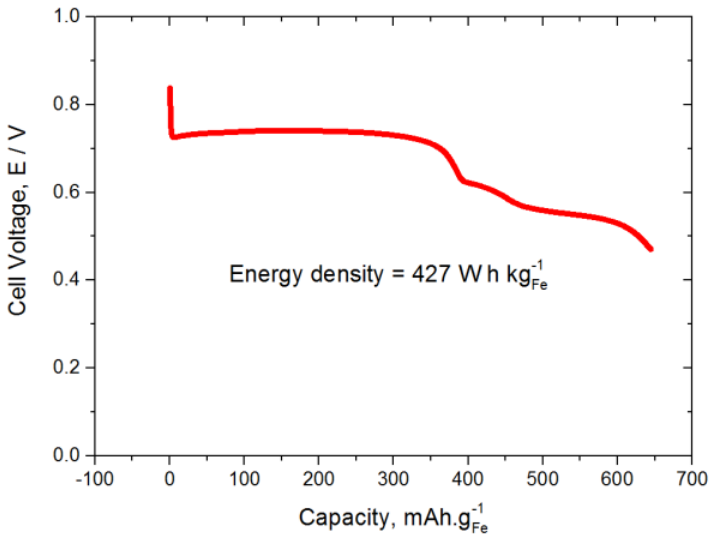


Figure 68. Discharge profile obtained with prototype 4 at 10 mA cm$^{-2}$. The iron electrode was the improved iron electrode sent by TECNALIA, and the air electrodes were the improved air electrodes catalysed with the 30% Pd/C developed by CNR-ITAE

## 8.5 Charge-discharge of prototype-5 supplying $O_2$

Using prototype-5, the same type of iron and air electrodes and electrolyte as before, the charge-discharge profiles at 5 and 10 mA cm$^{-2}$, were measured but in this time while $O_2$ with a purity of 99.99% was being supplied at a rate of 100 ml min$^{-1}$ in the gas diffusion side of the air electrodes. These results are presented in Figure 69 and Table 12.

In this experiment two more voltammeter were used to monitor the individual electrode potentials *vs* the Hg/HgO reference electrode simultaneously. These potential are also presented in Figure 69, the green line represent the air-electrode half-cell potential and in cyan the half-cell potential of the iron electrode. The indigo plot is the whole cell potential.

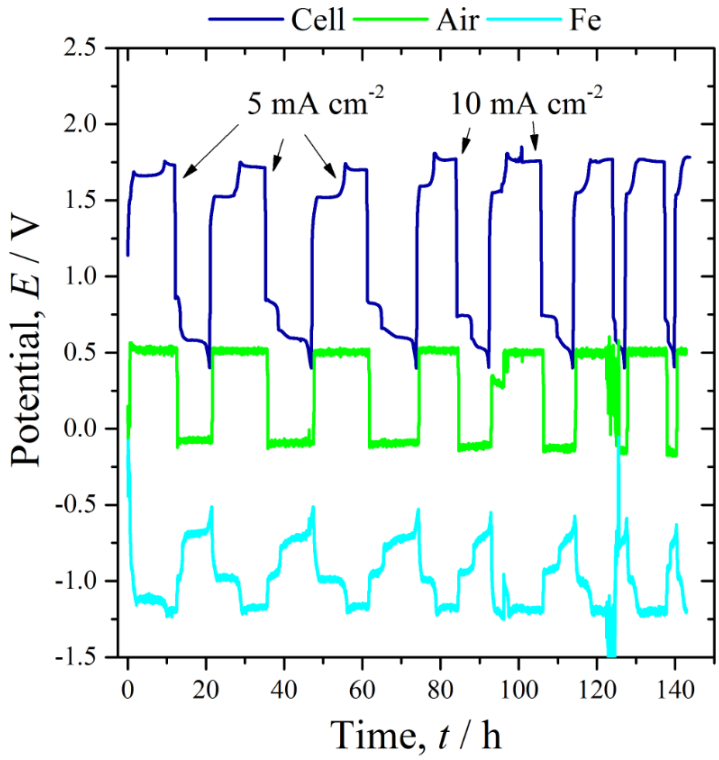


Figure 69. Cycling of prototype 5 filled with 6 M KOH, and 100 ml $min^{-1}$ oxygen flow into the back of the air electrodes. The air electrodes were catalysed with 30 wt. % Pd/C developed by CNR-ITAE. Potential is *vs* the Hg/HgO ref electrode.

Table 12. Cell performance data for the first seven cycles of cell 3.

| **Cycle** | **Current Density / mA $cm^{-2}$** | **Capacity / mAh-$g^{-1}_{Fe}$** | **Energy density / $Whkg^{-1}_{Fe}$** | **Cell Voltage (for both plateaus) / V** | **Voltage Efficiency / % (1st discharge plateau only)** | **Faradaic Efficiency / %** | **Energy Efficiency / %** |
|---|---|---|---|---|---|---|---|
| 1 | 5 | 469 | 303 | 0.84,0.59 | 50 | 78 | 47 |
| 2 | 5 | 585 | 377 | 0.83, 0.59 | 58 | 84 | 51 |
| 3 | 5 | 655 | 429 | 0.82. 0.60 | 49 | 78 | 59 |
| 4 | 10 | 820 | 555 | 0.74, 0.54 | 42 | 82 | 33 |
| 5 | 10 | 840 | 584 | 0.74, 0.54 | 42 | 84 | 26 |
| 6 | 10 | 310 | 235 | 0.69, 0.55 | 39 | 31 | 18 |
| 7 | 10 | 270 | 184 | 0.70, 0.54 | 39 | 27 | 16 |

The iron electrode contained approximately 2.5 g of iron, the theoretical specific capacity of iron is 960 mA h $g^{-1}_{Fe}$, for the first plateau this means that in principle

the maximum capacity of the electrode is 2400 mA h associated to the first discharge plateau.

During this test the iron electrode performed remarkably well during some cycles, for example in cycle 5 the capacity was 840 mA h $g^{-1}_{Fe}$ approximately 87 % of the theoretical maximum. Unfortunately, this good performance was not maintained in the following cycles where a drastic drop to 310 mA h $g^{-1}_{Fe}$ was observed.

In terms of energy density in some cycles high values as 584 W h $kg^{-1}_{Fe}$ were achieved, this value is high when compared with other batteries for example, the theoretical energy density of a Lithium cobalt oxide battery (Li-ion battery) is 568 W h $kg^{-1}$ [15].

## 8.6 Continuous charge-discharge cycling and air supply prototype 5

To compare how much the performance of the battery (using prototype 5) will vary by substituting $O_2$ with air, an air pump was used to supply air at a rate of 1 $dm^3$ $min^{-1}$ to the gas diffusion side of the air electrodes. The performance of the cell at various current densities ranging from 5 to 25 mA $cm^{-2}$ were studied. These results are presented in Figure 70.

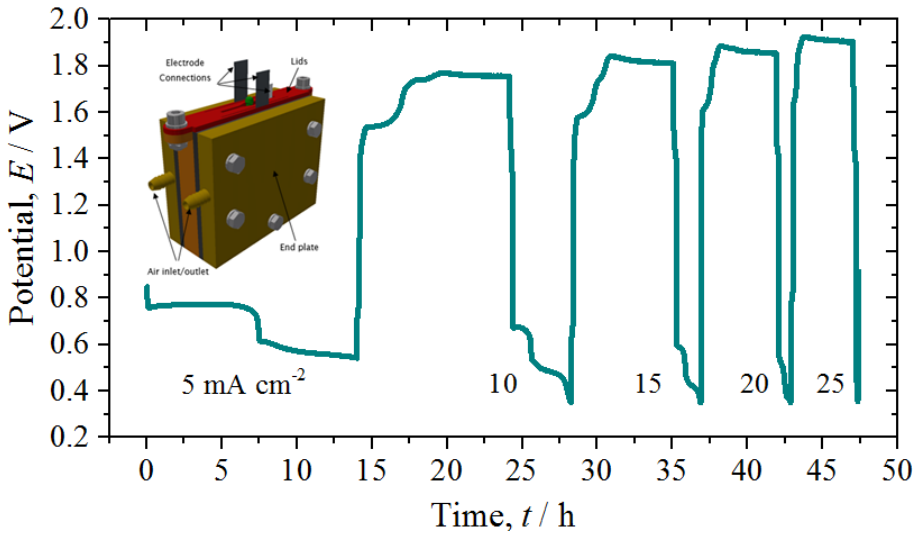


Figure 70. Charge-discharge cycling of prototype 5 with air suply into the back of the air electrodes at 1 $dm^3$ $min^{-1}$ and a gradual increase in cycling current density (both charge and discharge) in the range from 5-25 mA $cm^{-2}$.

In this figure the iron electrode was already charged from a previous test therefore the experiment started with the discharge at 5 mA $cm^{-2}$, then the charge-discharge cycles at 10, 15, 20 and 25 mA $cm^{-2}$ were measured and presented in Figure 70.

It has been mentioned that one of the limiting factors in the life cycle of an IAB was that the air electrode deteriorates over continuous cycling. This deterioration would be faster if cycled at high current densities. Therefore, it was suggested that having two air electrodes per iron electrode could be a way to diminish the current density experienced by each air electrode by half and extend its life-cycle.

Nevertheless, when the iron electrode was cycled with two air electrodes is compared with the case where it was cycled against 1-nickel counter electrode outside prototype 5, it was observed that the performance were different. The iron electrode deteriorated faster inside the prototype 5 with a reduced capacity in each cycle.

After ruling out that, the ABS of the cell could have an effect and a potential poisoning of the iron electrode by something else it was concluded that the main difference was the counter electrode. It can be due the use of one or two counter electrodes. In any case, it was decided to test if by using only one air electrode this might have an effect of the overall performance.

## 8.7 Charge discharge profiles only 1 air electrode prototype 5

In order to determine if the use of one or two air electrodes was having any effect in the performance of the battery the previous experiment in prototype-3 was repeated using now only 1 air electrode. In this case the charge-discharge procedure was planned in such a way that will charge the cell at 10 mA $cm^{-2}$, and then will discharge at different current densities ranging from 5 mA $cm^{-2}$ to 25 mA $cm^{-2}$ in increments of 5 mA $cm^{-2}$, the electrolyte was KOH 6M, and air was supplied to the back of the air electrode at 1 $dm^3$ $min^{-1}$, the reference electrode was as in the previous experiments the Hg/HgO.

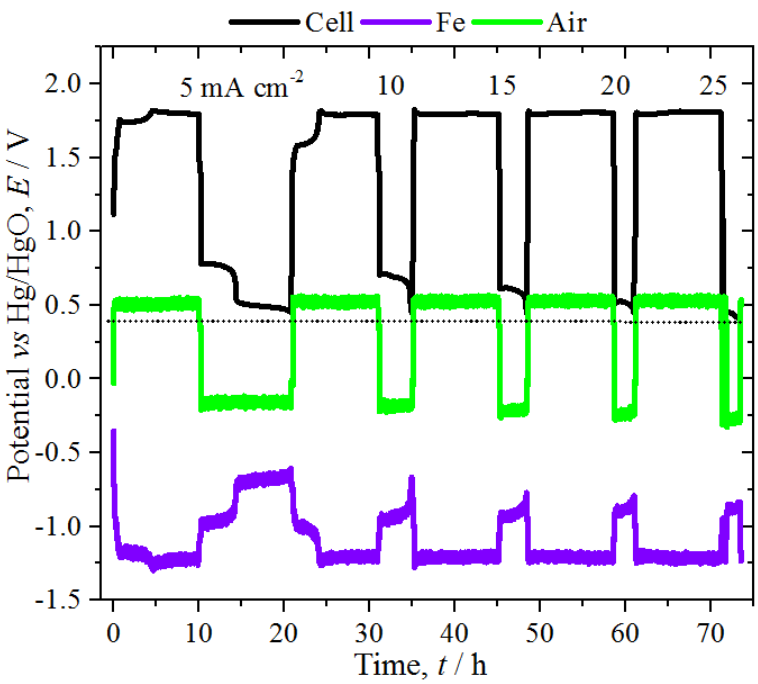


Figure 71. Charge-discharge curves of prototype 5 with only one air electrode at different current densities, the iron and air individual half-cell potentials are refered to the Hg/HgO reference electrode. The dotted line refers to the cut-off potential of 0.45 V.

The performance of the battery in this instance was more consistent in the sense that the iron electrode discharge profile did not drop over continuous cycling but still perform in a similar way. For some reason it seems that if only one counter electrode rather than two per each iron electrode were used the performance of the battery was steadier, so it was decided to continue with this configuration for the following experiments.

During this experiment a cut off voltage of 0.45 V was keep and this did not allow to fully observe the discharge plateaux at higher current densities as it is appreciable in Figure 71. In order to fully observe the discharge capacity at higher current densities it was required to modify the cut-off-potential depending on the discharge current density.

## 8.8 Effect of current density on the discharge capacity

The same experimental set up as used in section 0 was repeated (*negative electrode*: Tecnalia $Fe_2O_3$/C electrode, *positive electrode*: air electrode, *electrolyte*: KOH 6M, *reference electrode*: Hg/HgO, air supply: 1dm$^3$ min$^{-1}$ t*echnique*: Galvanostatic charge-discharge at various current densities variable cut-off voltage according to the current density used: at 5 mA cm$^{-2}$ $E_{cut\text{-}off}$ = 0.4, at 10 mA-cm$^{-2}$ $E_{cut\text{-}off}$ = 0.35, at15 mA-cm$^{-2}$ $E_{cut\text{-}off}$ = 0.28, at 20 mA-cm$^{-2}$ $E_{cut\text{-}off}$ = 0.20, and at 25 mA-cm$^{-2}$ $E_{cut\text{-}off}$ = 0.15).

In Figure 72 the discharge profiles at different current densities are presented, at higher current densities the performance of the battery decrease. At 5 mA cm$^{-2}$, the cell potential for the 1$^{st}$ plateau is 0.78 V while at 25 mA cm$^{-2}$ it is only 0.38 V. In Figure 73 both the specific capacity and energy density *vs* the applied current density are presented.

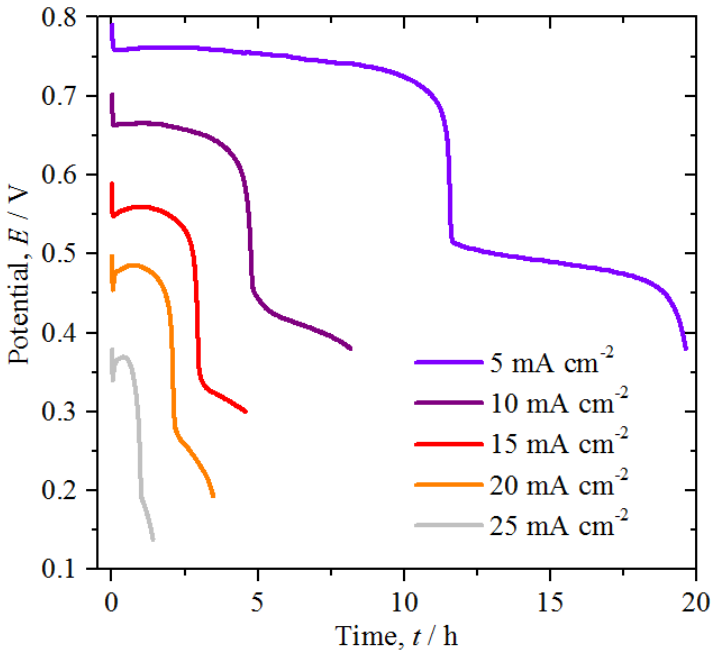


Figure 72. Discharge curves of prototype 5 with only one air electrode at different current densities in prototype 5.

If the stored energy and charge that were stored in each case is calculated it is possible to plot the energy density/specific capacity *vs* the discharge current density.

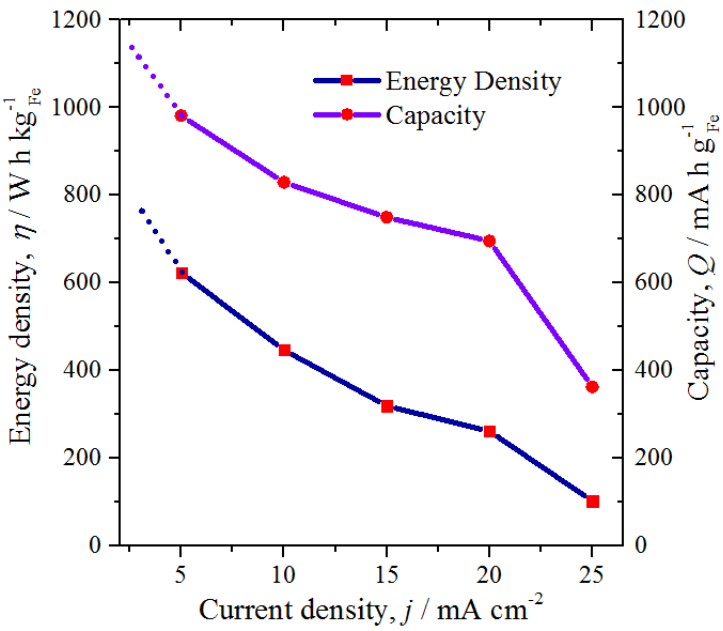


Figure 73. Effect of current density on the energy density and capacity of the whole discharge cycle using prototype 5.

From Figure 72 and Figure 73 it is possible to determine the mean power density for each case, by reading the energy density at each current density, and the time required to deliver the energy Table 13.

Table 13. Energy and power density for the IAB in prototype 5 at various current densities.

| **Current Density, *J*** | | **Energy density, *h*** | **Time, *t*** | **Power density, *P*** |
|---|---|---|---|---|
| mA $cm^{-2}$ | mA $g^{-1}_{Fe}$ | W h $kg^{-1}$ | h | W $kg^{-1}_{Fe}$ |
| 5 | 50 | 625 | 19.60 | 31.89 |
| 10 | 100 | 447 | 8.15 | 54.85 |
| 15 | 150 | 320 | 4.56 | 70.18 |
| 20 | 200 | 262 | 3.46 | 75.72 |
| 25 | 250 | 103 | 1.40 | 73.57 |

The energy density achieved with the IAB at this point is promising, for example a currently commercially available li-ion 36 V / 13 Ah battery claim to deliver *ca.* 468 W h, the whole battery pack weights 3 kg which implies an energy density of 156 W h per kg of the whole battery (Bosh, Vision power pack), usually Li-ion batteries real energy density range between ⅓ and ¼ of their theoretical value, assuming a similar range for the IAB system at 5 mA $cm^2$ it could potentially end with a battery cell pack of approximately 150 - 200 W h $kg^{-1}$.

Furthering the characterisation of the IAB in Figure 74 the observed IR drop of the cell is presented. In this figure the $E_{air}$ (red), and the $E_{iron}$ (blue) electrode potentials measured experimentally *vs.* the Hg/HgO reference electrode together with the calculated difference $E_{air} - E_{iron}$ (blue), and the measured cell potential $E_{cell}$ (black) are presented. The numerical difference between the individual electrodes *vs.* the Hg/HgO (blue) and the directly measured ones (black) would correspond to the *IR* drop due to the ohmic resistance in the cell (cyan), $E_{cell} = E^{o}_{cell} - \sum|\eta| - \sum IR_e$ . As expected, the *IR* drop obeys the Ohm's law and can be approximated using a standard linear fit by $V_{IR}$ /mV = 4.8 (*j*/mA $cm^{-2}$ + 28). Given that the electrode has a geometrical area of 25 $cm^2$ and the inter-electrode separation is 5 mm, the associated ohmic drop is 192 mΩ. If it is assumed that this resistance is only due to the electrolyte, this implies a resistivity value of 3.84 Ω cm. This value is in the same order of magnitude of the conductivity of 30% w/w KOH at 25 $^{o}$C in aqueous

solutions of 1.6 Ω cm [98]. Implying that there are not very high ohmic losses or that these are in the same order of magnitude of the conductive electrolyte.

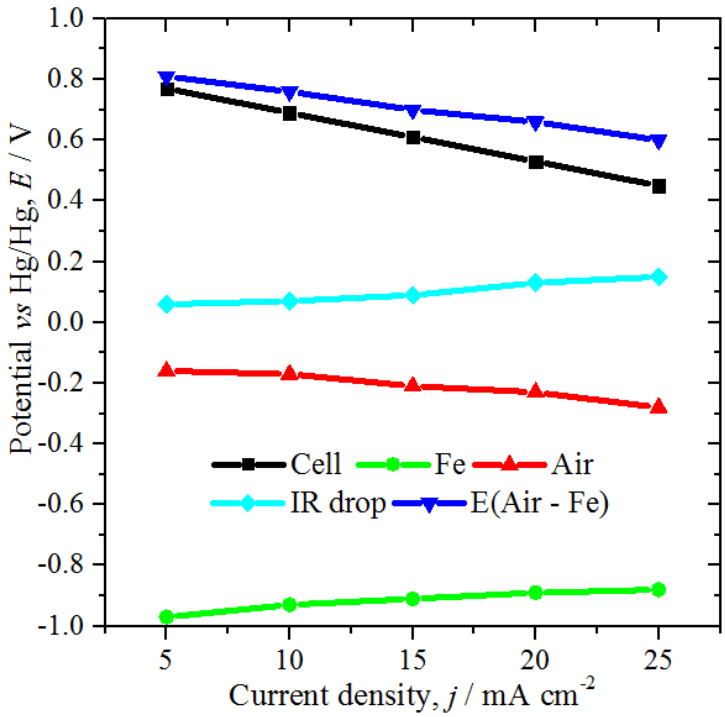


Figure 74. Effect of current density on the energy density and capacity of the whole discharge cycle using prototype 5.

## 8.9 Charge-discharge profiles considering only the 1st plateau

In the experiment presented in the previous section it was intended to determine what was the maximum capacity and energy output of the iron air battery. That is why the iron electrode was completely discharged to the second plateau. Nevertheless, the second plateau operates at a lower potential, for this reason, it was decided to determine its performance if only the first plateau is considered.

In order to study the performance of the IAB only discharging the first plateau a similar set up as before was used. Same electrolyte KOH 6M, reference electrode (Hg/HgO), air supply rate (1dm$^3$ min$^{-1}$). The only difference is that in this case the charge-discharge cycles were at a fixed current density of ±10 mA cm$^{-2}$ and a cut off voltage of 0.5 V was applied instead to ensure that only the first plateau was discharged. The procedure was repeated 20 times and these results are presented in Figure 75.

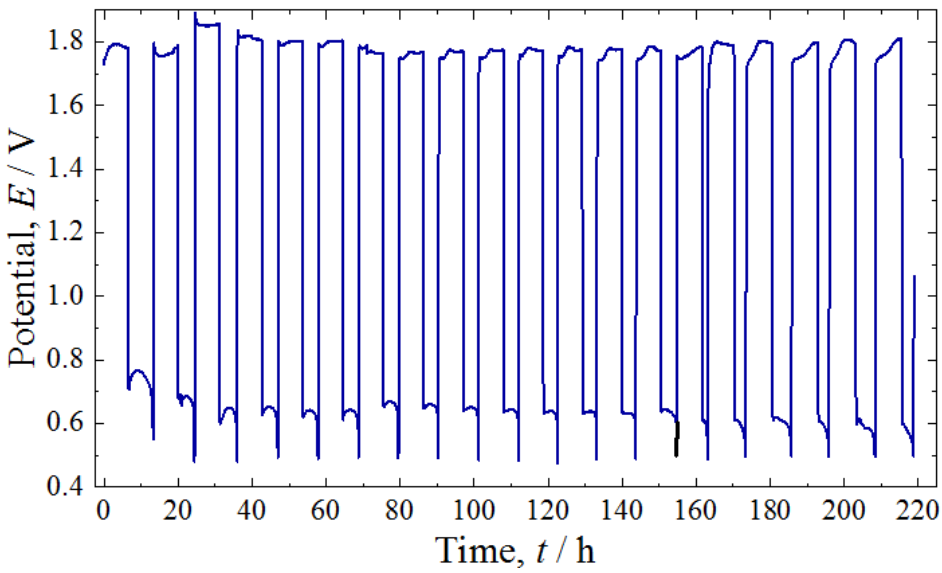


Figure 75. Charge-discharge profile. Cut off voltage set up at 0.5 V. Only the 1st plateau is discharged inside prototype 5 using only 1 air electrode, KOH 6M electrolyte, Hg/HgO reference electrode.

From the length of the charge and discharge plateaus (in hours) it is possible to calculate the capacity since the applied current is known. And by multiplying this

value by the mean voltage (during that particular dicharge) the energy density can be determined as well.

This had been done for each one of the 20 cycles presented in Figure 75 and the results sumarrized in Figure 76.

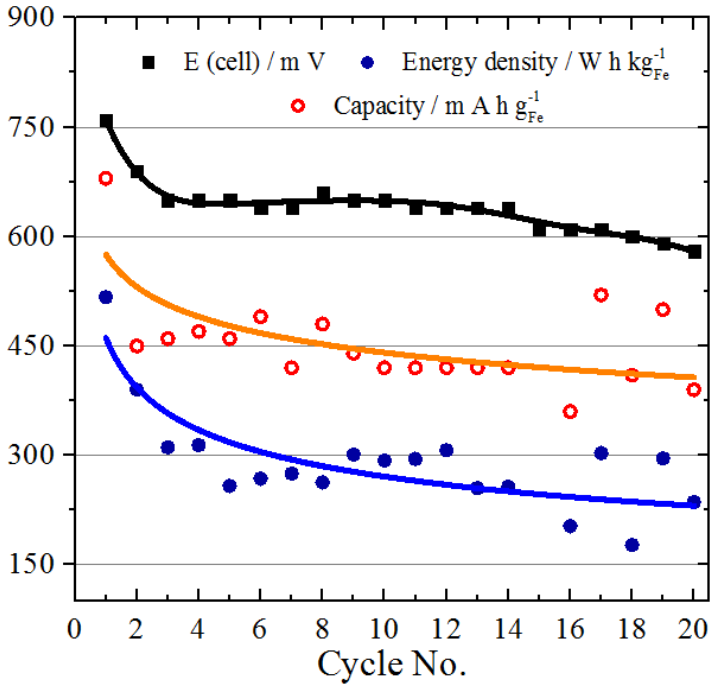


Figure 76. Capacity and energy density for each cycle presented in Figure 73.

As it is appreciable from Figure 76 the capacity and energy densiy are in average *ca.* 420 mA h $g^{-1}_{Fe}$ and 300 W h $kg^{-1}_{Fe}$ respectively.

## 8.10 Life cycle and deterioration of the IAB components

At an early stage of the project, one of the main challenges with the IAB system was related to the electrolyte leaks, not only through the cell, but as well through the air electrode given enough time. At some point, it was questioned if the hydrophobic properties (given by the PTFE) were lost after prolonged use within the strong alkaline environment. That is why a simple test was done.

In Figure 77 compares a piece of carbon cloth that had been left submerged in distilled water *vs* a piece of the same carbon cloth that had been left submerged in

the electrolyte KOH 6M for *ca.* 4 h. As it can be appreciated, the PTFE contained in the carbon cloth shape changed from long and thin filaments (left) to an agglomerate grumps shape (right). At a macroscopic level the carbon cloth left in the electrolyte KOH 6M had lost its hydrophobic properties after being left submerged.

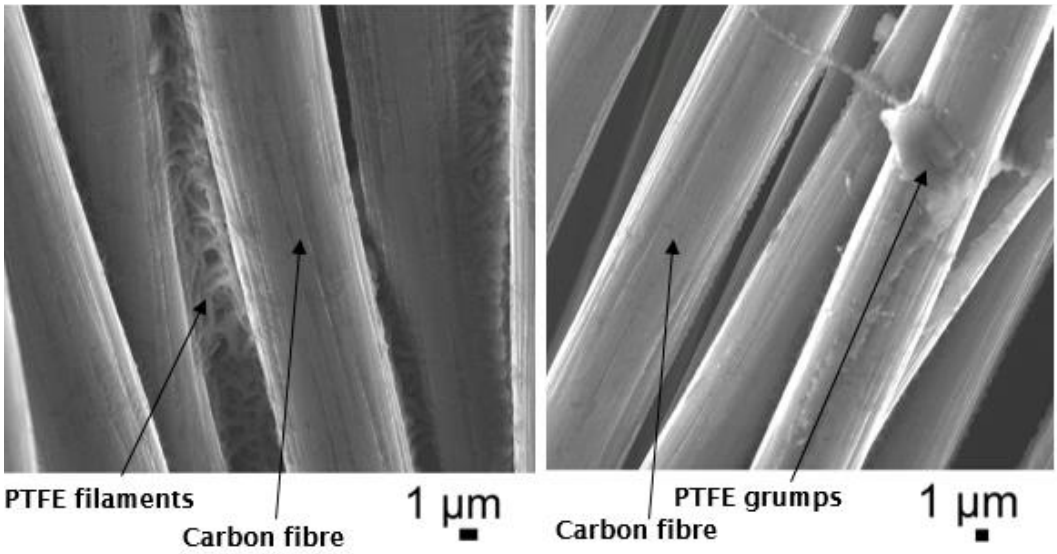


Figure 77. Scanning electron micrographs of the surface of carbon cloth after 4 h treatment with (left) distilled wather, and (rigth) 6M KOH, the one on the right lost had lost its hydrofobicity.

Given these results, it was decided to increase the loading of PTFE in the air electrode to ensure a longer lifetime. Including a 40% of PTFE in the catalyst layer of the air electrodes provided a way to stop the leaks though the air electrode throughout its laboratory lifetime.

## 8.11 Performance of the IAB stack

After having performed various test in one cell, the next natural step was to connect various cells together in a stack and to measure its performance.

The first attempt to characterise the performance of the stack was a charge-discharge protocol, 5 IAB cells were connected in series to ensure the same current passed through each one of them. Each IAB cell consisted in one iron electrode and one air electrode, the electrolyte used was again KOH 6M. Galvanostatic measurements at different current densities were applied at 5, 10, 15 and 20 mA

cm$^{-2}$, while air was supplied to the gas diffusion side of the air electrodes. The charge–discharge profile is shown in Figure 78. The charging phase lasted for 10 h.

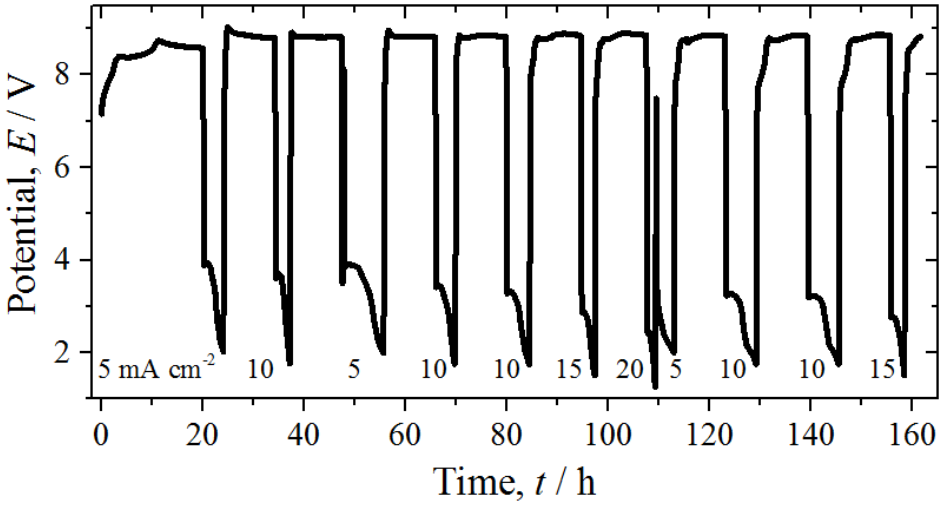


Figure 78. Charge-discharge cycling of the 5 IAB cells-stack.

The best cycles at each current density were chosen and presented in Figure 79, these, can be used to compare the stack performance at different current densities. A similar behaviour as the one observed in prototype 5 is observed (see Figure 72). But in this case the differentiation between both discharge plateaux is not that well defined, probably this is because the moment when the electrochemical reaction changes from the 1$^{st}$ plateau to the 2$^{nd}$ one does not happened simultaneously in each one of the 5 independent cells Figure 84.

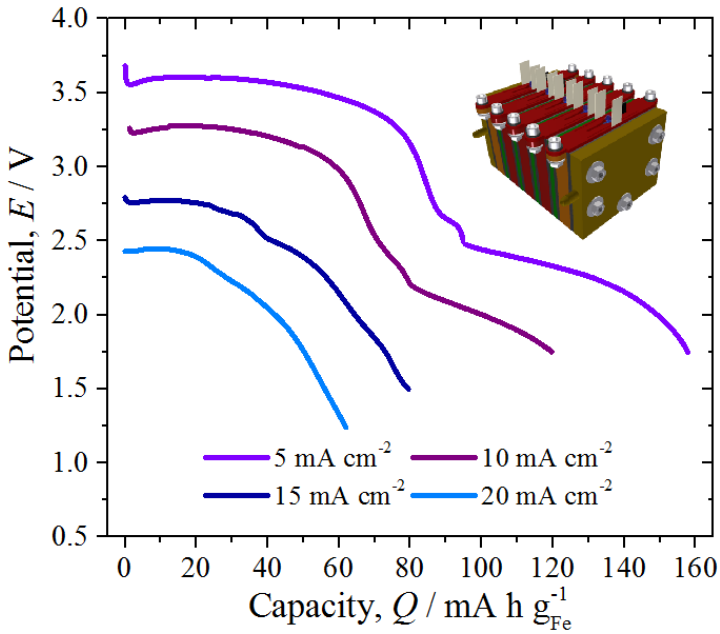


Figure 79. Discharge profiles of the 5 IAB cells-stack a t various current densities.

The stack capacity was low compared with the one observed in prototype 5 with only 1 cell. In the stack only 160 mA h $g^{-1}_{Fe}$ achieved on the cycle at 5 mA $cm^{-2}$, and even lower capacities were reached on the other cycles. It is not clear at this point why the full capacity of iron electrodes was not utilised, as the theoretically the capacity per gram of iron should be the same as in prototype 5. Maybe the air was not reaching at the same rate to the middle cells due to small air leaks.

The voltage of the stack was reasonable, given that each cell has an individual voltage of 0.76 V at 5 mA $cm^{-2}$ then the expected value was 0.76 V × 5 = 3.8 V close to the values observed in Figure 79 and the values are presented in Table 14 .

Table 14. Performance of the IAB 5 cells stack at different current densities.

| Current Density / mA $cm^{-2}$ | Stack voltage / V (1st plateau) | Capacity / mA h-$g^{-1}_{Fe}$ | Energy Density/ W h $kg^{-1}_{Fe}$ | Max. power / W | % Energy Efficiency |
|---|---|---|---|---|---|
| **5** | 3.6 | 160 | 464 | 0.45 | 26 |
| **10** | 3.3 | 120 | 319 | 0.83 | 18 |
| **15** | 2.8 | 80 | 192 | 1.05 | 11 |
| **20** | 2.4 | 62 | 130 | 1.20 | 7 |

In order to investigate further the performance of the stack each cell was monitored individually, In Figure 80, the charge-discharge profiles of the whole stack are in black and the individual cell potentials in different colours. This experiment allow us to realize that in general all cells were performing a similar way excepting for one. Cell 1 in red was having a lower performance than the rest of them.

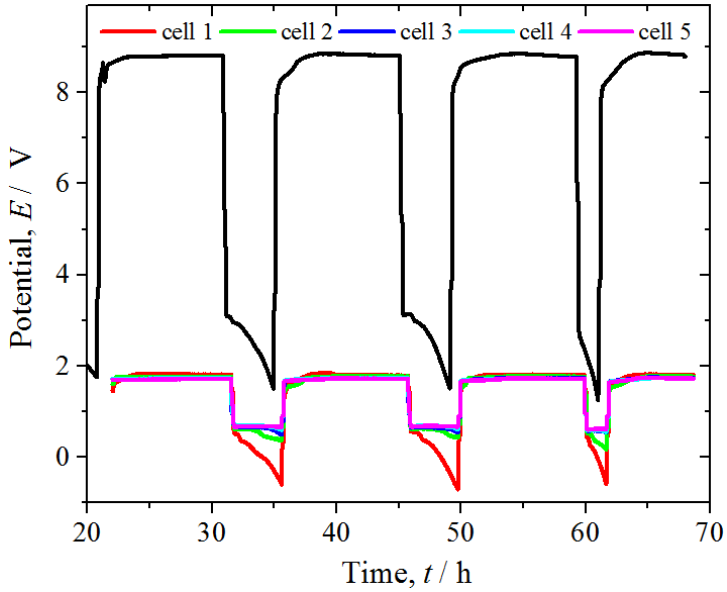


Figure 80. Charge discharge curves for the stack and the five cells that comprise the stack. The current density was 10 mA $cm^{-2}$, and the air flow rate was 1 L $min^{-1}$.

When the stack was disassembled electrolyte was found on the gas diffusion side of the air electrode of cell 1 and that electrolyte from cell 1 found its way out though a leak. This explained the poor performance of cell 1 (red line in Figure 80).

Additionally the polarisation curve of the stack cell was measured and presented in Figure 81. It is appreciable that at almost zero current, the stack voltage was 4.7 V, as the current density gradually increase the cell voltage decrease; at very low currents, the curve shows the cell voltage drop due to the kinetic control while the IR drop extends from around 100 to 800 mA with a linear cell voltage decrease. Mass transport limitations can be observed after 800 mA. At 1 A, the cell voltage has decreased to almost zero. This corresponds to a current density of 40 mA $cm^{-2}$ experienced by each cell, so this is the upper limit at that the cell can be run. The slope of the polarisation curve is quite steep, showing a rapid drop in voltage with increasing current density, probably because of the limitation on iron and air electrode performance.

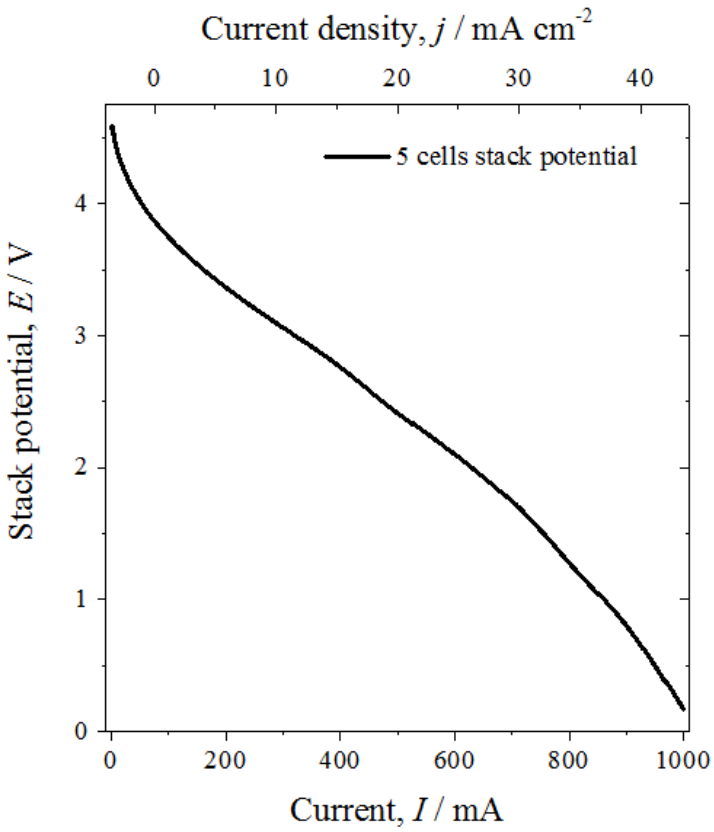


Figure 81. Polarisation curve of the stack, measured at a scan rate of 0.25 mA $s^{-1}$.

## 8.12 Electrochemical testing of 200 cm$^2$ electrodes

Besides connecting various cells together scaling up the iron and GDE electrodes was investigated. For this purpose a 200 cm$^2$ electrodes cell was developed using a similar design as in prototype 5. Many problems were encounter while testing these electrodes, nevertheless in Figure 82 the results obtained using these electrodes in the large 200 cm$^2$ cell are presented.

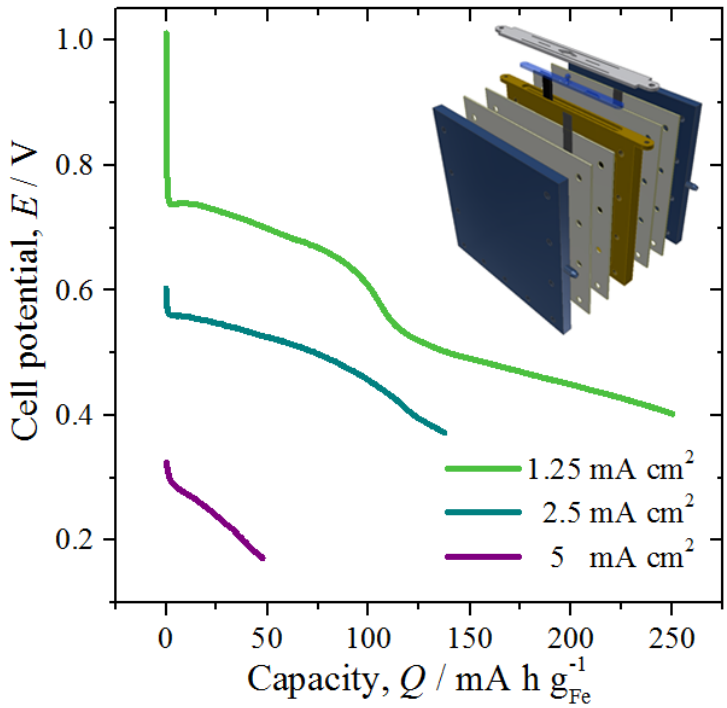


Figure 82. Discharge capacity profiles for the 200 cm$^2$ IAB cell at 1.25 mA cm$^{-2}$, 2.5 mA cm$^{-2}$ and 5 mA cm$^{-2}$ discharge rates.

When compared with the performance of both the 5-cells-stack (Figure 79) and the 25 cm$^2$ prototype 5 IAB (Figure 72), the performance of the 200 cm$^2$ cell was considerable lower, for example by comparing the case at 5 mA cm$^{-2}$, the stack achieved a capacity of 160 mA g$^{-1}_{Fe.}$ prototype-5 an outstanding 960 mA g$^{-1}_{Fe,}$ both of them considerable higher than the 50 mA g$^{-1}_{Fe}$ on the 200 cm$^2$ cell.

Many problems were observed when trying to scale up the cell, and manufacture the 200 cm$^2$ electrodes: On the air electrode side it was harder to ensure that the catalyst layer was as homogenously distributed as in the smaller electrodes, mostly because when spreading the catalyst ink due to the size of the large electrode it was hard to maintain it flat and this tend to concentrate the catalyst ink in certain areas,

the large iron electrode was supplied by TECNALIA and they were using a stainless steel mesh that was not as fine as the ones we used for our experiments, this mesh prove to be insufficient to avoid losing iron active material when cycling the battery, at the end of the test it was visible that after a short time (80 h) a large amount of both carbon an iron were lost. Another complication was that with the small air electrodes it was not that hard to avoid electrolyte leakage to the back part of the air electrodes but with the large cell this prove to be much more challenging. At the end I was required to use a large amount of silicon sealant at the edges just to be able to test the cell.

Definitely the air electrodes must include a smooth frame at its edges to ensure a proper sealing at the edges in combination with O-rings or silicon gaskets in future designs. The use of a finer mesh on the iron electrode could help to avoid losing material during its operation or it w

## 8.13 Conclusions on the performance of the IAB

Cell design and test performance of some preliminary cell prototypes were carried out under the following different conditions:

Prototype 1: An IAB flow battery. The cell was robust and heavy, the designs allows the use of two electrodes and separators in order to supply air/$O_2$ in case it is appropriate, different electrolyte to each half cell. However, the design was not suitable for the reactions of this electrochemical system since the bubbles formed during the charge-discharge process were trapped inside affecting its performance. A few tests at 1 mA $cm^{-2}$ were possible in this cell, with an energy density of 451 Wh-$kg^{-1}$ and the first and second discharge plateaus observed at $V_{1st}$ = 0.7 V and $V_{2nd}$ = 0.5 V at a current of density 1 mA $cm^{-2}$

Prototype 2: A screw-less IAB static cell interelectrode gap 5 mm: It was lighter than the previous design and had the advantage that it did not require screws making it easier to handle. It was designed to include two auxiliary nickel electrode for the charge that at the end were considered unnecessary. An air-venting valve was part of the lid.

Prototype 3: A screw-less IAB static cell interelectrode gap 3mm: It was even lighter than the previous design as well as prototype 2 it did not require screws. However, the way it was assembled caused considerable mechanical stress that damage in the GDE electrodes.

Prototype 4: A compact open air breathable static cell: This design was far more compact than the previous designs and allow us to test the air electrodes just as air breathing electrodes (no forced oxygen-air supplied) at different current densities. This was very light compared to the previous one but was not strong enough to hold tightly the air electrodes without leaks.

Prototype 5: A compact static cell with pumped air/$O_2$ supply: This design was basically an optimization of the previous design and allow us to test the IAB electrodes at different current densities with both oxygen and air supply. A small electrolyte leak tend to appear at the borders of the air electrodes and have loses due to evaporation of the electrolyte over time but these are manageable since they are small. It was concluded that a way to stop leaks completely will require the use of a stronger material that can be compressed hard enough without bending. Alternatively, a metal plate can be included in order to distribute the pressure more evenly over the end plates.

Stack based on prototype 5: A 5 individual cells stack based on Prototype. It allow as well the supply of air/$O_2$ during test to the gas diffusion side of the air electrodes, it allowed to test performance of a proof of concept IAB stack. Its performance were low compared with the individual cell and lower that what was expected, it was discovered later that leaks in the back side of one of the air electrodes lowered the overall performance of the stack.

3D printing is a fast and relatively low cost manufacturing technique that allows to test different cell design ideas quickly. ABS have been chemically compatible with the strong alkaline solution (KOH 6 M), is a relatively light and rigid material but cannot withstand that much stress without bending according to the experience shown in the laboratory.

The most challenging problems so far have been

1. Hydrogen evolution during charge that is suspected to cause the damage to the iron electrode and make it loss some material,
2. Slow leaks in the system that might cause dryness of the iron electrode. Since it is challenging to design a battery that seals property the air electrodes and that if unsupervised, part of the iron electrode is exposed to the air preventing the first discharge plateau from happening since the reaction involving the hydroxides requires electrolyte,
3. Loss of active material in the iron electrode; this might be resolved by using an extra amount of binder (PTFE) that may help and improve the life expectancy of this component.

It seems that the cell can run for a greater number of cycles (at least 20) with less deterioration in performance over time at 10 mA $cm^{-2}$ if one of the air electrodes is removed, so that the cell runs only with one air electrode parallel to the iron electrode. This could be due to differences in the charge distribution across the iron electrode, but more tests are required to verify if this is the case. A novel design should consider the use of only 1 air electrode per iron electrode.

# Chapter 9: Conclusions, future work and final remarks

In this final chapter, the most important results and conclusions achieved as part of this Ph.D. research project are highlighted. We will state which aspects of this research were limited and how could have been done better. Finally the future lines of research in order to continue the development of the IAB system will be discussed.

The first conclusion of this research will be confirming and having gained confident understanding of the electrochemical behaviour of the IAB system. Based on the operation principle various laboratory prototypes were developed and it was possible to observe the expected charge-discharge plateaus, a typical charge-discharge IAB profile is presented in Figure 83 at a current density of 10 mA $cm^{-2}$.

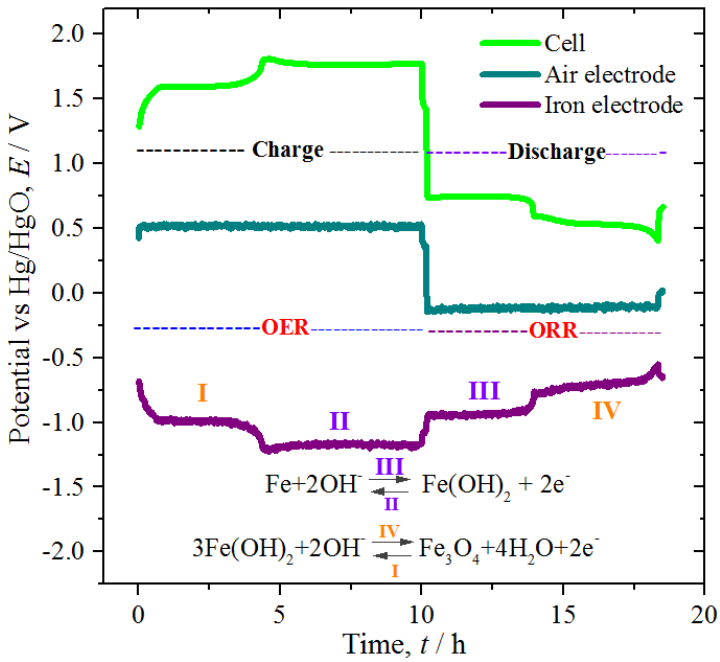


Figure 83. Typical charge-discharge IAB profile at 10 mA $cm^{-2}$.

During discharge, the theoretical capacity for this system is 960 mA h $g^{-1}_{Fe}$ for the first plateau and additional 313 mA h $g^{-1}_{Fe}$ for the second discharge plateau giving a total of 1273 mA h $g^{-1}_{Fe}$ when both plateaus are discharged. From the iron electrodes experiments performed in chapter 3, the maximum capacity was obtained with a $Fe_2O_3$/C hot pressed electrode with a value of 915 mA h $g^{-1}_{Fe}$ (71% of the

theoretical capacity) which is encouraging to further the development of iron electrodes using similar formulations.

The thermodynamically predicted IAB cell potential for the first plateau is 1.28 V and for the second 1.16 V. When discharged at the laboratory at a current density of 5 mA $cm^{-2}$ the observed potentials were *ca.* 0.75 V and 0.53 V which represents 58% and 45% of the thermodynamic values for each plateau respectively.

The equilibrium potential for the oxygen reactions is 0.441 V *vs* SHE or 0.556 V *vs* Hg/HgO, (considering that the 1 M KOH Hg/HgO has a potential of -0.115 V *vs* the SHE), the observed potentials for the OER and ORR at 5 mA $cm^{-2}$ are *ca.* 0.52 V and -0.11 V *vs* the Hg/HgO, which differs only 36 mV for the OER and 660 mV for the ORR.

When comparing the potentials of each plateau for the iron electrode, it was noticed that for the reaction corresponding to the oxidation of iron to iron oxide, (marked with II and III in Figure 83) the charge and discharge potentials are *ca* -1.15 V and -0.95 V *vs* Hg/HgO, representing a difference of 20 mV and for the oxidation of iron hydroxide to iron III oxide (marked with I and IV in Figure 83) -0.98 V and -0.70 V *vs* Hg/HgO representing a difference of 28 mV, which are actually small and manageable over potentials.

Similarly for the air electrode the observed potentials for the OER and ORR at 5 mA $cm^{-2}$ are *ca.* 0.52 V and -0.12 V *vs* the Hg/HgO. This difference of *ca.* 700 mV lowers the overall voltage efficiency of the IAB battery and in general is a challenge that most MAB face.

When comparing the ratio of the delivered-potential to the charging-potential for each plateau it would be observable that these ratios are 0.75 V/1.7 V (plateaus II and III) and 0.55 V/1.6 V (plateaus I and IV) which represent voltages efficiencies of 44% and 33% respectively. By comparing directly the areas beneath the charge phase (green line from 0 h – 10 h) and the discharge phase (green line 10 h – 18 h) it is possible to determine the an energy efficiency of *ca.* 30%.

Some interesting results were achieved testing novel bifunctional catalyst, this line of research will have to continue trying novel bifunctional materials formulations in our in-house GDE. In the future using new manufacturing techniques to ensure

that the catalyst layer is uniformly distributed over the surface of the GDE electrodes is advised since that was a potential limitation of our current research, even though efforts were done in the lab to ensure the catalyst layer to be as uniformly as possible still a more standardized technique may be required to ensure that the catalyst layer is always homogenously dispersed.

At some point while characterising the IAB it was suggested to use X-ray tomography to observe three-dimensionally the meso- and micro- porous structure of GDE to determine important geometric parameters such as pore size and tortuosity that would be relevant to study in detail the oxygen diffusion within the structure of GDE. Following this line of research, a 3D reconstruction of a section of 1 mm x 1 mm x 1 mm of a GDE electrode was determined by mapping the difference is density within this sample. These results were presented in section 6.4. Nevertheless at the end of my Ph.D. I focused mostly on the characterisation of iron electrodes reason why this line of research was not further developed but could be interesting to pursue in the future and measure and characterise in more detail the porous structure of GDE and implement a simulation of the oxygen diffusion species within its structure to determine how high the current density can be raised before starting to observe a limiting current by the oxygen diffusion transport.

Similarly, one of the expected problems with the IAB system is the volume change of the iron electrode during its operation, (as was explained in section 3.4), as a future line of research it is suggested to use X-ray tomography to observe this volume change *during operation*. This study will be relevant to design HPIE porous enough to avoid clogging and optimize the iron utilization during its operation.

The engineering design of the IAB considered using an iron electrode in combination with two GDE, since in the literature reviews it was mentioned that that way it was possible to extend the operation lifetime of the GDE, nevertheless our in-house GDE did not get damaged or deteriorated and it was possible to test the iron electrodes using only one gas diffusion electrode. This imply that in the future this would be our recommended approach when designing a new prototype for this system.

Similarly another configuration that would be interested to develop in the future is to use a nickel counter electrode to charge the iron electrode and to discharge the

iron electrode using a GDE, this configuration offers certain advantages. The first one is that in principle this way it will not be required to develop a bifunctional catalyst but only a suitable electrocatalysts for the oxygen reduction reaction which may open the possibility to test other reported materials that only focus on the electro-catalyst of the ORR. The idea of having 3 electrodes within the battery obviously has the drawback that this will lower the energy density of the system since it will require an additional electrode just for charging the battery, but it might be possible to design the IAB in such a way that it can be docked to a charging station where the nickel counter electrodes are located and once it is charged to undock it in such a way that the nickel electrodes are not inside the battery but only the iron electrode and the gas diffusion electrode optimised for the ORR, this idea may allow to fast charge the iron electrode.

Summarising the potential research paths to pursue the research of the IAB system, and the tasks at hand in the following months after the completion of this Ph.D. research are presented:

- Compare novel types of perovskites and continue the comparison with the ones that we have reported in this thesis and in the related publications.
- Deposit the catalyst layer in a more controlled way using spay guns techniques to ensure very thin and homogenous catalyst layers.
- Test the developed GDE using other metals, in other types of MAB such as the primary zinc-air system and compare its performance with the commercially available ones.
- Determine if the use of sulphides in the electrolyte may affect the performance of GDE and if they do. Research the possibility of using a suitable ionic membrane in the IAB system when these are added to the electrolyte.
- The continued use of X-ray tomography to determine the required parameters to simulate the $O_2$ diffusion species within the structure of the GDE and estimate under which conditions the GDE will be limited by the mass transport of these species.
- Use X-ray tomography to observe the change in volume in the fully charged and fully discharged state of HPIE. Use these results to improve the required

porosity in these type of electrodes to ensure a better utilization of the iron active material.

- Use novel manufacturing techniques such as metal 3D printing and sintering to compare the performance of the best performing iron active formulations including $Fe_2O_3$/C synthetized by the Adams method as described in section 5.5.
- Further study the compatibility of the IAB working with the addition of sulphides in the electrolyte formulations, it may seem that these sulphides have a positive effect on the coulombic efficiency of the iron electrode during the charge process but my affect the performance of the GDE, further experiments will be required to confirm or deny this hypothesis.
- Another aspect of the electrode characterisation that was not done during this phase, was to study the temperature influence in the performance of both the iron and air electrodes. In the future once an optimised formulation is outlined it will be required to study how the performance of these electrodes is modified at different temperatures.

It will be of the interest of the reader that wants to pursue this research some relevant caveats that should be taken into account when furthering the research of the IAB system:

- The studies related to the electrochemical characterisation of HPIE were limited by the amount of time that was allowed for the potentiostat to be used in the laboratory, that is why it was not possible to ensure the same number of reduction-oxidation cycles for the HPIE under study. In the future it would be ideal to further these characterisation over longer periods of time and to ensure that all the electrodes finished on the totally charge (reduced) or discharged (oxidised) state, which would allow a fairer comparison of the electrode materials after cycling.
- Another caveat to be taken in mind is the fact that overtime water in the electrolyte will evaporate this should be taken into account when setting up a cycling experiment for longer periods of time to ensure that the p.H. of the electrolyte solution is keep at the very same value.

- It has been attributed to the addition of sulphides into the electrolyte an enhanced performance of HPIE, and according to [41], it is suggested that the presence of sulphides ions will diminish over time, it would be ideal to continue this line of research in such a way that it is possible to measure the sulphides concentration over time while the HPIE is being tested either in a half cell configuration or in an IAB configuration.
- The last point has to be studied in detail, since it is important to determine if the oxidation of these sulphides will have an adverse effect on the performance of the GDE when connected in an IAB configuration, in which case it may require a membrane.
- Determining the discharge capacity of the IAB and the HPIE on a half-cell configuration was performed at various C discharge rates, but there was no time to further study the effect of charging these electrodes at different C rates, this line of research should be pursued in the future to complete the electrochemical performance of HPIE.

# Appendix A NECOBAUT flow cell design

This first prototype was composed of a series of plates, gaskets, electrolyte channels, electrodes, electrolyte inlets/outlets and air inlets/outlets as shown in Figure 84. This cell have been designed in such a way that two different electrolytes flows could be used independently at the counter electrode and between the separator and the air electrode. Also a compartment to allow the air to flow is part of the battery.

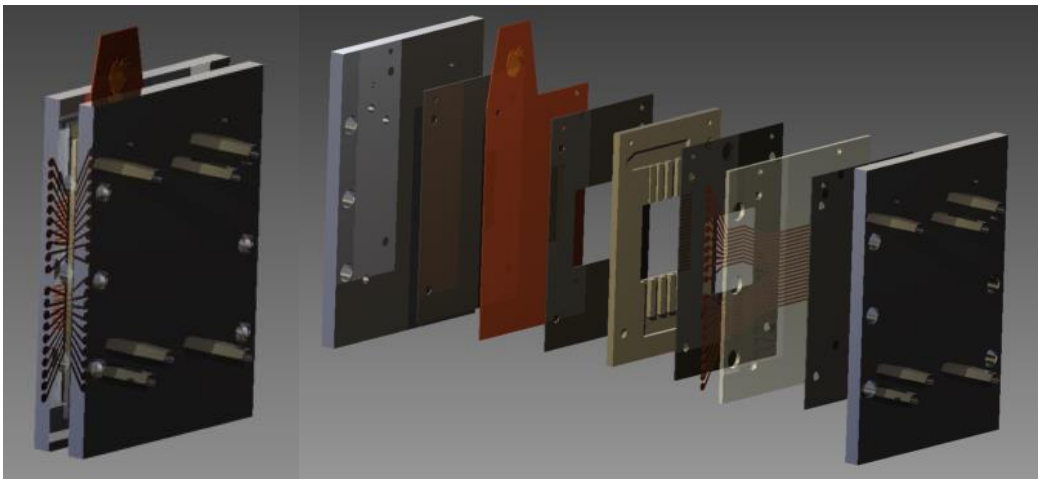

Figure 84. NECOBAUT Iron-air battery laboratory prototype.

Table 15. NECOBAUT complete list of components specification.

| | Component | Materials | Thickness mm | Height mm | Width mm |
|---|---|---|---|---|---|
| **1** | End Plate | Stainless Steel 316 | 10.0 | 190 | 140 |
| **2** | Gasket | Silicone | 1.5 | 150 | 100 |
| **3** | Cu Plate/ Counter Electrode | Copper | 1.0 | 150 | 100 |
| **4** | Gasket | Silicone | 1.5 | 150 | 100 |
| **5** | Electrolyte compartment 2 | Polypropylene | 5.0 | 150 | 100 |
| **6** | Gasket | Silicone | 1.5 | 150 | 100 |
| **7** | Separator PEM | Nafion | <0.5 | 150 | 100 |
| **8** | Gasket | Silicone | 1.5 | 150 | 100 |
| **9** | Electrolyte Compartment 1 | Polypropylene | 5.0 | 150 | 100 |

| | | | | | |
|---|---|---|---|---|---|
| **10** | Gasket | Silicone | 1.5 | 150 | 100 |
| | Air Electrode | | 1.0 | 150 | 100 |
| **11** | Gasket | Silicone | 1.5 | 150 | 100 |
| | Flow Air Compartment | Polypropylene | 5.0 | 150 | 100 |
| **12** | Gasket | | 1.5 | 150 | 100 |
| **13** | End Plate | Stainless Steel 316 | 10.0 | 190 | 140 |

Under different experimental conditions the battery may only need to be connected with fewer elements, for example in our case the same electrolyte is being used in both chambers allowing the reader to take away the separator and only use one electrolyte compartment. The experimental configuration used during the following experiments is presented in Figure 85, and the respective listing of elements is detailed in Table 15 .

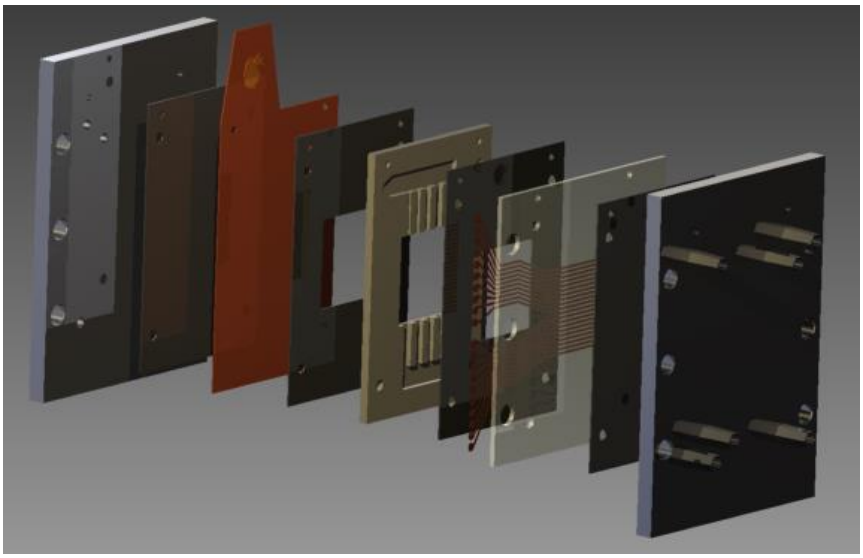

Figure 85. Actual NECOBAUT configuration for cell-characterisation-laboratory testing

Table 16. Used cell components specification.

| | Component | Materials | Thickness (mm) | Height mm | Width mm |
|---|---|---|---|---|---|
| **1** | End Plate | Stainless Steel 316 | 10 | 190 | 140 |
| **2** | Gasket | Silicone | 1.5 | 150 | 100 |
| **3** | Cu Plate/ Counter Electrode | Copper | 1 | 150 | 100 |
| **4** | Gasket | Silicone | 1.5 | 150 | 100 |
| **5** | Electrolyte compartment | Polypropylene | 5 | 150 | 100 |
| **6** | Gasket | Silicone | 1.5 | 150 | 100 |
| **7** | Segmented Electrode/ Working Electrode | Copper over epoxy layer or over fibre glass layer | 1 | 150 | ~200 |
| **8** | Gasket | Silicone | 1.5 | 150 | 100 |
| **9** | End Plate | Stainless Steel 316 | 10 | 190 | 140 |

This configuration was the one that was used to determine the hydrodynamic and mass transport distribution in the cell would give key valuable information for design purposes.

# Appendix B Activities chronogram

In this section a Gant diagram of the various activities and milestones related to my research is presented to show the project management that was followed during my research.

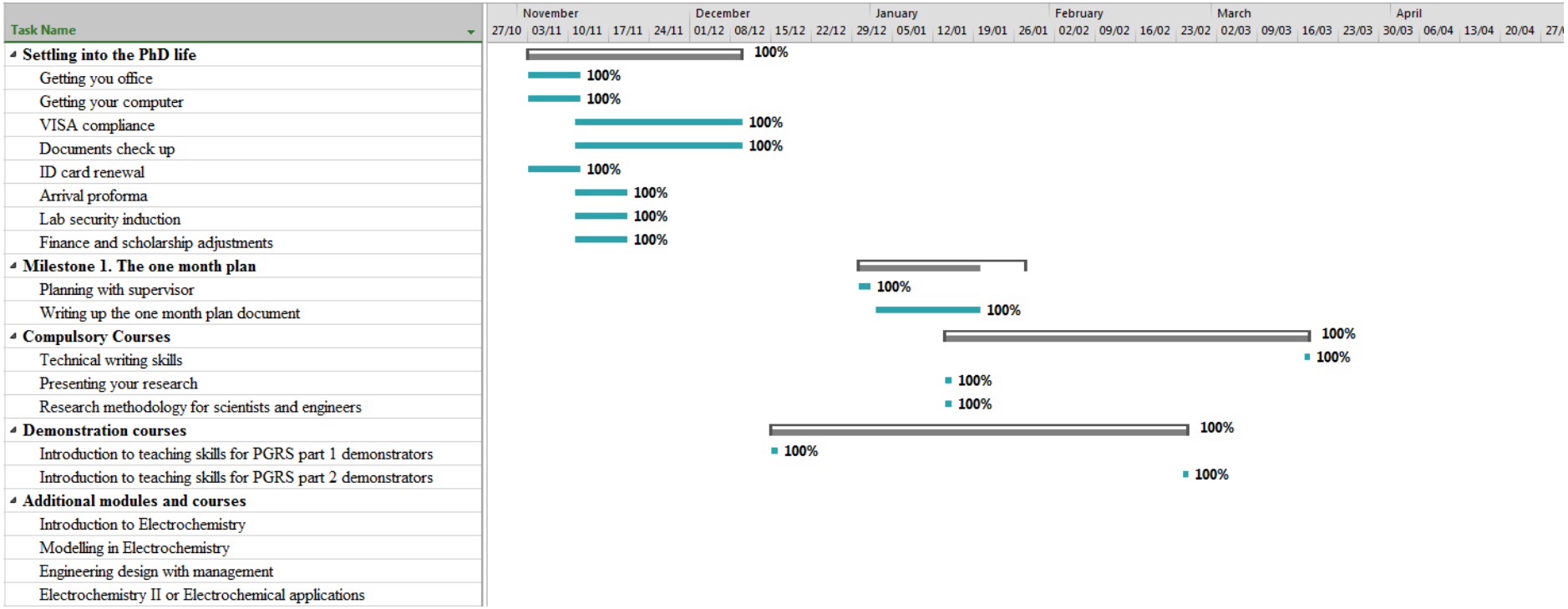
Task Name
November
December
January
February
March
April
27/10 03/11 10/11 17/11 24/11 01/12 08/12 15/12 22/12 29/12 05/01 12/01 19/01 26/01 02/02 09/02 16/02 23/02 02/03 09/03 16/03 23/03 30/03 06/04 13/04 20/04
Settling into the PhD life
Getting you office
Getting your computer
VISA compliance
Documents check up
ID card renewal
Arrival proforma
Lab security induction
Finance and scholarship adjustments
Milestone 1. The one month plan
Planning with supervisor
Writing up the one month plan document
Compulsory Courses
Technical writing skills
Presenting your research
Research methodology for scientists and engineers
Demonstration courses
Introduction to teaching skills for PGRS part 1 demonstrators
Introduction to teaching skills for PGRS part 2 demonstrators
Additional modules and courses
Introduction to Electrochemistry
Modelling in Electrochemistry
Engineering design with management
Electrochemistry II or Electrochemical applications
100%

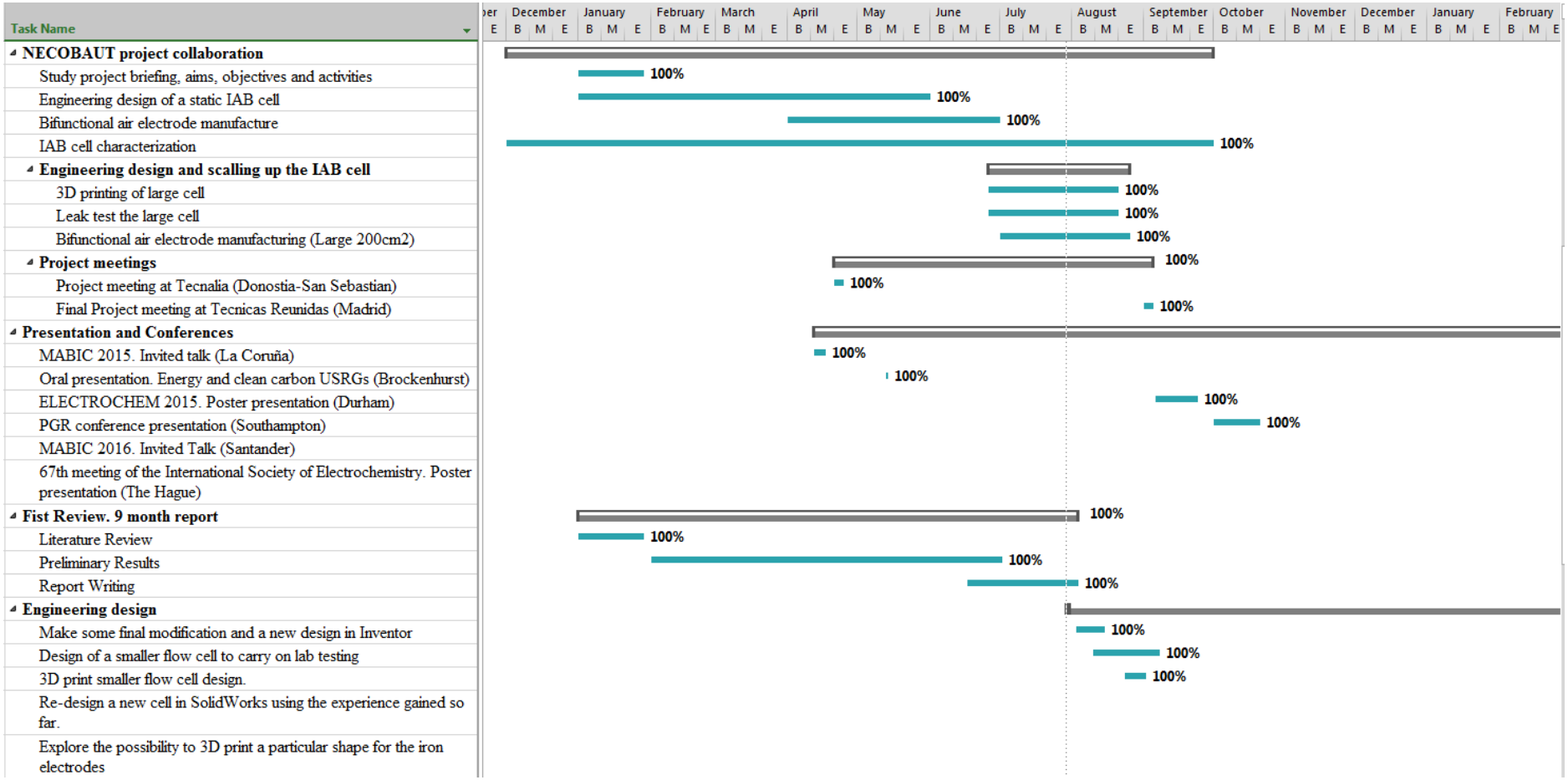
Task Name
NECOBAUT project collaboration
Study project briefing, aims, objectives and activities
Engineering design of a static IAB cell
Bifunctional air electrode manufacture
IAB cell characterization
Engineering design and scalling up the IAB cell
3D printing of large cell
Leak test the large cell
Bifunctional air electrode manufacturing (Large 200cm2)
Project meetings
Project meeting at Tecnalia (Donostia-San Sebastian)
Final Project meeting at Tecnicas Reunidas (Madrid)
Presentation and Conferences
MABIC 2015. Invited talk (La Coruña)
Oral presentation. Energy and clean carbon USRGs (Brockenhurst)
ELECTROCHEM 2015. Poster presentation (Durham)
PGR conference presentation (Southampton)
MABIC 2016. Invited Talk (Santander)
67th meeting of the International Society of Electrochemistry. Poster presentation (The Hague)
Fist Review. 9 month report
Literature Review
Preliminary Results
Report Writing
Engineering design
Make some final modification and a new design in Inventor
Design of a smaller flow cell to carry on lab testing
3D print smaller flow cell design.
Re-design a new cell in SolidWorks using the experience gained so far.
Explore the possibility to 3D print a particular shape for the iron electrodes
December
January
February
March
April
May
June
July
August
September
October
November
December
January
February
100%

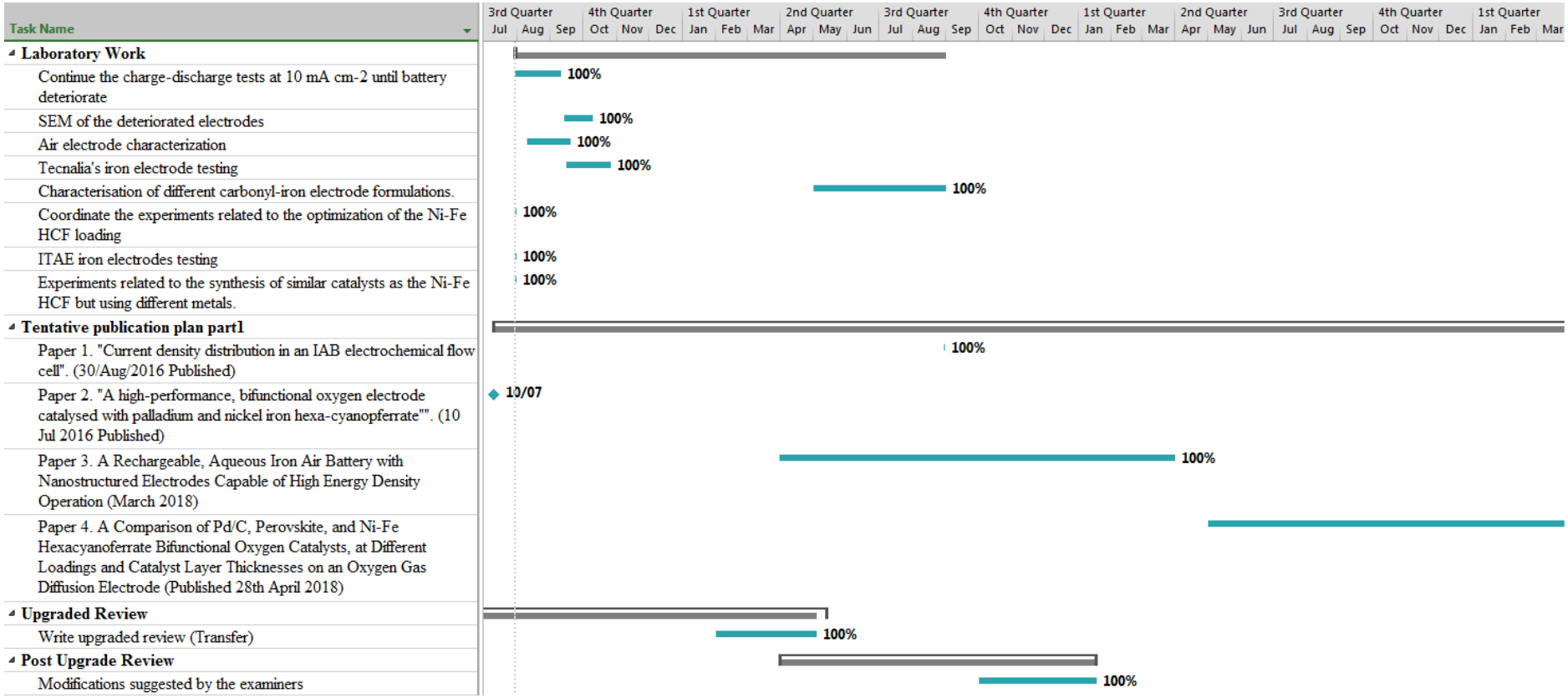
Task Name
3rd Quarter
4th Quarter
1st Quarter
2nd Quarter
3rd Quarter
4th Quarter
1st Quarter
2nd Quarter
3rd Quarter
4th Quarter
1st Quarter
Jul Aug Sep Oct Nov Dec Jan Feb Mar Apr May Jun Jul Aug Sep Oct Nov Dec Jan Feb Mar Apr May Jun Jul Aug Sep Oct Nov Dec Jan Feb Mar
Laboratory Work
Continue the charge-discharge tests at 10 mA cm-2 until battery deteriorate
SEM of the deteriorated electrodes
Air electrode characterization
Tecnalia's iron electrode testing
Characterisation of different carbonyl-iron electrode formulations.
Coordinate the experiments related to the optimization of the Ni-Fe HCF loading
ITAE iron electrodes testing
Experiments related to the synthesis of similar catalysts as the Ni-Fe HCF but using different metals.
Tentative publication plan part1
Paper 1. "Current density distribution in an IAB electrochemical flow cell". (30/Aug/2016 Published)
Paper 2. "A high-performance, bifunctional oxygen electrode catalysed with palladium and nickel iron hexa-cyanopferrate"". (10 Jul 2016 Published)
Paper 3. A Rechargeable, Aqueous Iron Air Battery with Nanostructured Electrodes Capable of High Energy Density Operation (March 2018)
Paper 4. A Comparison of Pd/C, Perovskite, and Ni-Fe Hexacyanoferrate Bifunctional Oxygen Catalysts, at Different Loadings and Catalyst Layer Thicknesses on an Oxygen Gas Diffusion Electrode (Published 28th April 2018)
Upgraded Review
Write upgraded review (Transfer)
Post Upgrade Review
Modifications suggested by the examiners
100%
10/07

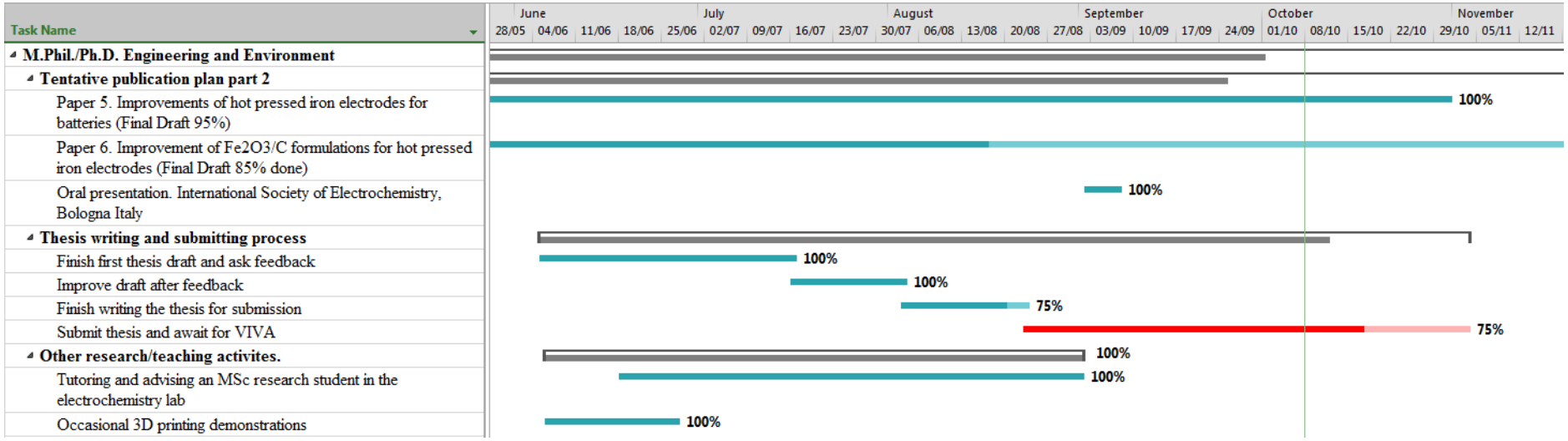
Task Name
June
July
August
September
October
November
28/05 04/06 11/06 18/06 25/06 02/07 09/07 16/07 23/07 30/07 06/08 13/08 20/08 27/08 03/09 10/09 17/09 24/09 01/10 08/10 15/10 22/10 29/10 05/11 12/11
M.Phil./Ph.D. Engineering and Environment
Tentative publication plan part 2
Paper 5. Improvements of hot pressed iron electrodes for batteries (Final Draft 95%)
100%
Paper 6. Improvement of Fe2O3/C formulations for hot pressed iron electrodes (Final Draft 85% done)
Oral presentation. International Society of Electrochemistry, Bologna Italy
100%
Thesis writing and submitting process
Finish first thesis draft and ask feedback
100%
Improve draft after feedback
100%
Finish writing the thesis for submission
75%
Submit thesis and await for VIVA
75%
Other research/teaching activites.
100%
Tutoring and advising an MSc research student in the electrochemistry lab
100%
Occasional 3D printing demonstrations
100%

# References


[1] A. Garcia, NECOBAUT, (2012). http://www.necobaut.eu/home/home.php (accessed 4 November 2016).

[2] R.D. McKerracher, C. Ponce de Leon, R.G.A. Wills, A.A. Shah, F.C. Walsh, A review of the iron–air secondary battery for energy storage, Chempluschem. 80 (2015) 323–335. doi:10.1002/cplu.201402238.

[3] H.A. Figueredo-Rodríguez, R.D. McKerracher, C. Ponce de León, F.C. Walsh, Current distribution in a rectangular flow channel manufactured by 3-D printing, AIChE J. 63 (2017) 1144–1151. doi:10.1002/aic.15454.

[4] R.D. McKerracher, C. Alegre, V. Baglio, A.S. Aricò, C. Ponce de León, F. Mornaghini, M. Rodlert, F.C. Walsh, A nanostructured bifunctional Pd/C gas-diffusion electrode for metal-air batteries, Electrochim. Acta. 174 (2015) 508–515. doi:http://dx.doi.org/10.1016/j.electacta.2015.06.001.

[5] R.D. McKerracher, H.A. Figueredo-Rodríguez, C. Ponce De León, C. Alegre, V. Baglio, A.S. Aricò, F.C. Walsh, A high-performance, bifunctional oxygen electrode catalysed with palladium and nickel-iron hexacyanoferrate, Electrochim. Acta. 206 (2016) 127–133. doi:10.1016/j.electacta.2016.04.090.

[6] R.D. McKerracher, H.A. Figueredo-Rodríguez, J.O. Avila-Alejo, K. Kwasnicki, C.P. de León, C. Alegre, V. Baglio, A.S. Aricò, F.C. Walsh, A Comparison of Pd/C, Perovskite, and Ni-Fe Hexacyanoferrate Bifunctional Oxygen Catalysts, at Different Loadings and Catalyst Layer Thicknesses on an Oxygen Gas Diffusion Electrode, J. Electrochem. Soc. 165 (2018) A1254–A1262. doi:10.1149/2.0321807jes.

[7] H.A. Figueredo-Rodríguez, R.D. McKerracher, M. Insausti, A.G. Luis, C.P. de León, C. Alegre, V. Baglio, A.S. Aricò, F.C. Walsh, A rechargeable, aqueous iron air battery with nanostructured electrodes capable of high energy density operation, J. Electrochem. Soc. 164 (2017) A1148–A1157. doi:10.1149/2.0711706jes.

[8] H.A.F. Rodríguez, R.D. McKerracher, C.P. de León, F.C. Walsh, Improvement of Negative Electrodes for Iron-Air Batteries: Comparison of Different Iron Compounds as Active Materials, J. Electrochem. Soc. 166 (2019) A107–A117. doi:10.1149/2.1071816jes.

[9] R. Amirante, E. Cassone, E. Distaso, P. Tamburrano, Overview on recent developments in energy storage: Mechanical, electrochemical and hydrogen technologies, Energy Convers. Manag. 132 (2017) 372–387. doi:10.1016/j.enconman.2016.11.046.

[10] H. Ibrahim, A. Ilinca, J. Perron, Energy storage systems—Characteristics and comparisons, Renew. Sustain. Energy Rev. 12 (2008) 1221–1250. doi:10.1016/J.RSER.2007.01.023.

[11] S. Narayanan, P. Albertus, A robust and inexpensive iron-air rechargeable battery for grid-scale energy storage, (n.d.). https://arpa-e.energy.gov/?q=slick-sheet-project/iron-air-rechargeable-battery (accessed 4 November 2016).

[12] H.A. Catherino, J.F. Burgel, P.L. Shi, A. Rusek, X. Zou, Hybrid power supplies: A capacitor-assisted battery, 2006. doi:10.1016/j.jpowsour.2005.07.012.

[13] L. Jörissen, Bifunctional oxygen/air electrodes, J. Power Sources. 155 (2006) 23–32. doi:10.1016/j.jpowsour.2005.07.038.

[14] S. Liu, S. Liu, J. Luo, Carbon-based cathodes for sodium-air batteries, New Carbon Mater. 31 (2016) 264–270. doi:10.1016/S1872-5805(16)60012-4.

[15] C.-X. Zu, H. Li, Thermodynamic analysis on energy densities of batteries, Energy Environ. Sci. 4 (2011) 2614–2624. doi:10.1039/C0EE00777C.

[16] G. Milazzo, S. Caroli, R.D. Braun, Tables of Standard Electrode Potentials, J. Electrochem. Soc. . 125 (1978) 261C–261C. doi:10.1149/1.2131790.

[17] S.G. Bratsch, Standard Electrode Potentials and Temperature Coefficients in Water at 298.15 K, J. Phys. Chem. Ref. Data. 18 (1989).

[18] J.J. Allen J. Bard, Roger Parsons, Standard Potentials in Aqueous Solution (Monographs in Electroanalytical Chemistry & Electrochemistry), Marcel Dekker, Inc., 1985.

[19] I.B.G. Platzki, Thermochemical Data of Pure Substances, VCH Publishers, New York, 1995.

[20] R. David, CRC Handbook of Chemistry and Physics, 90th ed., CRC Press, Boca Raton Florida, 2009.

[21] D. Linden, Chapter 1. Basic Concepts, in: D. Linden, T.B. Reddy (Eds.), Linden's Handb. Batter., Third, Mcgraw-hill, New York, 2002: pp. 1.3–1.18.

[22] A.J. Bard, L.R. Faulkner, Electrochemical Methods: Fundamentals and Applications, Wiley, 2000. https://books.google.co.uk/books?id=kv56QgAACAAJ.

[23] F.C. Walsh, A First Course in Electrochemical Engineering, Electrochemical Consultancy, 1993. https://books.google.co.uk/books?id=n-9qQgAACAAJ.

[24] D. Pletcher, A First Course in Electrode Processes, The Royal Society of Chemistry, 2009.

[25] T. Reddy, Linden's Handbook of Batteries, McGraw-Hill Professional, 2010.

[26] K. Kinoshita, Electrochemical oxygen technology, John Wiley & Sons, 1992.

[27] M. Egashira, SECONDARY BATTERIES – METAL-AIR SYSTEMS | Iron–Air (Secondary and Primary), in: J.B.T.-E. of E.P.S. Garche (Ed.), Elsevier, Amsterdam, 2009: pp. 372–375. doi:http://dx.doi.org/10.1016/B978-044452745-5.00102-7.

[28] O.C. Wagner, Cadmium-air cell studies, New Jersey, 1971. http://www.dtic.mil/cgi-bin/GetTRDoc?Location=U2&doc=GetTRDoc.pdf&AD=AD0733290.

[29] R.P. Hamlen, T.B. Atwater, Chapter 33. Metal/Air Batteries, in: Linden's Handb. Batter., 4th ed., Mcgraw-hill, 2002.

[30] S.F. Bender, J.W. Cretzmeyer, T.F. Reise, Chapter 13. Zinc / Air Batteries - Button Configuration, in: D. Linden, T. Reddy (Eds.), Linden's Handb. Batter., Third, Mcgraw-hill, New York, 2002: pp. 13.1–13.21.

[31] S.R. Narayanan, G.K.S. Prakash, A. Manohar, B. Yang, S. Malkhandi, A. Kindler, Materials challenges and technical approaches for realizing inexpensive and robust iron–air batteries for large-scale energy storage, Solid State Ionics. 216 (2012) 105–109. doi:10.1016/j.ssi.2011.12.002.

[32] G. Gutmann, Electric Vehicle: Batteries, Encycl. Electrochem. Power Sources. (2009) Vol1, 219–325.

[33] N.P. Yao, U.S.A. EV Battery programme, J. Power Sources. 7 (1982) 317–329. doi:10.1016/0378-7753(82)80025-6.

[34] S.G. Chalk, J.F. Miller, Key challenges and recent progress in batteries, fuel cells, and hydrogen storage for clean energy systems, J. Power Sources. 159 (2006) 73–80. doi:10.1016/j.jpowsour.2006.04.058.

[35] L. Öjefors, L. Carlsson, An iron—air vehicle battery, J. Power Sources. 2 (1978) 287–296. doi:10.1016/0378-7753(78)85019-8.

[36] H. Cnobloch, Energy Storage, Elsevier, 1980. doi:10.1016/B978-0-08-025471-5.50018-X.

[37] W.A. Buzzelli, E.S., Liu, C.T., Bryant, Iron air batteries for electric vehicles, Soc. Automot. Eng. 1 (1978) 745–9.

[38] E.S. Buzzelli, C.T. Liu, W.A. Bryant, Iron-air battery development program, Pittsburgh, Pennsylvania, 1979.

[39] J.O.G. Posada, P.J. Hall, Surface response investigation of parameters in the development of FeS based iron electrodes, Sustain. Energy Technol. Assessments. 11 (2015) 194–197. doi:10.1016/j.seta.2014.10.005.

[40] B. Yang, S. Malkhandi, A.K. Manohar, G.K. Surya Prakash, S.R. Narayanan, Organo-sulfur molecules enable iron-based battery electrodes to meet the challenges of large-scale electrical energy storage, Energy Environ. Sci. 7 (2014) 2753–2763. doi:10.1039/C4EE01454E.

[41] A.K. Manohar, C. Yang, S.R. Narayanan, The role of sulfide additives in achieving long cycle life rechargeable iron electrodes in alkaline batteries, J. Electrochem. Soc. 162 (2015) A1864–A1872. doi:10.1149/2.0741509jes.

[42] J.F. Jackovitz, G.A. Bayles, R.J. Brodd, Chapter 25. Iron electrode batteries, in: D. Linden, T. Reddy (Eds.), Linden's Handb. Batter., Third, McGraw-Hill Education, New York, 2002: pp. 25.1–25.6.

[43] L. Carlsson, Bifunctional Air Electrode for Metal-Air Batteries, J. Electrochem. Soc. 127 (1980) 525. doi:10.1149/1.2129705.

[44] F. Cheng, J. Chen, Metal-air batteries: from oxygen reduction electrochemistry to cathode catalysts, Chem. Soc. Rev. 41 (2012) 2172–2192. doi:10.1039/C1CS15228A.

[45] J.O.G. Posada, P.J. Hall, The effect of electrolyte additives on the performance of iron based anodes for NiFe cells, J. Electrochem. Soc. 162 (2015) A2036–A2043. doi:10.1149/2.0451510jes.

[46] A.K. Manohar, C. Yang, S. Malkhandi, B. Yang, G.K. Surya Prakash, S.R. Narayanan, Understanding the factors affecting the formation of carbonyl iron electrodes in rechargeable alkaline iron batteries, J. Electrochem. Soc. 159 (2012) A2148–A2155. doi:10.1149/2.021301jes.

[47] A.K. Manohar, C. Yang, S. Malkhandi, G.K.S. Prakash, S.R. Narayanan, Enhancing the performance of the rechargeable iron electrode in alkaline batteries with bismuth oxide and iron sulfide additives, J. Electrochem. Soc. 160 (2013) A2078–A2084. doi:10.1149/2.066311jes.

[48] J.O. Gil Posada, P.J. Hall, Post-hoc comparisons among iron electrode formulations based on bismuth, bismuth sulphide, iron sulphide, and potassium sulphide under strong alkaline conditions, J. Power Sources. 268 (2014) 810–815. doi:10.1016/j.jpowsour.2014.06.126.

[49] A.J. Salkind, C.J. Venuto, S.U. Falk, The Reaction at the Iron Alkaline Electrode, J. Electrochem. Soc. 111 (1964) 493–495. doi:10.1149/1.2426166.

[50] L. Öjefors, SEM Studies of Discharge Products from Alkaline Iron Electrodes, J. Electrochem. Soc. . 123 (1976) 1691–1696. doi:10.1149/1.2132669.

[51] B.T. Hang, T. Watanabe, M. Egashira, I. Watanabe, S. Okada, J. Yamaki, The effect of additives on the electrochemical properties of Fe/C composite for Fe/air battery anode, J. Power Sources. 155 (2006) 461–469. doi:10.1016/j.jpowsour.2005.04.010.

[52] Q. Wang, B. Fu, Y. Wang, The Factors Determining Charge Rate of Magnetite Electrode and the Functional Mechanism of Sulfide on the Reaction, Electrochim. Acta. 258 (2017) 143–152. doi:10.1016/J.ELECTACTA.2017.10.090.

[53] Q. Wang, Y. Wang, Overcoming the limiting step of Fe2O3 reduction via in situ sulfide modification, ACS Appl. Mater. Interfaces. 8 (2016) 10334–10342. doi:10.1021/acsami.6b01737.

[54] J.O.G. Posada, P.J. Hall, Towards the development of safe and commercially viable nickel-iron batteries: improvements to Coulombic efficiency at high iron sulphide electrode formulations, J. Appl. Electrochem. 46 (2016) 451–458. doi:10.1007/s10800-015-0911-3.

[55] C. Yang, A.K. Manohar, S.R. Narayanan, A high-performance sintered iron electrode for rechargeable alkaline batteries to enable large-scale energy storage, J. Electrochem. Soc. 164 (2017) A418–A429. doi:10.1149/2.1161702jes.

[56] A.K. Manohar, S. Malkhandi, B. Yang, C. Yang, G.K. Surya Prakash, S.R. Narayanan, A high-performance rechargeable iron electrode for large-scale battery-based energy storage, J. Electrochem. Soc. 159 (2012) A1209–A1214. doi:10.1149/2.034208jes.

[57] R.M. Cornell, U. Schwertmann, Electronic, Electrical and Magnetic Properties and Colour, in: Iron Oxides, Wiley-VCH Verlag GmbH & Co. KGaA, 2004: pp. 111–137. doi:10.1002/3527602097.ch6.

[58] K. Dmitri, SubsTech. Pourbaix diagrams, (2012). http://www.substech.com/dokuwiki/doku.php?id=pourbaix_diagrams (accessed 4 February 2019).

[59] A. Ito, L. Zhao, S. Okada, J. Yamaki, Synthesis of nano-Fe3O4-loaded tubular carbon nanofibers and their application as negative electrodes for Fe/air batteries, J. Power Sources. 196 (2011) 8154–8159. doi:10.1016/j.jpowsour.2011.05.043.

[60] B.T. Hang, D.H. Thang, N.T. Nga, P.T.L. Minh, E. Kobayashi, Nanoparticle Fe2O3-loaded carbon nanofibers as iron-air battery anodes, J. Electrochem. Soc. 160 (2013) A1442–A1445. doi:10.1149/2.066309jes.

[61] B.T. Hang, T. Watanabe, M. Eashira, S. Okada, J. Yamaki, S. Hata, S.-H. Yoon, I. Mochida, The electrochemical properties of Fe2O3-loaded carbon electrodes for iron–air battery anodes, J. Power Sources. 150 (2005) 261–271. doi:10.1016/j.jpowsour.2005.02.028.

[62] H. Kitamura, L. Zhao, B.T. Hang, S. Okada, J. Yamaki, Effect of charge current density on electrochemical performance of Fe/C electrodes in alkaline solutions, J. Electrochem. Soc. 159 (2012) A720–A724. doi:10.1149/2.049206jes.

[63] O. Outiki, E. Lamy-Pitara, J. Barbier, Platinum-palladium catalysts for fuel cell oxygen electrodes, React. Kinet. Catal. Lett. 23 (1983) 213–220. doi:10.1007/BF02065563.

[64] O. Savadogo, K. Lee, K. Oishi, S. Mitsushima, N. Kamiya, K.-I. Ota, New palladium alloys catalyst for the oxygen reduction reaction in an acid medium, Electrochem. Commun. 6 (2004) 105–109. doi:10.1016/j.elecom.2003.10.020.

[65] C. Alegre, A. Stassi, E. Modica, C. Lo Vecchio, A.S. Arico, V. Baglio, Investigation of the activity and stability of Pd-based catalysts towards the oxygen reduction (ORR) and evolution reactions (OER) in iron-air batteries, RSC Adv. 5 (2015) 25424–25427. doi:10.1039/C4RA15578E.

[66] A. Stassi, I. Gatto, V. Baglio, A.S. Aricò, Evaluation of Palladium-based electrocatalyst for oxygen reduction and hydrogen oxidation in intermediate temperature polymer electrolyte fuel cells, Int. J. Hydrogen Energy. 39 (2014) 21581–21587. doi:10.1016/j.ijhydene.2014.05.090.

[67] C. Zhu, A. Nobuta, I. Nakatsugawa, T. Akiyama, Solution combustion synthesis of LaMO3 (M = Fe, Co, Mn) perovskite nanoparticles and the measurement of their electrocatalytic properties for air cathode, Int. J. Hydrogen Energy. 38 (2013) 13238–13248. doi:10.1016/j.ijhydene.2013.07.113.

[68] J.R. Petrie, V.R. Cooper, J.W. Freeland, T.L. Meyer, Z. Zhang, D.A. Lutterman, H.N. Lee, Enhanced Bifunctional Oxygen Catalysis in Strained LaNiO3 Perovskites, J. Am. Chem. Soc. 138 (2016) 2488–2491. doi:10.1021/jacs.5b11713.

[69] G. Karlson, H. Lindström, Catalysis for oxygen evolution in bifunctional air-cathodes, J. Mol. Catal. 38 (1986) 41–48. doi:10.1016/0304-5102(86)87047-x.

[70] A. Damjanovic, M.A. Genshaw, J.O. Bockris, Distinction between Intermediates Produced in Main and Side Electrodic Reactions, J. Chem. Phys. 45 (1966) 4057–4059. doi:10.1063/1.1727457.

[71] I. Morcos, E. Yeager, Kinetic studies of the oxygen—peroxide couple on pyrolytic graphite, Electrochim. Acta. 15 (1970) 953–975. doi:10.1016/0013-4686(70)80037-8.

[72] A.J. Appleby, J. Marie, Kinetics of oxygen reduction on carbon materials in alkaline solution, Electrochim. Acta. 24 (1979) 195–202. doi:10.1016/0013-4686(79)80024-9.

[73] J.O. Bockris, T. Otagawa, The Electrocatalysis of Oxygen Evolution on Perovskites, J. Electrochem. Soc. . 131 (1984) 290–302. doi:10.1149/1.2115565.

[74] M.H. Miles, Y.H. Huang, S. Srinivasan, The Oxygen Electrode Reaction in Alkaline Solutions on Oxide Electrodes Prepared by the Thermal Decomposition Method, J. Electrochem. Soc. . 125 (1978) 1931–1934. doi:10.1149/1.2131330.

[75] H. Ohkuma, I. Uechi, M. Matsui, Y. Takeda, O. Yamamoto, N. Imanishi, Stability of carbon electrodes for aqueous lithium-air secondary batteries, J. Power Sources. 245 (2014) 947–952. doi:10.1016/j.jpowsour.2013.06.146.

[76] M. Yuasa, M. Nishida, T. Kida, N. Yamazoe, K. Shimanoe, Bi-Functional Oxygen Electrodes Using LaMnO3/LaNiO3 for Rechargeable Metal-Air Batteries, J. Electrochem. Soc. . 158 (2011) A605–A610. doi:10.1149/1.3562564.

[77] K.-N. Jung, J.-H. Jung, W. Bin Im, S. Yoon, K.-H. Shin, J.-W. Lee, Doped Lanthanum Nickelates with a Layered Perovskite Structure as Bifunctional Cathode Catalysts for Rechargeable Metal–Air Batteries, ACS Appl. Mater. Interfaces. 5 (2013) 9902–9907. doi:10.1021/am403244k.

[78] W.A. Bryant, The structure and performance of sintered iron electrodes, Electrochim. Acta. 24 (1979) 1057–1060. http://www.scopus.com/inward/record.url?eid=2-s2.0-0018530640&partnerID=40&md5=2e173debfc6cf487d13790680e988b51.

[79] J. Suntivich, H.A. Gasteiger, N. Yabuuchi, H. Nakanishi, J.B. Goodenough, Y. Shao-Horn, Design principles for oxygen-reduction activity on perovskite oxide catalysts for fuel cells and metal-air batteries, Nat. Chem. 3 (2011) 546–550. http://www.scopus.com/inward/record.url?eid=2-s2.0-79959577135&partnerID=40&md5=ee729fd54b6c1b4e9110631b24982e71.

[80] K. Vijayamohanan, T.S. Balasubramanian, A.K. Shukla, Rechargeable alkaline iron electrodes, J. Power Sources. 34 (1991) 269–285. doi:10.1016/0378-7753(91)80093-D.

[81] R. Thacker, On the use of palladium-catalyzed cathodes in a secondary zinc-air cell, Energy Convers. 12 (1972) iii. doi:10.1016/0013-7480(72)90075-7.

[82] C. Tötzke, G. Gaiselmann, M. Osenberg, T. Arlt, H. Markötter, A. Hilger, A. Kupsch, B.R. Müller, V. Schmidt, W. Lehnert, I. Manke, Influence of hydrophobic treatment on the structure of compressed gas diffusion layers, J. Power Sources. 324 (2016) 625–636. doi:10.1016/j.jpowsour.2016.05.118.

[83] T. Danner, S. Eswara, V.P. Schulz, A. Latz, Characterization of gas diffusion electrodes for metal-air batteries, J. Power Sources. 324 (2016) 646–656. doi:10.1016/j.jpowsour.2016.05.108.

[84] R. Adams, R.L. Shriner, Platinum oxide as a catalyst in the reduction of organic compounds. Preparation and properties of the oxide of platinum obtained by the fusion of chloroplatinic acid with sodium nitrate., J. Am. Chem. Soc. 45 (1923) 2171–2179. doi:10.1021/ja01662a022.

[85] S. Siracusano, N. Van Dijk, E. Payne-Johnson, V. Baglio, A.S. Aricò, Nanosized IrOx and IrRuOx electrocatalysts for the O2 evolution reaction in PEM water electrolysers, Appl. Catal. B Environ. 164 (2015) 488–495. doi:10.1016/j.apcatb.2014.09.005.

[86] A. Sundar Rajan, M.K. Ravikumar, K.R. Priolkar, S. Sampath, A.K. Shukla, Carbonyl-iron electrodes for rechargeable-iron batteries, Electrochem. Energy Technol. 1 (2015) 2–9. doi:10.2478/eetech-2014-0002.

[87] A. Ito, L. Zhao, S. Okada, J. Yamaki, Synthesis of nano-Fe3O4-loaded tubular carbon nanofibers and their application as negative electrodes for Fe/air batteries, J. Power Sources. 196 (2011) 8154–8159. doi:10.1016/j.jpowsour.2011.05.043.

[88] D. Pantea, H. Darmstadt, S. Kaliaguine, C. Roy, Electrical conductivity of conductive carbon blacks: influence of surface chemistry and topology, Appl. Surf. Sci. 217 (2003) 181–193. doi:10.1016/S0169-4332(03)00550-6.

[89] J. Sánchez-González, A. Macías-García, M.F. Alexandre-Franco, V. Gómez-Serrano, Electrical conductivity of carbon blacks under compression, Carbon N. Y. 43 (2005) 741–747. doi:10.1016/J.CARBON.2004.10.045.

[90] A.S. Arico, V. Baglio, A. Di Blasi, E. Modica, P.L. Antonucci, V. Antonucci, Analysis of the high-temperature methanol oxidation behaviour at carbon-supported Pt-Ru catalysts, J. Electroanal. Chem. 557 (2003) 167–176. doi:10.1016/S0022-0728(03)00369-3.

[91] a. Stassi, I. Gatto, V. Baglio, A.S. Aricò, Evaluation of Palladium-based electrocatalyst for oxygen reduction and hydrogen oxidation in intermediate temperature polymer electrolyte fuel cells, Int. J. Hydrogen Energy. 9 (2014) 3–9. doi:10.1016/j.ijhydene.2014.05.090.

[92] C. Alegre, E. Modica, M. Rodlert-Bacilieri, F.C. Mornaghini, A.S. Aricò, V. Baglio, Enhanced durability of a cost-effective perovskite-carbon catalyst for the oxygen evolution and reduction reactions in alkaline environment, Int. J. Hydrogen Energy. 42 (2017) 28063–28069. doi:10.1016/J.IJHYDENE.2017.03.216.

[93] M. Chini, R. Antonsen, Ø. Vennesland, J. Håvard Mork, B. Arntsen, Polarization Behavior of Carbon Fiber as an Anodic Material in Cathodic Protection, 2019.

[94] J. Varcoe, P. Atanassov, D. Dekel, A. Herring, M. Hickner, P. Kohl, A. R. Kucernak, W. Mustain, K. Nijmeijer, K. Scott, T. Xu, L. Zhuang, Energy Environ Sci vol7 p3135-3191 (2014), (2014).

[95] C. Ponce De Leon, W. Hussey, F. Frazao, D. Jones, E. Ruggeri, The 3D printing of a polymeric electrochemical cell body and its characterisation, Chem. Eng. Transcations. 41 (2014) 1–6. doi:10.3303/CET1441001.

[96] S. Vinodh, G. Sundararaj, S.R. Devadasan, D. Kuttalingam, D. Rajanayagam, Agility through rapid prototyping technology in a manufacturing environment using a 3D printer, J. Manuf. Technol. Manag. 20 (2009) 1023–1041. doi:10.1108/17410380910984267.

[97] S. V Murphy, A. Atala, 3D printing, Nat. Biotechnol. 32 (2014) 773–785. doi:10.1038/nbt.2958.

[98] F. Allebrod, C. Chatzichristodoulou, P.L. Mollerup, M.B. Mogensen, Electrical conductivity measurements of aqueous and immobilized potassium hydroxide, Int. J. Hydrogen Energy. 37 (2012) 16505–16514. doi:10.1016/j.ijhydene.2012.02.088.